Vibration Analysis of a Shaft-Disc System for On-line Crack Detection

Hamid Khorrami

A Thesis
in
The Department
of
Mechanical and Industrial Engineering

Presented in Partial Fulfillment of the Requirements
for the Degree of Doctor of Philosophy at
Concordia University
Montréal, Québec, Canada

October 2016

CONCORDIA UNIVERSITY
School of Graduate Studies

This is to certify that the thesis proposal prepared

By: **Hamid Khorrami**

Entitled: **Vibration Analysis of a Shaft-Disc System for On-line Crack Detection**

and submitted in partial fulfilment of the requirements for the degree of

Doctor of Philosophy

complies with the regulations of this University and meets the accepted standards with respect to originality and quality.

Signed by the final examining committee:

____________________ Dr. Deborah Dysart-Gale, Chair
____________________ Dr. Dan Zhang, External Examiner
____________________ Dr. Lucia Tirca, External to Program
____________________ Dr. Ion Stiharu, Examiner
____________________ Dr. Rama Bhat, Examiner
____________________ Dr. Subhash Rakheja, Co-supervisor
____________________ Dr. Ramin Sedaghati, Co-supervisor

Approved by ______________________________
Chair of the Department of Mechanical and Industrial Engineering

____
Dean of the Faculty of Engineering and Computer Science

ABSTRACT

Vibration Analysis of a Shaft-Disc System for On-line Crack Detection

Hamid Khorrami,

Concordia University, 2016

This dissertation research concerns detection of cracks in rotating shaft-disc systems using the vibration-based methods. Turbines, pumps and jet engines are some examples of the shaft-disc systems, where crack failures may cause catastrophic effects. Detection of cracks at the early stages of growth is thus vital for prevention of failures, and has been the subject of many studies. Various crack detection methods such as ultrasonic, x-ray and vibration-based methods have been widely developed. Among these, the vibration-based methods are better suited for on-line crack detection. The reliability of such methods, however, relies upon the acquisition of an adequate vibration signature and its correlation with the crack, particularly for small size cracks. The reported studies have employed varying signal processing and crack modeling methods, although the models generally lack of consideration of effects of crack location and other possible faults.

An analytical model of a flexible shaft with two transverse fatigue cracks and two discs mounted on rigid/ resilient supports is formulated, and the corresponding boundary and continuity conditions are developed. A modified harmonic balance method is subsequently proposed for solutions of the governing equations of the analytical model to investigate changes in the selected vibrational properties such as shaft critical speeds, shaft center orbits and super-harmonic components of the steady-state lateral response to an unbalance excitation. The effects of single crack properties such as depth and location on the responses are investigated considering short/long and rigid/flexible bearing supports. The crack is considered as a breathing crack, and is characterized by an exponential function, which facilitated its integration in the modified harmonic balance method. Furthermore, the effects of two cracks' characteristics such as depth, location and relative angular position on selected vibrational properties are studied. Each crack is initially described by a breathing function proposed by Mayes and Davies, which is subsequently modified as a softly-clipped cosine function to accurately describe saturation in breathing phenomenon. The response characteristics of the cracked shaft are also compared with those of the system with an intact shaft in order to identify potential measures for detecting cracks. The validity of the proposed analytical model and the solution strategy is illustrated through comparisons of the model results with those obtained from a finite element model and limited experiments.

The crack-induced changes in transient lateral responses of the shaft-disc system are also considered for transverse crack detection. The shaft-disc system is simply modeled as a Jeffcott rotor to compute its start-up responses in the lateral direction. The breathing behavior of the crack is characterized with respect to stress intensity factor at different points on the crack edge at each shaft angle. A positive stress intensity factor corresponds to the open part of the crack, while the closed part shows a negative stress intensity factor. The breathing crack excites super-harmonic components of the transient as well as the steady-state lateral responses. Time-frequency representation of the transient lateral response obtained from Hilbert-Huang transform based on an improved empirical mode decomposition is used for crack detection. The results show that observed changes in the transient and steady-state lateral vibration responses could lead to effective detection of relatively small size cracks.

ACKNOWLEDGEMENTS

I wish to express my great appreciation and gratitude to my supervisors Dr. Ramin Sedaghati and Dr. Subhash Rakheja for all their support and guidance throughout the course of this research. Financial supports provided by Concordia University are gratefully acknowledged. I would like to extend my appreciation to the Department of Mechanical and Industrial Engineering staff.

Finally, I also would like to express my deepest gratitude to my wife and my parents for their endless love, support and encouragement.

To my beloved wife, Ameneh

TABLE OF CONTENTS

3 Verification of the Modified Harmonic Balance Method and the Alternate Breathing Function 57

List of Figures

List of Tables

Nomenclature

A	shaft cross-sectional area
$\{A\}$	vector of the coefficients of harmonic and super-harmonic components
a	crack depth
a_n,b_n	Fourier series coefficients
a_v	visualized depth of the crack
a_1,a_2	scale and translation parameters in wavelet transform
$\{B\}$	vector of the harmonic external forces acting on the shaft
C	external damping coefficient
	shaft and the rigid disc gyroscopic effect matrices
C_{br}	compliance matrix for a breathing crack in the stationary coordinate
C_{op}	compliance matrix for a fully-open crack in the stationary coordinate
C_r	flexibility matrix in rotating system
$c_{\xi\xi}, c_{\eta\xi}, c_{\xi\eta}, c_{\eta\eta}$	compliance elements of the cracked shaft cross-section in the rotating coordinates
$c_n(t)$	*nth* IMF
D	shaft diameter
E	shaft modulus of elasticity
F	unbalance and gravitational forces imposed on the shaft-disc system
F^d	unbalance and gravitational forces on the rigid disc
F^e	unbalance and gravitational forces at each node
F_u	unbalance force
$f(t)$	crack breathing function
G	shaft shear modulus
G^d	gyroscopic effect for the rigid disc
G^e	gyroscopic effect for each element
G_r	shaft compliance matrix in the rotating system
g	gravitational acceleration,
$H[.]$	Hilbert transform operation
I	shaft area moment of inertia about x-axis
$I_{D,p}$,$I_{P,p}$	disc diametral and polar mass moment of inertias
$IF_n(t)$	instantaneous frequency of the *nth* IMF
$J(\alpha)$	strain energy density function due to the crack
$\mathrm{K_b}$	flexible bearing stiffness
K_C^r	stiffness matrix of the shaft element containing the open crack

K^d	stiffness for the rigid disc
K^e	stiffness for each element
$K^I, K^I_{Q_\xi}, K^I_{Q_\eta}$	stress intensity factors
K_r	stiffness matrix in rotating system
k	shaft shear factor
$k_{\xi\xi}, k_{\eta\xi}, k_{\xi\eta}, k_{\eta\eta}$	stiffness elements of the cracked shaft cross-section in the rotating coordinates
$L(t)$	lower envelope of the original signal
L_0	crack 1 location on the shaft
L_3	crack 2 location on the shaft
L_1	disc 1 location on the shaft
L_2	disc 2 location on the shaft
L_4	shaft length
M	mass matrix integrating the shaft and disc mass matrices
$M_{D,p}$	disc mass without unbalance
M^d_T	translational mass for the rigid disc
M^e_T	translational mass for each element
M^d_R	rotary mass for the rigid disc
M^e_R	rotary mass for each element
M_d	disc mass with unbalance
m	number of harmonics considered in the lateral response
$m(t)$	instantaneous mean of the original signal
m_u	unbalance mass
n	order of the super-harmonics
P_y	static load in y direction
Q_ξ,Q_η	forces acting on the shaft cracked cross-area
R	shaft radius
r_u	unbalance eccentricity
r_0	radius of gyration
$U(t)$	upper envelope of the original signal
U^c	additional strain energy due to the crack
U^e	8×1 element nodal displacement vector
U^d	disc center nodal displacement vector
$u(x,t)$	steady-state lateral response of the shaft

$u(t)$	original signal
$u^t(t)$	represents the transient lateral response of the shaft
u_i	additional deflections due to the crack $(i = \xi, \eta)$
$x_m(t)$	mth residual signal
$[\Delta]$	matrix of coefficients
$\Phi_n(x)$, $G_n(t)$	space- and time-dependent nth super-harmonic components of the lateral response
Φ_r	angle between the crack edge normal line and vertical axis in he stationary coordinate
$\Psi(t)$	mother wavelet
Ω	shaft rotational speed
ω	whirling speed of the shaft
α_n	root of the characteristic equation of the nth super-harmonic component
α_r	shaft acceleration rate
β	unbalance angle
ε_d	unbalance disc eccentricity
$\theta(t)$	shaft rotational angle
ρ	mass density of the shaft
τ	Short-time Fourier transform parameter

Chapter 1

Literature Review and Scope of Dissertation

1.1 Introduction

Transverse crack detection due to cyclic bending loads and other faults in different components of a rotating machine have been widely investigated using different methods over the past many years. Non-vibrational methods have been particularly emphasized for detection of cracks in rotating machines such as ultrasonic, x-ray and infrared radiation methods. Over the past few decades, a number of vibration-based crack detection methods have been explored for on-line detection of cracks. A vibration-based crack detection method involves identification of changes in the vibration properties of a system in relation to selected predefined crack properties. The reliability of such methods, however, strongly relies upon presence of good correlations between a selected vibration measure (crack indicator) and the crack parameters (depth and location).

The crack effect on the system is generally modeled as a local stiffness reduction at the crack location on the shaft. The stiffness reduction due to a crack can be obtained using the fracture mechanics theory or considering the reduction in second moment of area of the cracked shaft cross-section. A crack can be modeled as an open crack or a breathing crack. The crack is considered as an open crack, when the dependence of the stiffness reduction due to the crack on the shaft angle of rotation is considered negligible. In this case, the crack effect is modeled as a rotational spring with a constant stiffness coefficient at the crack location [1]. When the dependence of stiffness reduction due to crack on the shaft angle of rotation is not negligible, the crack is modeled as a breathing crack, where the crack opens and closes during each revolution of the shaft. A range of complex breathing functions have been proposed to accurately describe breathing behavior of a crack [2–4]. The validity and relative merits of the reported breathing functions and their effects on the performance of a crack detection and identification method, however, have not been reported.

The reported studies have proposed diverse vibration-based crack detection and identification methods using widely different signal analysis methods. These, however, exhibit certain limitations, and analyses and implementation challenges. The analyses for detection of a single crack have been mostly considered in a uniform shaft-disc system (a Jeffcott rotor) [e.g., 5–8], while the effects of multiple discs and stepped shafts have not yet been attempted. Moreover, only little efforts have been made to investigate the effects of various confounders involving other form of shaft-disc system faults such as bow shaft and other cracks. Some of the shaft-disc system faults may cause changes in the crack indicator that are similar to those induced by a crack [9]. In such cases, the reliability of the crack indicator and the detection method would be of concern. Furthermore, the reported methods generally do not detect small size cracks and do not provide direct information about the crack location.

In this dissertation research, an analytical model of a shaft-disc system with multiple discs and cracks is formulated to study its responses in the presence of unbalance force. A modified harmonic balance method is proposed to solve the governing equations of lateral motion of the shaft-disc analytical model with one- and two-cracks. Unlike the vast majority of the studies that are limited only to the first harmonic component of the response, the proposed method also yields super-harmonic components of the steady-state lateral response. A methodology to incorporate localized stiffness reductions due to breathing cracks is also presented. The effects of crack parameters such as depth, location and relative angular position are investigated in terms of critical speeds, shaft center orbits close to sub-critical speeds and amplitudes of harmonic and super-harmonic components of the steady-state lateral response. These response characteristics are discussed in view of their potential for detecting the presence of one and two cracks in the rotating shaft. The critical speeds are also compared with those obtained from the developed Finite Element (FE) model of the shaft-disc system and from laboratory experiments to examine the validity of the model. An alternate breathing function is subsequently proposed to more accurately model the breathing behavior of the fully-open and closed crack. It is shown that the proposed breathing function significantly improves efficiency of the applied method for detection of two cracks in a rotating shaft. Furthermore, the time-frequency representation of the transient lateral response of the shaft-disc system is considered for crack detection. The Hilbert-Huang transform based on an improved empirical mode decomposition is used to obtain relatively higher resolutions of the crack indicator to improve its effectiveness for detecting small size cracks.

1.2 Literature review

Studies reporting different methodologies for detecting crack defects in shaft-disc systems on the basis of vibration analyses and measurement are critically reviewed to formulate the scope of the present dissertation research. The reported studies, grouped under relevant topics, are discussed in the following sections.

1.2.1 Non-vibrational methods

Non-vibrational methods such as x-ray, infrared radiation and ultrasonic methods are widely used for detecting faults in machine components. Among these, the ultrasonic methods are more commonly used. The ultrasonic methods involve propagation of high frequency sound energy, generated using high voltage electrical pulses, through the test components, and measurements of sound reflections. A defect tends to alter the properties of the reflected sound waves [10, 11]. The x-ray and infrared radiation methods involve specific imaging of the test component, where a crack emerges in a distinct color [12, 13]. A number of limitations of these methods have been documented in the literature such as greater sensitivity to high levels of noise

[14], requirement of scanning of the entire components that may not be directly accessible [15, 16], poor performance in detecting crack defects in earlier stages [17] and relatively high costs [17]. Moreover, such methods are not suited for on-line detection of cracks during machines operations. Alternatively, the vibration-based damage detection techniques have shown superior potential to overcome the limitations associated with conventional non-vibrational detection techniques.

1.2.2 Vibration-based methods

Signal- and model-based methods

A variety of vibration-based crack detection methods have been proposed during the past few decades. Vibration-based crack detection and identification methods can be classified into two categories, namely, the signal-based and the model-based methods[18]. In the first category, only the changes in the selected vibrational properties of a system are considered to build a qualitative fault-symptom correlation [e.g., 19–21]. Probabilistic classifications such as the fuzzy logic or the artificial neural networks can be applied to define the fault-symptom correlation [22]. The signal-based methods do not depend on the properties of the system under consideration and can be used for crack detection in widely different types of systems [23]. Signal-based methods do not require a mathematical model of the system, while these can provide vital information related to dynamic behaviors of the intact and the cracked systems.

In the second category, a mathematical model of the system is necessary to define a quantitative fault-symptom relation. These generally involve: (i) modeling the shaft-disc system; (ii) modeling the crack effect on the system; (iii) defining a crack indicator; and (iv) identifying a correlation between the crack parameters and changes in the values of selected crack indicators. The flow graphs in Figure 1.1 illustrate signal- as well as model-based methods. In majority of these studies, the

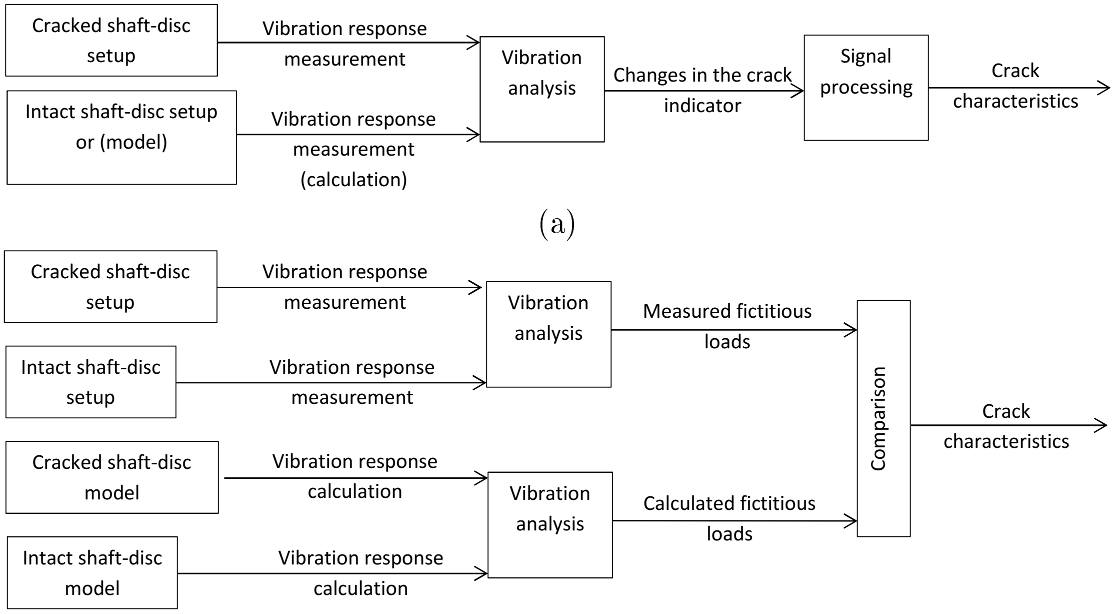

(a)

(b)

Figure 1.1: (a) Signal- and (b) model-based crack detection methods

identification of a crack and its depth primarily relies on the analysis of crack-induced changes in selected vibrational properties of the shaft-disc system with respect to the reference values obtained for the intact (uncracked) system.

In model-based crack identification methods [e.g., 24–26], the internal loads due to the crack are mostly replaced by equivalent external fictitious loads applied to the intact system model. The crack parameters could be determined through comparing the fictitious loads obtained from the constructed system model and those estimated from vibrational measurements [27]. Although the model-based methods rely on static and dynamic characteristics of the system, these are considered to be more reliable and more adaptable than the signal-based methods for detection of other machine faults[28]. A few studies have proposed methods integrating both the signal- and model-based approaches for more effective detections [29, 30].

Off- and on-line methods

The reported crack detection methods may be further classified in on- and off-line methods. The crack detection methods attempting to detect a crack in a rotating shaft are referred to on-line methods, while those focusing on crack identification in a non-rotating shaft are called off-line methods. An on-line method can be applied during steady-state rotational speeds and shutdown or startup stages, whilst the off-line method is specifically limited to the non-rotating shafts. Contrary to non-rotating structures, the equations of motion of rotating structures are non-self-adjoint (NSA), containing non-symmetric system matrices which can lead to non-symmetric frequency response function (FRF) matrix [31]. The NSA equations refer to equations of motion of a system which are physically symmetric but mathematically asymmetric. Structures with NSA equations need two sets of eigenvectors and a set of eigenvalues to be completely defined. The necessity of using two eigenvectors (left- and right-eigenvectors) arises from the fact that both sensor and excitation devices should change their position on different points of the structure to fully define the system [31]. Some simplifications can result in special relation between left and right eigenvectors, such as an undamped gyroscopic system [31]. The on-line methods are far more advantageous than the off-line methods in detecting small size cracks [32]. Moreover, the on-line methods do not require stoppage of the machine.

The on-line crack detection methods, however, known to be most sensitive to unknown external forces, geometric variations and sensor noise. The off-line methods are thus recommended to verify the correctness of an on-line crack detection method [33]. Moreover, natural frequencies and FRFs are a function of rotational speed in rotating structures [31], which tend to induce errors in on-line methods. For instance, Dong et al. [34] attempted to detect the crack parameters of a non-rotating shaft, while many other studies have focused on developing the on-line crack detection strategies [17, 25, 35–37].

1.2.3 Shaft-disc system modeling

The governing equations of lateral motion of shaft-disc systems have been reported in many analytical [e.g., 4–6, 38–40] and numerical [e.g., 1, 15, 41–46] models. These models have been mostly derived using the Euler-Bernoulli [e.g., 38, 47] and Timoshenko beam theories [e.g., 4, 44, 48]. The Jeffcott rotor model, as a simplified lumped analytical model, has been widely used in obtaining the steady-state [e.g., 5, 6, 49] as well as transient [e.g., 7, 8, 50] lateral responses of the shaft-disc systems. This model considers a single rigid disc on the mid-span of a massless flexible shaft to obtain vibrational properties in the vertical and horizontal directions. The vibrational properties of a rotating shaft-disc system, however, are strongly affected by the crack location and the gyroscopic effects, especially at higher spin speeds of the shaft, which are not considered in the simplified Jeffcott rotor model.

Eshleman and Eubanks [38] developed an analytical model of an intact continuous shaft-disc system using Euler-Bernoulli theory to obtain critical speeds of the system considering the effect of coupling in lateral motion as well the gyroscopic effects of the shaft and the disc. The analytical results showed good agreements with those obtained from the experiment. The governing equations of lateral motion of a continuous shaft have also been derived using the Timoshenko beam theory [39, 40]. Such analytical models permit analysis of effects of crack location on the shaft vibrational properties. Chasalevris and Papadopoulos [4] developed a cracked continuous shaft-disc model to study the effects of crack depth on higher critical speeds of the rotating system. The study reported that the higher critical speeds are more sensitive to crack propagation and can be effectively used to detect small size cracks.

A number of numerical models of the rotating cracked shaft-disc systems have also been reported, which are based on FE methods using Euler-Bernoulli and Timoshenko beam theories [e.g., 15, 41–45]. Such models have been employed for the crack location sensitivity analysis considering the gyroscopic effects of the shaft and the disc. The study of crack effect in FE models generally requires relatively more computational efforts compared with the analytical models [1, 46]. Furthermore, the FE model of the cracked system should be adjusted for each crack location on the shaft. Lees and Friswell [46] reported that the effects of crack depth on the rotating system responses strongly depend on the length of the shaft element containing the crack, and suggested that this parameter should be chosen within a reasonable range.

The studies have also employed different solution strategies, which satisfy the continuity and boundary conditions to obtain steady-state and transient responses, and changes in the selected vibrational properties. Some studies have employed a solution function in the exponential form, which is only limited to the first harmonic component [e.g., 4, 39, 40, 51], while others have used numerical integration techniques to obtain super-harmonic components of the steady-state responses [e.g., 3, 6, 52] and the transient responses [e.g., 50, 53, 54] of the analytical models. The steady-state responses of FE models have also been obtained using different methods such as generalized harmonic balance and alternate frequency/time domain methods [e.g., 44, 55].

1.2.4 Crack modeling

The reported studies have invariably shown that a crack induces changes in the local stiffness of the shaft and consequently the dynamic behavior of the shaft-disc system [e.g. 2, 18, 44]. Furthermore, the crack geometry tends to vary during a rotation cycle. The crack modeling thus involves two distinct challenges: (i) obtaining the stiffness changes due to the crack, and (ii) defining a function to describe a relation between crack-induced changes and angle of rotation of the shaft during each revolution. The stiffness reduction due to the crack may be accurately estimated using the fracture mechanics concepts [2, 18] or considering the changes in the area moment of inertia about the transverse coordinates of the cracked shaft cross-section [37, 44].

A crack may undergo either tension or compression during each rotation cycle, which yields considerable variation in the shaft stiffness with the angle of rotation. A tensile stress imposes the crack to remain open, while it is closed under compression. In asynchronous whirling, the rotational speed of the shaft Ω differs from the whirling speed ω, which causes the stress zones on the shaft cross-section to vary leading to sequential crack opening and closing (breathing) during each revolution of the shaft. Furthermore, in synchronous whirling, the stress zones on the shaft cross-section also change when the shaft lateral vibration magnitude due to an external excitation is negligible compared to static deflection of the shaft. Otherwise, the crack remains open or closed as the shaft rotates, as shown in Figure 1.2.

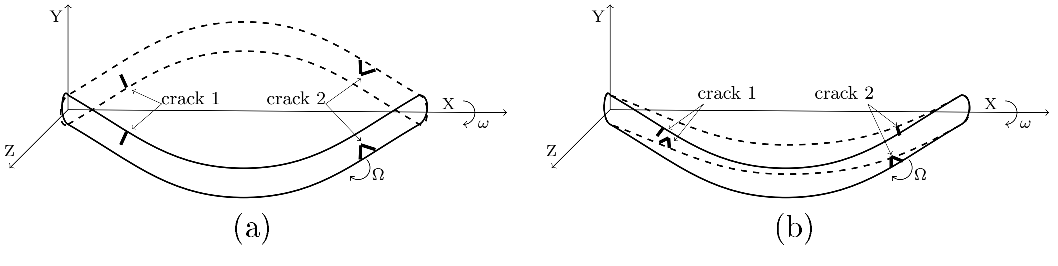

Figure 1.2: The synchronous whirling of a cracked shaft: (a) the static deflection of the shaft is negligible, the crack 1 remains closed while the crack 2 remains open; and (b) the static deflection of the shaft is not negligible, the crack 1 and crack 2 breath during each revolution of the shaft

A crack may be simply considered as an open crack when the variation in the stiffness due to the shaft angle of rotation are considered negligible [6, 56]. Alternatively, a number of studies consider the crack as a breathing crack to accurately describe its behavior as a function of the shaft rotation [57–59]. These have described crack breathing via step and periodic functions to accurately describe the changes in crack geometry and thus the stiffness effect as a function of shaft angle of rotation [1, 3, 55, 60]. The step function assumes that the crack opens and closes abruptly during a revolution of the shaft, while the function proposed by Mayes and Davies [60] consider periodic opening or closing of the crack with the shaft angle of rotation. Figure 1.3 compares step and Mayes and Davies breathing functions in a shaft fixed reference system.

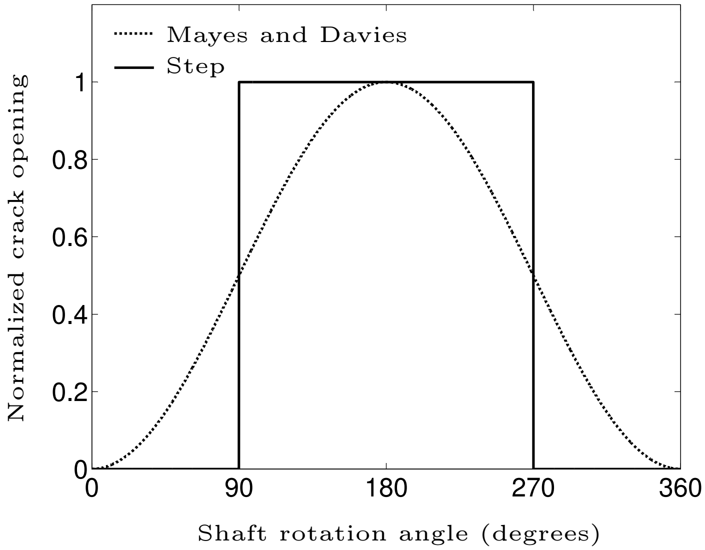

Figure 1.3: Step and Mayes and Davies breathing functions in a rotating coordinate system

A few studies have employed linear fracture mechanics to evaluate local stiffness of the shaft cross-section near the crack location corresponding to different shaft angles of rotation and proposed breathing crack models considering the effects of crack depth and location [2–4]. These breathing functions are considered to be effective in more accurate modeling of the crack behavior for a wide range of crack depths. Jun et al. [3] used the sign of the total stress intensity factor (SIF) at each point on the crack edge to determine whether the crack is open or closed. In compressive stress state, the sign of total SIF is negative and the crack is assumed to be closed, while in tensile stress state the sign of total SIF is positive and consequently the crack is considered to be open. Darpe et al. [2] introduced the concept of crack closure line (CCL), an imaginary line perpendicular to the crack edge separating the open and closed parts of the crack, to study breathing behavior of the crack. The CCL position was obtained considering the sign of the total SIF at each point on the crack edge, as proposed by Jun et al. [3].

Owing to complexities associated with evaluations of the stress intensity factor for shaft angles corresponding to stress state transition between the vertical and horizontal moments, Chasalevris and Papadopoulos [4] employed B-spline curves to interpolate between the transient points. Al-Shudeifat and Butcher [43] used changes in area moment of inertia about the transverse coordinates of the cracked shaft cross-section area to obtain a breathing function which more accurately describes the real breathing behavior of the crack. The method considered exact locations of centroid and neutral axis of the cracked shaft cross-section at each shaft angle to estimate corresponding area moments of inertia and the local stiffness.

1.2.5 Crack indicator

The changes in different vibrational properties due to a crack have been utilized for detection of cracks in rotating shaft-disc systems. Reduction in critical speeds of a rotating shaft-disc system has been widely used as a simple crack indicator in many studies [e.g. 1, 43, 56]. The critical speed is the spin speed of the shaft, in which the natural frequency of the shaft-disc system is excited and amplitudes of the lateral response in vertical and horizontal directions are maximized. The changes in the critical speed, however, may be caused by many other faults in the shaft-disc system such as bent shaft, coupling misalignments and polar stiffness asymmetries

[9, 25], which may affect the reliability of such a crack detection method.

In the presence of a breathing crack, the super-harmonic components in lateral response of an unbalanced rotating shaft-disc system are excited. Relatively low magnitude resonant peaks emerge at rational fractions of the critical speeds. Such sub-critical resonant peaks, however, may also arise due to some other faults in the shaft-disc system such as polar stiffness asymmetries, surface geometry errors and non-linear effects in oil film bearings [25]. In some studies, the emergence of these resonant peaks near sub-critical speeds has been considered to indicate the existence of a crack [e.g., 3, 37, 55, 61, 62]. Furthermore, it has been reported that crack detection methods based on the emergence of sub-critical resonant peaks are more reliable than those based on shift in the critical speed [37].

Sinou and Lee [55] compared the steady-state lateral responses of a shaft-disc system with and without a transverse breathing crack, which are presented in Figure 1.4. The results show presence of sub-critical resonant peaks of relatively low magnitudes in the steady-state vertical (points 1,2 and 4) and horizontal (point 6) displacement responses of the cracked shaft, which are not evident in the responses of the intact shaft. Furthermore, the results show slight reduction in first and second critical speeds (points 3 and 5) due to the crack, as seen in the vertical displacement response. However, changes in critical speeds of the system are not clearly observable in the horizontal direction (points 7 and 8).

Alternate vibration-based crack indicators such as changes in transient response, shaft center orbit evolution at sub-critical speeds, torsional-lateral vibration coupling and equivalent fictitious loads, have also been proposed for detection of a crack in shaft-disc systems [e.g., 25, 29, 56]. As a shaft-disc system with a breathing crack passes through rational fractions of its critical speeds, inner loops of the shaft center orbit form due to excitations of the super-harmonic components of lateral response. Gasch [62] has illustrated the evolution of shaft center orbits of a cracked

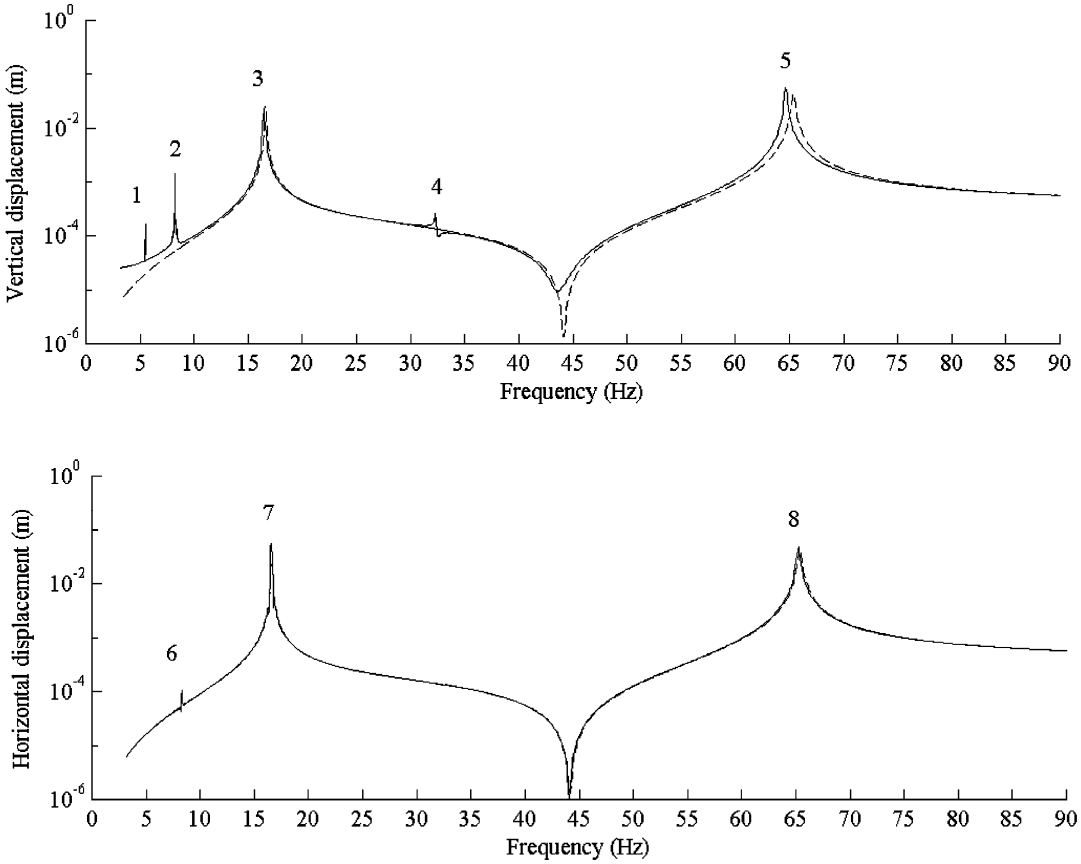

Figure 1.4: Emergence of sub-critical resonant peaks in steady-state lateral displacement of a shaft-disc system; dashed line and solid line represent the intact and cracked systems, respectively [55]

rotating shaft passing through $\frac{1}{3}$ and $\frac{1}{2}$ of its first critical speed, as shown in Figure 1.5. The results show that the shaft center orbit is comprised of 2 and 3 inner loops at $\frac{1}{3}$ and $\frac{1}{2}$ of the critical speed, respectively.

In model-based crack detection methods, the basic idea is that the crack effect on the dynamic behavior of the shaft-disc system can be characterized by fictitious forces and moments exerted on the intact system. The amplitudes and positions of these fictitious loads on the shaft depend on the crack depth and location, respectively. Sekhar [27] employed the fictitious loads as reliable crack indicators using a FE shaft-disc model, shown in Figure 1.6 (a). In the model, a breathing crack is positioned in the 7th element, and the fictitious loads are located on the end nodes

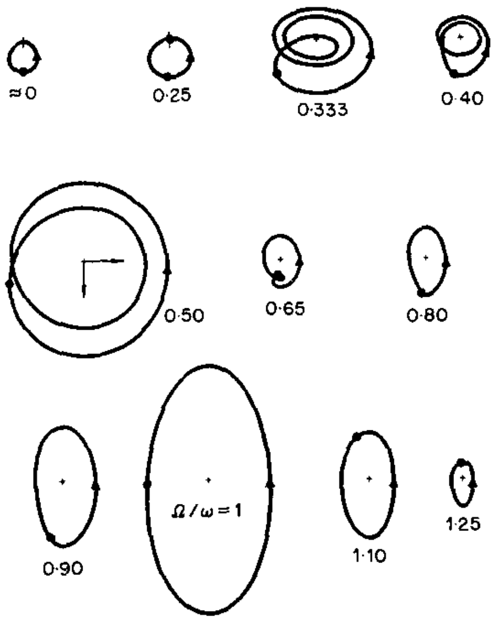

Figure 1.5: Shaft center orbits evolution passing through rational fractions of the critical speed; Ω and ω represent the shaft spin speed and whirling speed, respectively [62]

of the corresponding cracked element. Moreover, as the crack depth increases the severity of the fictitious loads increases, as seen in Figures 1.6 (b) and 1.6 (c).

Darpe [63] reported that the presence of a transverse crack on a rotating shaft leads to coupling between lateral and torsional vibrations, which may serve as a measure of crack detection. The study showed the emergence of low amplitude oscillations in the horizontal and vertical vibration responses to transient torsional excitations, as shown in Figure 1.7. Such small variations in lateral response, however, could not be clearly detected in the time response and frequency spectrum particularly in the presence of small crack depths. Darpe [63] employed wavelet transform to detect these changes. He also reported that the torsional-lateral vibration coupling and equivalent fictitious loads are generally affected only by crack defects and have shown relatively lower sensitivity to other faults in the shaft-disc system. The implementation of such crack indicators, however, would require an external torsional excitation, and vibration measurements of the intact as well as

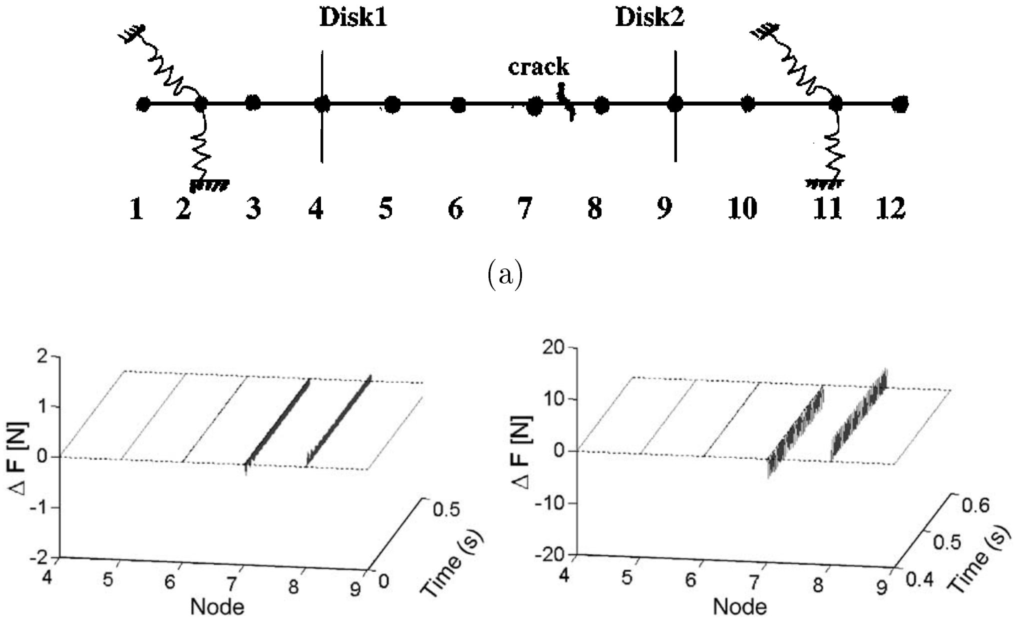

(a)

(b)

(c)

Figure 1.6: (a) FE shaft-disc model with a crack located on the 7th element; and computed fictitious loads ΔF, corresponding to the breathing crack with (b) 1.4 mm; and (c) 4mm depth (shaft diameter = 20 mm) [27]

the cracked shaft-disc system.

The changes in transient lateral responses of the shaft-disc system have also been investigated in many studies for crack detection. Plaut et al. [47] considered the effects of crack parameters, namely, depth and location, and shaft acceleration and deceleration rate on the maximum transient response passing through the first critical speed of the system, considered as a reliable crack indicator. Sawicki et al. [64] suggested that the "saw-cut" pattern in the vibration phase response as the rotor accelerates can be considered as a crack indicator. Darpe et al. [50] considered shaft center orbit evolution and relatively stronger super-harmonic components in the horizontal direction than in the vertical direction passing through sub-critical resonances as reliable crack indicators. The study applied Fourier transform for determining amplitudes of sub-critical resonant peaks in the transient response of the shaft-disc-system.

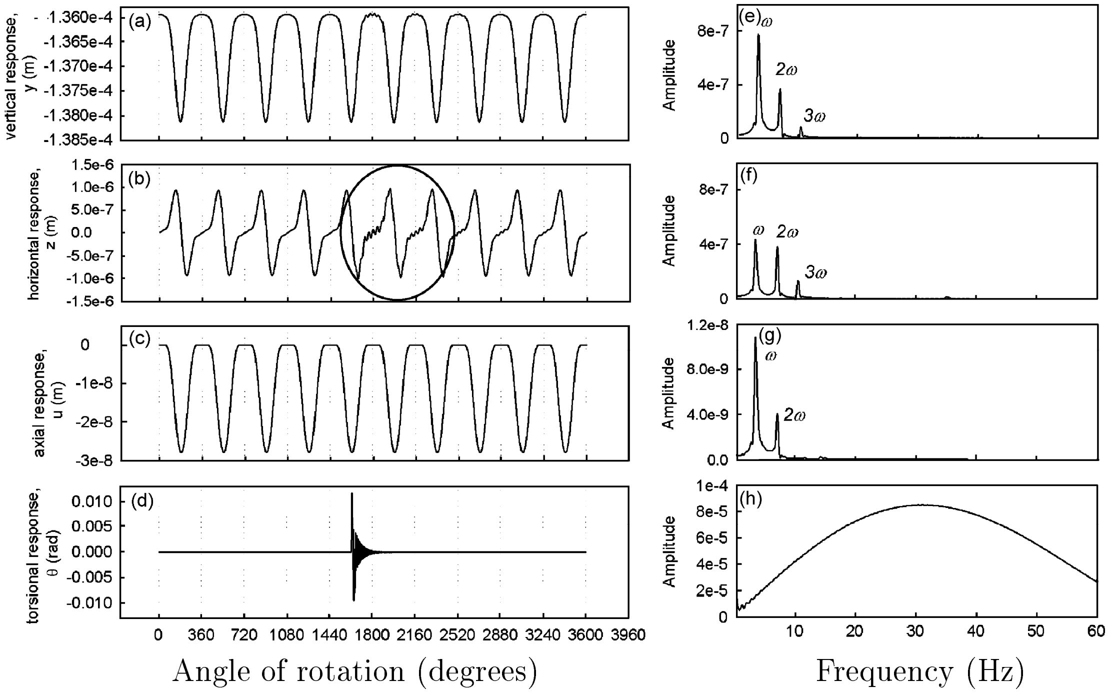

Figure 1.7: Lateral and axial steady-state responses of a cracked shaft-disc system with transient torsional excitation [63]

The emergence of low amplitude sub-critical resonant peaks in rotor transient response has been considered as a reliable crack indicator. The sub-critical resonant peaks, however, are affected by several parameters such as start-up/ run-down rotational acceleration/ deceleration rates and unbalance phase [50, 53]. Thus, the sub-critical resonant peaks are usually hard to detect in time response especially in the presence of small cracks. Alternate signal processing techniques are thus required to analyze transient responses so as to obtain essential information related to sub-critical resonant peaks. Table 1.1 summarizes different crack indicators proposed in the literature.

Crack indicators using signal processing transforms

Fourier transform is a suitable signal processing method for analyzing signals, where the frequency contents do not change in time (stationary signals). The response amplitudes corresponding to different frequencies are obtained from [65]:

Table 1.1: Comparison among different crack indicators proposed in the literature

Crack indicator	Provide direct information about the crack	
	depth	location
Changes in critical speeds	yes	no
Evolution of the shaft center orbit	yes	no
Emergence of sub-critical resonant peaks	yes	no
Changes in transient lateral responses	yes	no
Coupling between lateral and torsional vibrations	yes	no
Changes in mode shapes	yes	yes
Fictitious loads	yes	yes

$$\hat{U}(\omega) = a(\omega) = \int_{-\infty}^{+\infty} u(t) e^{-in\omega t} dt \tag{1.1}$$

where $u(t)$ is the time signal, often expressed by the Fourier series, as:

$$u(t) = \sum_{n=-\infty}^{\infty} c_n e^{in\omega t} \tag{1.2}$$

Short-Time Fourier Transform (STFT) methods have also been applied for analyzing non-stationary signals. The STFT is expressed as [66]:

$$STFT(\omega, t) = \frac{1}{2\pi} \int_{-\infty}^{+\infty} u(t) h(t-\tau) e^{-i\omega\tau} d\tau \tag{1.3}$$

where the window function $h(t-\tau)$ slides along the signal $u(t)$ with steps equal to the variable τ. The STFT divides a non-stationary signal into approximately stationary segments using the window function. The Fourier transform thus yields frequency contents of each segment. The size of the window function can effectively change the time and frequency resolutions in the STFT time-frequency representation of the signal. For instance, a short window provides higher time resolution with lower frequency resolution, while a wide window gives lower time resolution with higher frequency resolution. It should be noted that the size of the window function is fixed once it has been selected, the STFT time-frequency representation may thus yield either good frequency or good time resolution [66].

However, in transient responses the frequency contents change in time (non-stationary signals). The frequency contents are thus be extracted using alternate advanced signal processing techniques such as Wigner–Ville distribution, wavelet transform (WT) and Empirical Mode Decomposition (EMD) [67–69]. The time and frequency resolution problem of STFT has also been resolved using the Wigner–Ville distribution, proposed by Eugene Wigner [67], defined as:

$$WV(\omega, t) = \frac{1}{2\pi} \int_{-\infty}^{+\infty} u(t + \frac{\tau}{2}) conj(u(t - \frac{\tau}{2})) e^{-i\omega\tau} d\tau \tag{1.4}$$

The Wigner–Ville distribution does not use a window function as in the case of STFT and provides relatively higher time and frequency resolutions correlating the signal with its translated version in time and frequency [67]. However, this distribution may produce cross-term interferences in analysis of multicomponent signals, which may pose difficulties in the interpretations of the time-frequency representations [70].

Wavelet transform considers flexible window functions namely, wavelet to provide multi-resolution time-frequency representation of a non-stationary signal. The wavelet transform (WT) of the signal $u(t)$ can be expressed as [68]:

$$\begin{aligned} WT(a_1, a_2) &= \int_{-\infty}^{+\infty} u(t) \Psi_{a_1,a_2}(t) dt \\ \Psi_{a_1,a_2}(t) &= \frac{1}{\sqrt{a_1}} \Psi(\frac{t - a_2}{a_1}) \end{aligned} \tag{1.5}$$

where $\Psi(t)$ is the mother wavelet, and a_1 and a_2 are scaling and translation parameters, respectively, which determine the shape of wavelets $\Psi_{a_1,a_2}(t)$. A wavelet of large scales (window with narrow frequency and wide time) extracts lower frequency components with higher frequency resolution, while that with smaller scales (window with narrow time and wide frequency) yields higher frequency components with higher time resolution.

Figure 1.8 compares the window functions used in STFT and WT as functions of time and frequency. It is observed that the selected window function (e.g.,

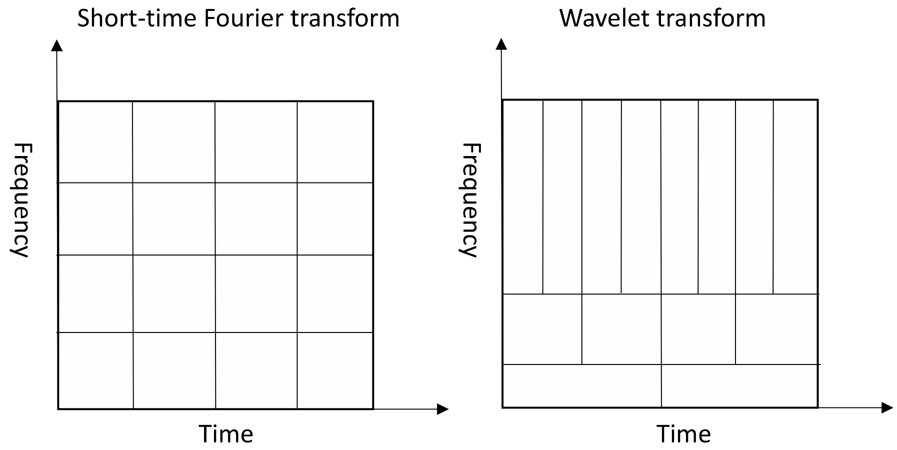

Figure 1.8: Difference between Short-time Fourier transform and wavelet transform window functions

Hamming or Gaussian) in STFT assumes a fixed shape, while the window function (mother wavelet, e.g., Morlet, Haar and Symmlet) chosen in WT possesses variable shapes. The wavelet transform is considered as an adaptive transform due to the variable shape of the mother wavelet. The wavelet transform thus yield high time and frequency resolutions, while the chosen mother wavelet can effectively alter the time-frequency representation results, if it is not properly correlated with the signal [71].

The performance of the Wigner–Ville distribution in crack identification using the transient response has been evaluated by Zou et al. [7]. The study concluded that the Wigner–Ville distribution is highly sensitive to small shaft stiffness changes due to small cracks. Figure 1.9 compares the time-frequency representations of intact and cracked rotor's transient responses obtained from the Wigner–Ville distribution. The comparisons show that a crack introduces small oscillations to the regular ellipses of the intact rotor's time-frequency representation [7].

The wavelet transform provides time-frequency representation of a signal using a scaled shifted mother wavelet. Different types of wavelet transform have been used to detect the sub-critical resonant peaks [72–75]. Sekhar [72] suggested that

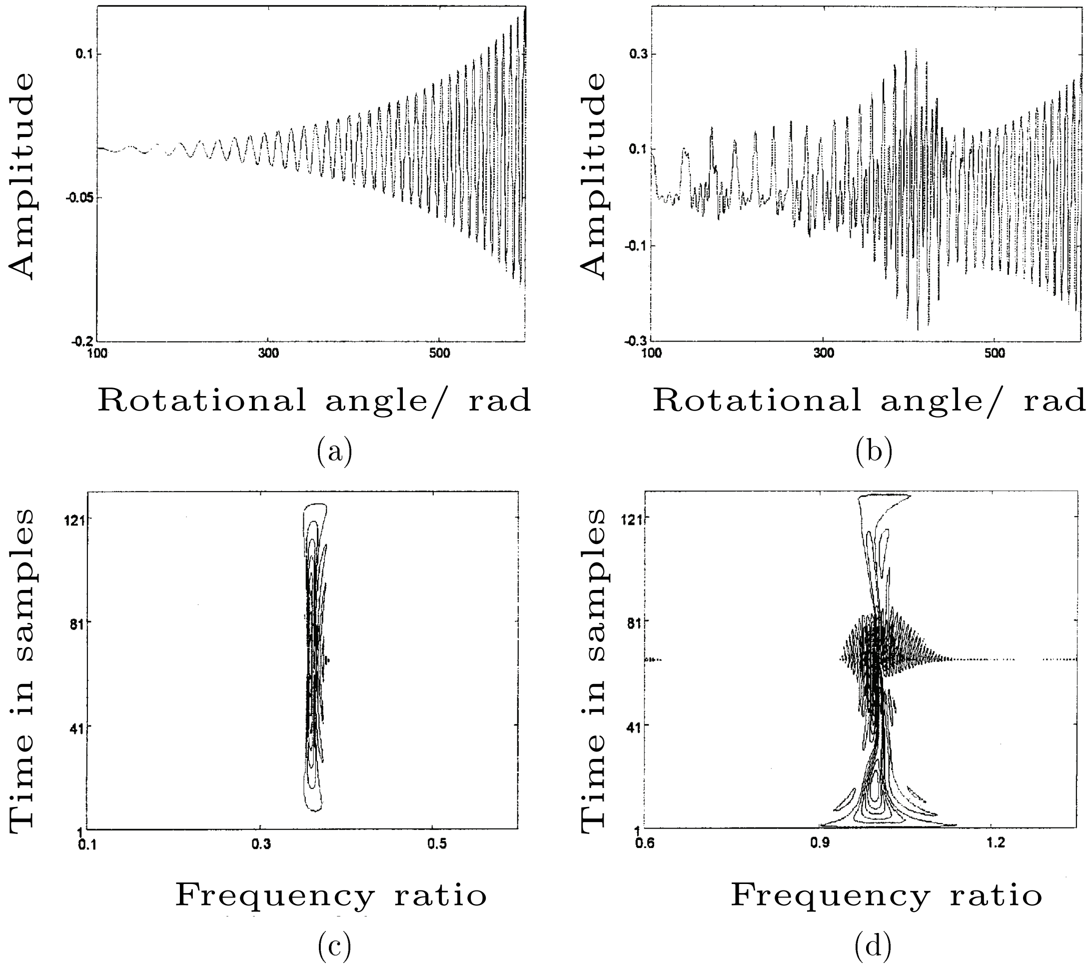

Figure 1.9: Transient lateral response of a rotor (a) intact and (b) cracked; and their corresponding Wigner–Ville time-frequency representations (c) intact and (d) cracked [7]

the continuous wavelet transform (CWT) could serve as a powerful tool for crack detection in a Jeffcott rotor coasting down through its critical speed. The coefficients of the CWT have been shown to be sensitive to the crack depth and can thus be applied as efficient crack indicators. The transient responses of intact and cracked rotors and their corresponding CWT coefficients are illustrated in Figure 1.10 [72]. The results show that the crack-induced changes in CWT coefficients are clearly detectable compared with those in the time responses. Sekhar [73] further established that the CWT is a powerful tool in crack detection particularly in high start-up acceleration rates.

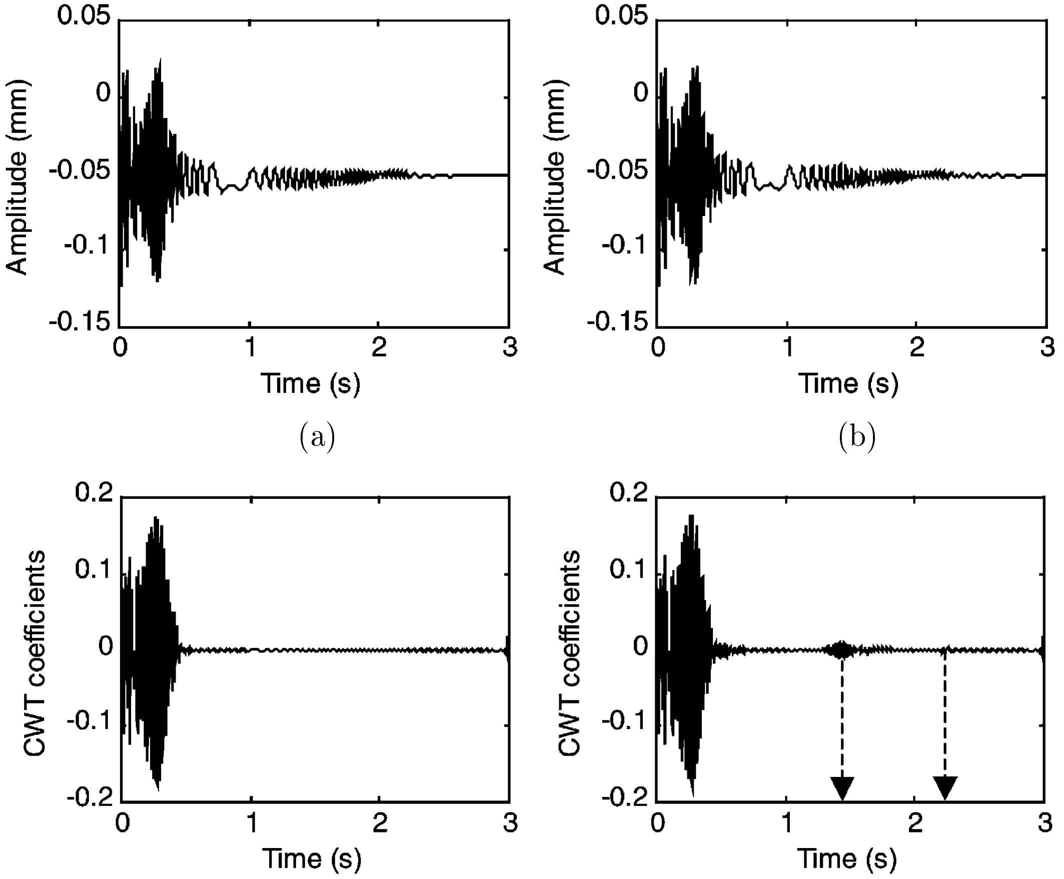

(a) (b)

(c) (d)

Figure 1.10: Coasting down lateral response of a rotor (a) intact and (b) cracked; and their corresponding CWT coefficients (c) intact and (d) cracked [72]

The wavelet transform yields high resolution frequency analysis for the entire time signal, although the time and frequency resolutions are highly affected by the chosen mother wavelet [76]. Alternate methods such as empirical mode decomposition (EMD) have been applied to obtain high frequency resolution analysis without using preselected kernels. The EMD decomposes signal into a set of orthogonal components representing local characteristics of the time signal, which consequently yields local high resolution frequency analysis. The Hilbert–Huang transform is a EMD-based transformation for finding the instantaneous frequency components of signals [69]. Guo and Peng [77], and Ramesh et al. [48] have effectively applied the Hilbert–Huang transform for crack detection using transient response. Guo and Peng [77] established the effectiveness of Hilbert–Huang transform for detecting propagating transverse cracks, while Ramesh et al. [48] showed that Hilbert–Huang transform outperforms the CWT. Chandra and Sekhar [78] employed the EMD for detections of shaft misalignment, and crack and rotor stator rubbing faults in rotor bearing systems. From comparisons of the results of the time-frequency representation obtained from EMD with those obtained from CWT, the study concluded that the EMD method can lead to detection of relatively smaller cracks with lesser computation time.

While time-frequency representations of the signals obtained from EMD methods exhibits relatively higher local resolution frequency analysis, a few studies have established their limitations [79, 80]. A number of alternate approaches have been proposed to address these limitations of EMD, which include end effects [e.g., 81–83], extremum interpolation [e.g., 84, 85] and mode mixing [86]. These studies have proposed extension methods, alternate interpolation approaches and noise-assisted data analysis methods. A comprehensive review of improved EMD algorithms and their applications in rotary machine fault diagnosis is presented in [76].

1.2.6 Shaft-disc system with two or more cracks

The effects of a single crack on vibrational properties of different structural systems have been widely reported, while the effects of two or more cracks have been addressed in a relatively fewer studies. This is likely due to complexities associated with identifications of crack properties in the presence of additional cracks. For instance, it has been shown that different combinations of properties of single or multiple cracks such as depth and relative locations may yield similar effects on vibrational properties of the system. Sekhar [15] conducted a review of methods for identifying two or more cracks in components such as beams, rotors and pipes, and concluded that efficiency of identification methods for single or multiple cracks mostly depends on the applied signal processing techniques. Owing to variations in vibration responses with varying speeds, the time-variable frequency contents of responses of cracked mechanical systems and their features are extracted using advanced signal processing techniques such as wavelet transform and Hilbert-Huang transform [e.g., 48, 73, 74, 77].

Some studies have presented changes in preselected vibrational properties due to known multiple crack parameters [e.g., 6, 56], while others have presented inverse problem of determining multiple cracks parameters from known changes in vibrational properties [e.g., 87, 88]. Sekhar [56] investigated effects of two open cracks on the eigenfrequencies, mode-shapes and threshold speed of a rotor system using FE method. Darpe et al. [6] studied the effect of two breathing cracks on unbalance response of a simple Jeffcott rotor. Both studies suggested that relative angular position of the two cracks may exhibit significant changes in the shaft center orbit. Saridakis et al. [87] formulated an inverse problem for identifying cracks properties (depth, location and relative angular position) from known changes in vibrational properties of a flexible cantilever shaft with two breathing cracks. The inverse problem was solved using artificial neural networks, genetic algorithm and fuzzy logic methods. The study suggested that the method could provide real-time identification of crack parameters.

Ramesh and Sekhar [88] proposed an alternate crack indicator, referred to as ‘amplitude deviation curve (ADC)’ or ‘slope deviation curve (SDC)’, based on the concept of operational deflection shape (ODS) and concluded that the method outperforms that based on the continuous wavelet transform reported in [20] for detecting two breathing cracks. The ODS operator considers the entire shaft deflection at a specific shaft speed, which may change under different external loads acting on the shaft. Ramesh and Sekhar [88] observed small sudden changes in ODS at the location of cracks on the shaft, and suggested that these changes may be

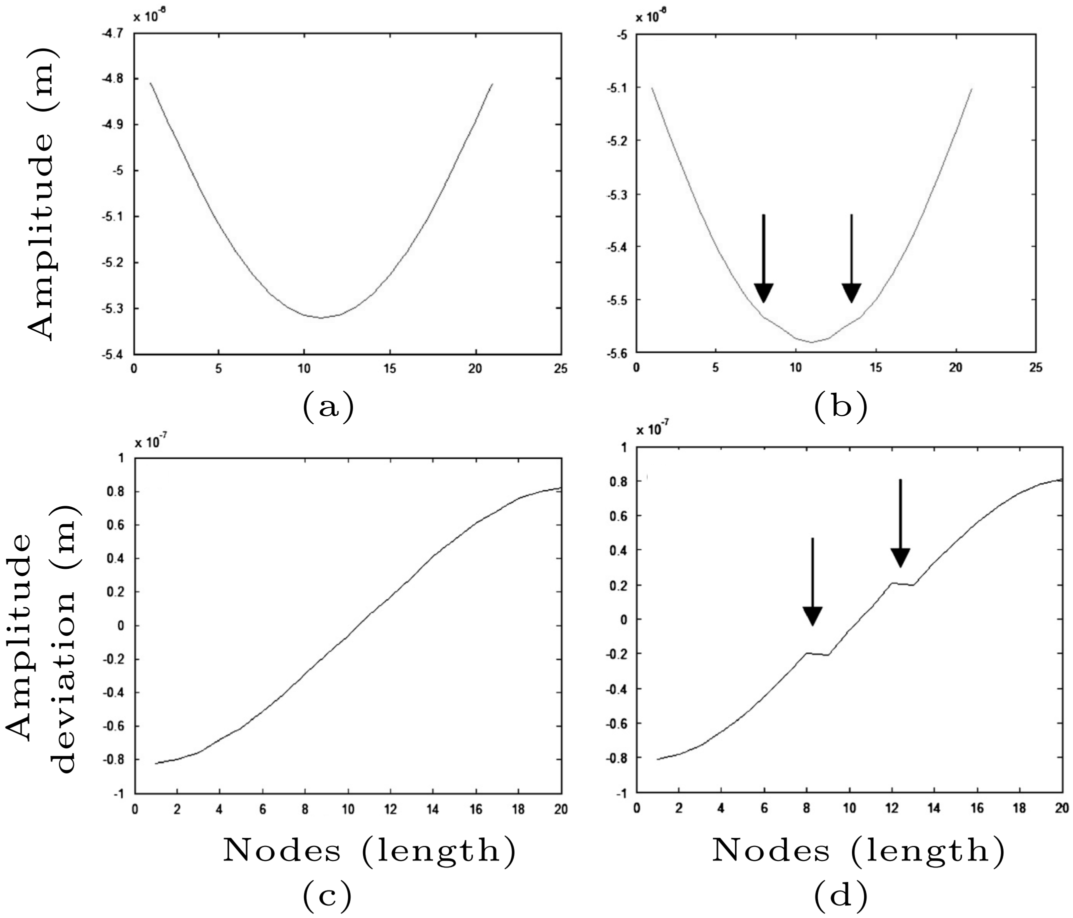

(a) (b)

(c) (d)

Figure 1.11: Comparison of operational deflection shapes (ODS) (a, b) and the slope derivation curve (SDC) (c, d) of the intact shaft (a, c) and the shaft with two cracks located on the 8th and 12th elements of the FE model (b, d) [88]

undetectable particularly in the presence of small crack depths. The study further introduced the concept of ADS or SDC, which relates to amplitude deviations of sequential points on the shaft, and showed that this new operator is more sensitive to changes in shaft deflection close to the crack location on the shaft, which may lead to the detection of smaller cracks. Figure 1.11 shows that the crack imposes sudden changes in the slopes of the resulting ODS and SDC. The results revealed notable changes in the slopes of the SDC in the vicinity of the cracks, which are not clearly evident in the ODS.

Sekhar [24] considered both forward and inverse problems to investigate the effects of two cracks on vibration responses of a shaft-rotor system. The method employed fictitious loads obtained from the FE model for identifying depths and locations of the cracks.

1.3 Scope and objectives of dissertation research

Despite the numerous reported studies on vibration-based crack detection methods, the efforts are continuing for developing more reliable crack indicators for real-time applications. From the literature review, it is evident that detection of cracks in rotary machines on the basis of vibration responses is promising but it poses many technical challenges. These include the characterization of responses of shaft-disc systems with stepped shaft and multiple discs, effects of other rotor faults, identifications of crack location, and identification and assessments of reliable crack detection methods for small size cracks, which have not been adequately addressed. Moreover, further efforts are desirable in applications of advanced signal processing methods and effects of external loads on the crack detection such as unbalance and external torsional torque in the shaft-disc system. In addition, different breathing functions have been introduced in order to more accurately describe the real breathing behavior of a crack on a rotating shaft; while the effect of these functions in detecting small size cracks has not been reported. Moreover, the breathing functions lack consideration of crack saturation effects. The main objective of this dissertation research is formulated so as to investigate vibration responses of a shaft-disc system with multiple discs and cracks via analytical and numerical methods, and to study correlations between changes in different vibration characteristics and the crack parameters including depth and location. The specific objectives are summarized below:

1. Develop analytical and numerical models of a shaft-disc system with single as

well as multiple cracks and discs on the shaft, and formulate a crack breathing function to account for saturation;

2. Modify the harmonic balance method to obtain harmonic as well as super-harmonic components of steady-state lateral response of the analytical shaft-disc model, and demonstrate validity of the analytical model together with the proposed solution strategy;
3. Analyze the analytical and numerical models for vibration analysis in the presence of single and two breathing cracks, and propose indicators for on-line detection of small size cracks using alternate signal processing methods;

1.4 Organization of the thesis

The dissertation research is conducted in five chapters. In Chapter 1, reported relevant studies are reviewed to attain adequate knowledge on different methods and their limitations and merits, and to formulate the scope of the dissertation research. The reviewed studies are systematically grouped into modeling of shaft-disc systems, crack modeling and crack indicators.

Chapter 2 presents the analytical and numerical models of the shaft-disc system. The equations of motion of the Jeffcott rotor model are initially described. Subsequently, an analytical model is formulated to incorporate a flexible shaft with two discs and cracks mounted together with different bearing supports. The shaft is modeled using the Timoshenko beam theory and the gyroscopic effects of the shaft and the discs are taken into account. The boundary conditions related to different types of bearing supports and continuity conditions corresponding to the cracks and disc are also formulated. Furthermore, a modified harmonic balance method is proposed to obtain the harmonic and super-harmonic components of the steady-state lateral response of the analytical model. The FE model of the shaft-disc system with two cracks is also described. Different crack models are summarized in this chapter and an alternate crack breathing function is also introduced. Finally, the methods of solution to obtain the transient and steady-state lateral responses of the shaft-disc system are described. The Hilbert-Huang transform based on EMD and improved EMD algorithms is also described, which is employed to obtain the time-frequency representations of transient lateral response of the shaft-disc system.

The experimental measurements and FE model of the shaft-disc system are employed to verify the validation of the modified harmonic balance method for obtaining the steady-state lateral response of the analytical model in Chapter 3. Moreover, the accuracy of the alternate crack breathing function, described in Chapter 2, for modeling the breathing behavior of the crack is examined through transient lateral response of the shaft-disc system passing through its first critical speed.

Chapter 4 presents the effect of cracks depths and locations on the selected vibrational properties such as critical speeds, shaft center orbits and harmonic and super-harmonic components of the steady-state and transient lateral responses the shaft-disc system. The effects of an alternate breathing function on detection of two cracks using frequency spectrum of the steady-state lateral response are investigated. The computational demands for obtaining transient lateral responses of the cracked shaft-disc system are also discussed. Furthermore, the results of employing the Hilbert–Huang transform based on EMD and improved EMD algorithms, described in Chapter 2, for finding small size cracks are compared.

Finally Chapter 5 summarizes the major contributions and conclusions of the dissertation research together with directions for future works.

Chapter 2

Shaft-Disc System, Crack Modeling and Methods of Solutions

2.1 Introduction

Constructing a reliable shaft-disc system model with a crack is the important initial step in a study on response analyses and crack detection methods. The model permits analyses of effects of a crack on changes in the dynamic behavior of the system, which are often considered as crack indicators. The model also provides the reference vibrational responses of the shaft-disc system without the crack. Applications of appropriate signal processing techniques form the subsequent essential step for identifying consistent changes in responses due to a crack and to establish correlations between the indicators and the crack parameters. This is a particular concern for detecting small size cracks.

Different analytical [e.g., 4–6, 38–40] and numerical [e.g., 41–43] shaft-disc models have been employed in various crack detection methods. The Jeffcott rotor model, a simplified analytical model with 2 degrees-of-freedom, has been widely used to obtain steady-state as well as transient lateral responses of a cracked rotor [e.g., 7, 8, 49, 50]. Although the Jeffcott rotor model does not consider the mass of the shaft and the gyroscopic effects, it provides reasonably good estimations of steady-state and transient lateral responses up to speeds below the second critical speed of the system. A more comprehensive model with higher degree-of-freedom, however, is essential to investigate the effects of crack properties (depth and location) on the first and higher critical speeds of the shaft-disc system. Such a model should also incorporate the gyroscopic effects.

The crack effect in a rotating machine is modeled in terms of changes in the local stiffness of the shaft in the vicinity of the crack. This effect can be estimated using fracture mechanics theory [2, 18] or by considering changes in the area moment of inertia about transverse coordinates at the location of the crack [37, 44]. An open crack induces constant stiffness reduction in the rotor system. A crack, however, tends to open or close during rotation, which is denoted as a breathing crack. In a breathing crack model, the crack is considered to open and close once per revolution of the shaft under the influence of the shaft's weight, while the deflection of the shaft due to the crack is considered negligible in comparison with that caused by the weight [62]. Different breathing functions, have been proposed to describe breathing behavior of the crack and to determine variations in the stiffness [e.g., 1, 3, 43, 55, 60, 89].

In this chapter, the governing equations of the lateral motion are formulated using the Jeffcott rotor model and analytical models of the shaft-disc system considering Timoshenko beam theory. An unbalance mass is introduced to excite lateral vibration of the system. The analytical model is developed considering two cracks and discs on different locations on the shaft mounted on rigid as well as flexible bearings. A finite element model of the shaft-disc system is also formulated. A modified harmonic balance method is proposed to evaluate the harmonic and super-harmonic components of the steady-state lateral response of the system containing breathing cracks, and consequently the preselected vibrational properties such as critical speeds and shaft center orbits. Additional flexibilities to the shaft near the crack are calculated using fracture mechanic concepts, and different breathing functions are described. Moreover, an alternate breathing function is proposed to model the crack opening and closing saturation in computing steady-state lateral response of the system using modified harmonic balance method. It is shown that the proposed alternate function reduced the computational demands of the model for transient response analysis.

2.2 Jeffcott rotor model

The Jeffcott rotor model considers a massless flexible shaft with a single rigid disc mounted on rigid-short bearing supports. The disc is located on the mid-span

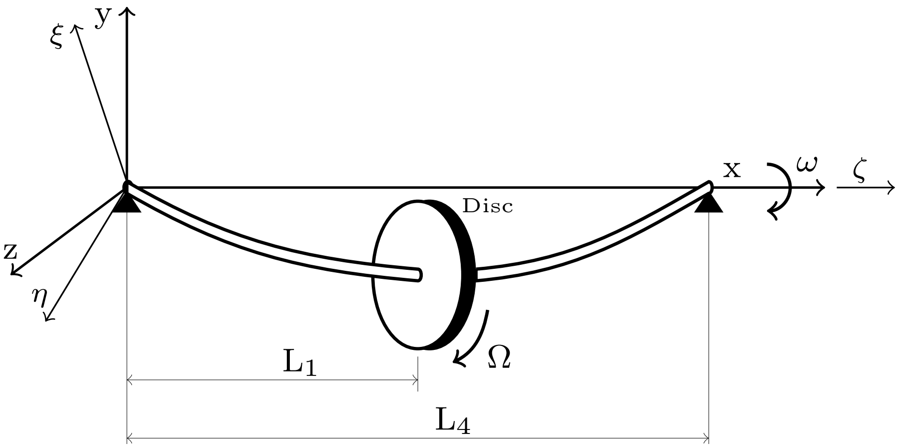

Figure 2.1: (a) A Jeffcott rotor model in the stationary coordinate (x, y, z) and rotating coordinate (ζ, ξ, η) frames

of the shaft, as shown in Figure 2.1. The equations describing the motion in the lateral directions in the stationary (x, y, z) and rotating (ζ, ξ, η) coordinates have been presented in [49, 64]. The equations of motion in the rotating coordinate, which rotates with the same speed of the shaft spin speed Ω, are given as [64]:

$$\begin{aligned}
&\begin{bmatrix} M_d & 0 \\ 0 & M_d \end{bmatrix} \begin{Bmatrix} \ddot{\xi} \\ \ddot{\eta} \end{Bmatrix} + \begin{bmatrix} C & -2M_d\Omega \\ 2M_d\Omega & C \end{bmatrix} \begin{Bmatrix} \dot{\xi} \\ \dot{\eta} \end{Bmatrix} + \\
&\begin{bmatrix} k_{\xi\xi} - M_d\Omega^2 & k_{\xi\eta} - \Omega C - M_d\alpha_r \\ k_{\eta\xi} + \Omega C + M_d\alpha_r & k_{\eta\eta} - M_d\Omega^2 \end{bmatrix} \begin{Bmatrix} \xi \\ \eta \end{Bmatrix} \\
&= M_d g \begin{Bmatrix} cos(\theta) \\ -sin(\theta) \end{Bmatrix} + M_d\varepsilon_d \begin{Bmatrix} \Omega^2 cos(\beta) + \alpha_r sin(\beta) \\ \Omega^2 sin(\beta) - \alpha_r cos(\beta) \end{Bmatrix}
\end{aligned} \tag{2.1}$$

where M_d, C, ε_d, g and β are the disc mass, external damping coefficient, unbalance eccentricity of the disc, gravitational acceleration and the angle between unbalance and ξ axis, respectively, as shown in Figure 2.2. In the above equation, $\theta(t), \Omega$ and α_r denote shaft rotational angle, rotational speed and acceleration rate, respectively. The stiffness matrix K_r is defined in the rotating system, as:

$$K_r = \begin{bmatrix} k_{\xi\xi} & k_{\xi\eta} \\ k_{\eta\xi} & k_{\eta\eta} \end{bmatrix} \tag{2.2}$$

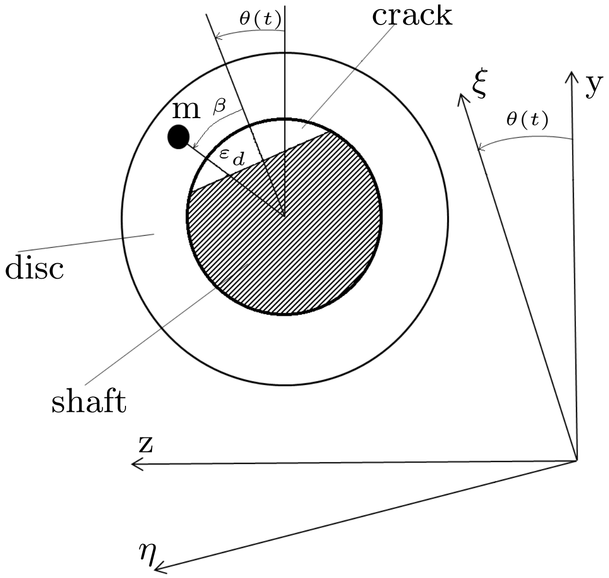

Figure 2.2: Stationary (x, y, z) and rotating (ζ, ξ, η) coordinate systems [3]

2.3 Analytical model of a shaft with two discs and cracks using Timoshenko beam theory

The governing equation of lateral motion of a continuous rotating shaft with two discs (Figure 2.3) is obtained using the Timoshenko beam theory [40], considering the gyroscopic moments, rotary inertia and shear deformation, as:

$$\begin{aligned} EI\frac{\partial^4 u}{\partial x^4} - \left(\frac{EI\rho}{kG} + \rho A r_0^2\right)\frac{\partial^4 u}{\partial x^2 \partial t^2} + 2i\rho A r_0^2 \Omega \frac{\partial^2 u}{\partial^2 x \partial t} + \\ \frac{\rho^2 A r_0^2}{kG}\frac{\partial^4 u}{\partial t^4} - 2i\frac{\rho^2 A r_0^2 \Omega}{kG}\frac{\partial^3 u}{\partial t^3} + \rho A \frac{\partial^2 u}{\partial t^2} = 0 \end{aligned} \tag{2.3}$$

where $u(x,t) = u_y(x,t) + iu_z(x,t)$ is lateral response of the system, in which u_y and u_z represent vertical and horizontal components of the response, respectively. The parameters E, I, k, G, A, r_0, ρ and Ω are the modulus of elasticity, shaft area moment of inertia about x-axis, shear factor, shear modulus, shaft cross-sectional area, radius of gyration $(\sqrt{I/A})$, mass density of the shaft and spin speed of the shaft, respectively.

To obtain the lateral response $u(x,t)$, the assumed solution function must satisfy boundary conditions of the rotating shaft in addition to compatibility relations at the cracks and discs locations. The flexible shaft with two discs is divided into three segments located on left- and right-sides of each disc. The coupled governing equations of lateral motion formulated for each segment are combined considering the appropriate continuity conditions. The governing equations describing lateral response of a flexible shaft with two transverse cracks can also be obtained in a similar manner [4, 38]. The effect of disc is incorporated into the continuity conditions in shear force and bending moments, while the crack effect is represented by a small but abrupt change in the slope continuity condition of the shaft, as described in section 2.3.2. The disc effects are related to its mass, and diametral and polar mass moment of inertia, while the crack effect depends on its depth and breathing behavior.

In the presence of two transverse cracks, as shown in Figure 2.3 (a), the governing equation of motion is formulated considering five separate segments ($s = 0, 1, 2, 3, 4$) of the shaft ($0 \leqslant x \leqslant L_0; L_0 \leqslant x \leqslant L_1; L_1 \leqslant x \leqslant L_2; L_2 \leqslant x \leqslant L_3$; and $L_3 \leqslant x \leqslant L_4$). In the model, $x = L_0$ and $x = L_3$, define locations of the two cracks, while $x = L_1$ and $x = L_2$ describes the discs location on the shaft of length L_4. Satisfying the continuity conditions at the location of the discs and the cracks simultaneously combined with Eq. (2.3) would yield lateral dynamic response of the entire cracked shaft-disc system. It is to be noted that $u^s(x,t)$ in Figure 2.3 represents the lateral displacement response of segment s of the flexible shaft, while ω is the whirling speed of the shaft.

2.3.1 Crack modeling

The presence of a transverse crack on a shaft causes a sudden change in the slope, which depends on crack depth and exhibits a reduction in the shaft local stiffness at the crack location. The crack-induced changes in local stiffness can be obtained using linear fracture mechanics theory [2, 3, 18, 50]. June et al. [3] have

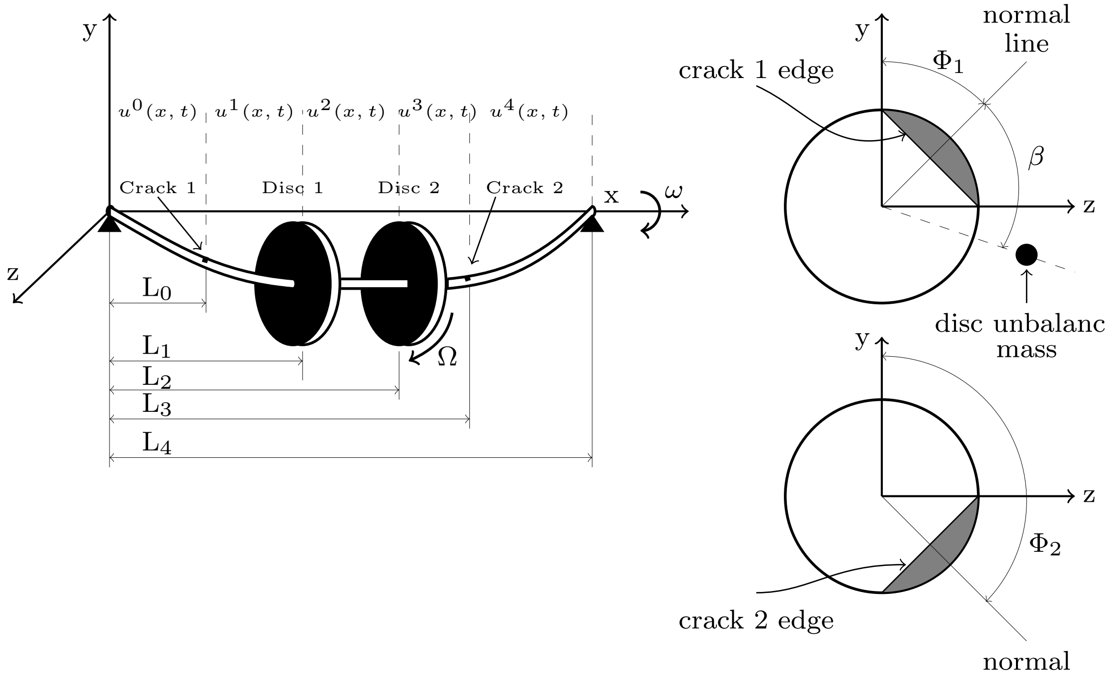

(a) (b)

Figure 2.3: (a) A continuous shaft-disc system with two cracks; and (b) Shaft cross-sections at the location of the crack 1 and crack 2

obtained the shaft flexibility due to a fully-open crack, as shown in Figure 2.4 (a). The study considered the strain energy density function, $J(\alpha)$, in terms of stress intensity factor K^I, as [3]:

$$\begin{aligned} J(\alpha) &= \frac{1}{E}\left(K^I\right)^2 \\ K^I &= K^I_{Q_\xi} + K^I_{Q_\eta} \end{aligned} \tag{2.4}$$

where $K^I_{Q_\xi}$ and $K^I_{Q_\eta}$ are the stress intensity factors corresponding to opening mode of the crack due to forces Q_ξ and Q_η acting on the cracked shaft cross-section, respectively, and can be described as [3]:

$$\begin{aligned} K^I_{Q_\xi} &= \frac{Q_\xi L_4 \alpha'/8}{I}\sqrt{\pi\alpha}F\left(\alpha/\alpha'\right) \\ K^I_{Q_\eta} &= \frac{Q_\eta L_4 w/4}{I}\sqrt{\pi\alpha}F'\left(\alpha/\alpha'\right) \end{aligned} \tag{2.5}$$

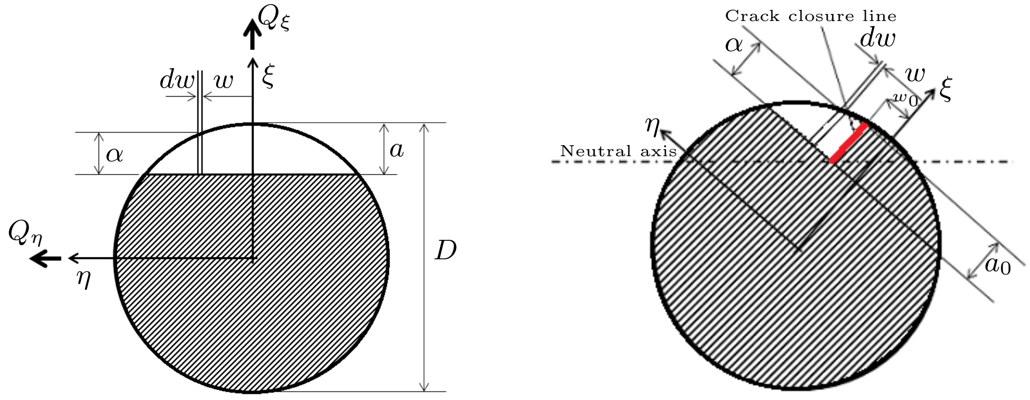

(a) (b)

Figure 2.4: Crack cross-section geometry, (a) fully-open crack, (b) partially open-closed crack [3]

The functions F and F' in the above relations are given by [3]:

$$\begin{aligned} F\left(\alpha/\alpha'\right) &= \sqrt{\frac{2\alpha'}{\pi\alpha} tan\left(\frac{\pi\alpha}{2\alpha'}\right)} \frac{0.923 + 0.199\left[1 - sin\left(\pi\alpha/2\alpha'\right)\right]^4}{cos\left(\pi\alpha/2\alpha'\right)} \\ F'\left(\alpha/\alpha'\right) &= \sqrt{\frac{2\alpha'}{\pi\alpha} tan\left(\frac{\pi\alpha}{2\alpha'}\right)} \frac{0.752 + 2.02\left[1 - sin\left(\pi\alpha/2\alpha'\right)\right]^3}{cos\left(\pi\alpha/2\alpha'\right)} \end{aligned} \tag{2.6}$$

where $I = \pi D^4/64$ and $\alpha' = \sqrt{D^2 - (2w)^2}$. In these equations, L_4 and D denote the length and diameter of the shaft, respectively. Using Castgliano's theorem, the additional deflections u_i $(i = \xi, \eta)$ due to the crack are obtained from [3]:

$$u_i = \frac{\partial U^c}{\partial Q_i} \tag{2.7}$$

where U^c represents the additional strain energy due to the crack, which can be written in term of strain energy density function $J(\alpha)$, as [3]:

$$U^c = \int\int J(\alpha) d\alpha dw \tag{2.8}$$

The additional flexibilities are thus given by [3]:

$$c_{ij} = \frac{\partial^2}{\partial Q_i \partial Q_j} \int_{-\sqrt{a(D-a)}}^{\sqrt{a(D-a)}} \int_0^{a - \frac{D}{2} + \sqrt{\frac{D}{4}^2 - w^2}} J(\alpha) d\alpha dw \tag{2.9}$$

Thereby, adding the flexibilities of the intact shaft to the obtained crack-induced flexibilities, described in Eq. (2.9), the compliance elements of the cracked shaft cross-area in ξ and η directions and the correspondence cross-coupled flexibilities can be described as [3]:

$$\begin{aligned} c_{\xi\xi} &= \frac{{L_4}^3}{48EI} + \int\int \frac{128{L_4}^2\alpha'^2}{E\pi D^8}\alpha F(\alpha/\alpha')^2 d\alpha dw \\ c_{\eta\xi} = c_{\xi\eta} &= \int\int \frac{256{L_4}^2\alpha' w}{E\pi D^8}\alpha F(\alpha/\alpha')F'(\alpha/\alpha') d\alpha dw \\ c_{\eta\eta} &= \frac{{L_4}^3}{48EI} + \int\int \frac{512{L_4}^2 w^2}{E\pi D^8}\alpha F'(\alpha/\alpha')^2 d\alpha dw \end{aligned} \tag{2.10}$$

Finally, the elements of the stiffness matrix K_r, described in Eq. (2.2), are obtained as:

$$K_r = C_r^{-1} = \begin{bmatrix} c_{\xi\xi} & c_{\xi\eta} \\ c_{\eta\xi} & c_{\eta\eta} \end{bmatrix}^{-1} \tag{2.11}$$

where,

$$k_{\xi\xi} = \frac{c_{\eta\eta}}{c_{\xi\xi}c_{\eta\eta} - c_{\xi\eta}^2}; k_{\eta\eta} = \frac{c_{\xi\xi}}{c_{\xi\xi}c_{\eta\eta} - c_{\xi\eta}^2}; k_{\xi\eta} = k_{\eta\xi} = \frac{-c_{\xi\eta}}{c_{\xi\xi}c_{\eta\eta} - c_{\xi\eta}^2} \tag{2.12}$$

In the above relation, the shaft compliance matrix C_r is defined in the rotational coordinates. The crack compliance matrix, C_{op}, for a fully-open crack in the y-z plane in the stationary coordinate system has also been derived using the strain energy release rate and Castigliano's theorem, which is generally expressed as [18]:

$$C_{op} = \begin{bmatrix} c_{yy} & c_{yz} \\ c_{zy} & c_{zz} \end{bmatrix} = \begin{bmatrix} cos(\theta(t)) & -sin(\theta(t)) \\ sin(\theta(t)) & cos(\theta(t)) \end{bmatrix} \begin{bmatrix} c_{\xi\xi} - \frac{{L_4}^3}{48EI} & c_{\xi\eta} \\ c_{\eta\xi} & c_{\eta\eta} - \frac{{L_4}^3}{48EI} \end{bmatrix} \tag{2.13}$$

A crack can be modeled as an open crack or a breathing crack. The crack may be modeled as an open crack when dependence of the local stiffness change on the shaft angle is considered negligible. However, it has been shown that the stiffness reduction is strongly related to shaft angle of rotation. The crack is thus more accurately modeled as a breathing crack, where the crack opens and closes during each revolution of the shaft.

The effect of shaft rotation on the crack behavior is modeled using a breathing function multiplied by the fully-open crack compliance matrix, C_{op}, such that:

$$C_{br} = f(t)C_{op} \tag{2.14}$$

where $f(t)$ $(0 \leqslant f(t) \leqslant 1)$ is the breathing function. A breathing function is a periodic function with period $2\pi/\Omega$. During each shaft revolution, the crack may close fully ($C_{br} = 0$), and approach fully-open ($C_{br} = C_{op}$) or partially open ($C_{br} \leqslant C_{op}$) conditions. A periodic breathing function, proposed by Mayes and Davies [60], has been widely employed, and is given by:

$$f(t) = \frac{1 - cos(\Omega t + \Phi_r)}{2} \tag{2.15}$$

where $\Phi_r (r = 1, 2)$ define the angles between the crack edge normal line and vertical axis, as shown in Figure 2.3 (b). In this study, the breathing function in Eq. (2.15) is formulated in the exponential form, which can facilitate steady-state solution of equations of motion of the shaft-disc system using the modified harmonic balance method, as described in section 2.5, such that:

$$f(t) = \frac{1}{2} - \frac{1}{4}\left(e^{i(\Omega t + \Phi_r)} + e^{-i(\Omega t + \Phi_r)}\right) \tag{2.16}$$

Proposal for an alternate breathing function

A crack in a shaft may exhibit saturation in opening and closing during rotation. This saturation may alter the amplitude of peaks in frequency spectrum of lateral response of the shaft-disc system, which is believed to serve as a better indicator of presence of the second crack. An alternate explicit breathing function is thus proposed to account for saturation of crack breathing behavior using a softly-clipped cosine function, such that:

$$f(t) = \frac{1}{2} - \frac{5}{9} cos(\Omega t + \Phi_r) - \frac{1}{18} cos(3\left(\Omega t + \Phi_r\right) - \pi) \tag{2.17}$$

It is evident that the periodic function in Eq. (2.15) leads to fully-open or closed crack at an instant when shaft angle approaches ($\theta = \pm\frac{n\pi}{2}, n = 0, 1, 2, \ldots$). The modified explicit breathing function in Eq. (2.17), on the other hand yields saturation in opening or closing over a range of shaft angle. In the saturation

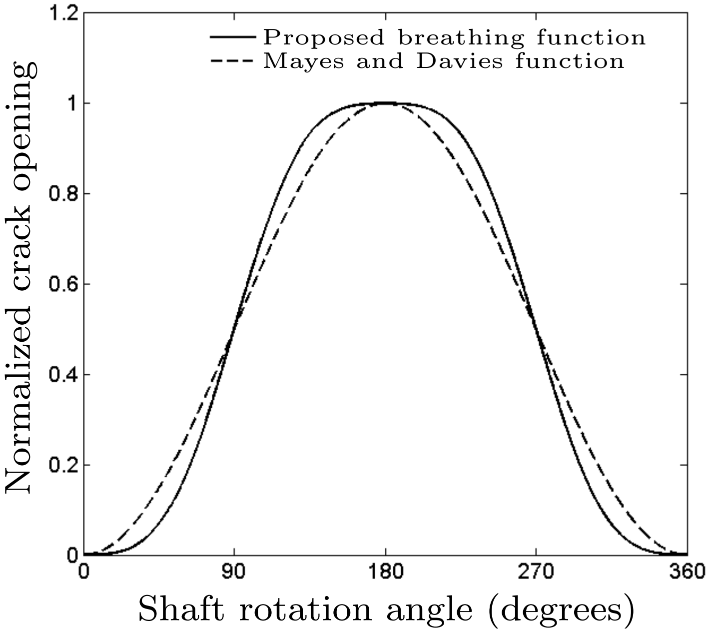

Figure 2.5: Comparison of the proposed breathing function with that reported by Mayes and Davies [60]

intervals, the crack locates completely in either tensile or compressive stress zones of the shaft and remains either fully-open or closed over certain period of angle of rotation. Figure 2.5 compares the normalized crack opening obtained from the proposed periodic breathing function and that from the Mayes and Davies function. The comparison clearly illustrates that the proposed function can describe crack opening and closing saturation.

The proposed breathing function also contains the term $cos(3\Omega t + \Phi_r)$ which leads to distribution of the energy dissipation originated from crack saturation among more number of harmonic components of the lateral response using the modified harmonic balance method, described in section 2.5, and may contribute to relatively lower amplitudes of harmonic and super-harmonic components. Modeling the crack breathing behavior more accurately considering the saturation phenomenon may thus yield relatively lower amplitude peaks in the lateral response spectrum. Mayes and Davies breathing function [60], Eq. (2.15), does not account for saturation in crack breathing and subsequently the energy dissipation due to crack saturation, which may lead to lateral response peaks with relatively higher amplitudes.

Moreover, a few studies have reported that the compliance matrix for a breathing crack varies periodically versus the shaft angle [2–4, 43, 50]. A number of reported crack breathing models, however, do not provide an explicit function for application in the modified harmonic balance method, described in section 2.5. The proposed explicit function can also be expressed in the exponential form to facilitate its application to the modified harmonic balance method, such that:

$$f(t) = \frac{1}{2} - \frac{5}{18}\left(e^{i(\Omega t+\Phi_r)} + e^{-i(\Omega t+\Phi_r)}\right) - \frac{1}{36}\left(e^{i((3\Omega t+\Phi_r)-\pi)} + e^{-i((3\Omega t+\Phi_r)-\pi)}\right) \quad (2.18)$$

As described earlier, Jun et al. [3] provided the stiffness of a fully-open cracked shaft. Furthermore, to obtain the localized stiffness of a shaft with a partially open/closed crack based on the model of Jun et al. [3], Darpe et al. [50] have proposed concept of crack closure line (CCL) as shown in Figure 2.4 (b). This concept is based on the sign of the stress intensity factor at the crack edge. The stress intensity factor for each point at the crack edge on the left side of the CCL carries a positive sign, which indicates that the crack is in tension and thus open mode. The crack is considered to be closed on the right side of the CCL due to a negative stress intensity factor. While Eq. (2.9) is equally applicable, the lower and upper limits in the double integral are updated based on the position of the CCL, as [50]:

$$c_{ij} = \frac{\partial^2}{\partial Q_i \partial Q_j} \int_{-a\sqrt{(D-a)}}^{w_0} \int_0^{a_0} J(\alpha) d\alpha dw \quad (2.19)$$

The breathing crack model proposed by Darpe et al. [50] can accurately describe the breathing behavior of the crack at each shaft angle. The model, however, poses substantial computational demands. In this study, an alternate explicit breathing function, proposed in Eq.(2.17), is used to reduce the computational efforts.

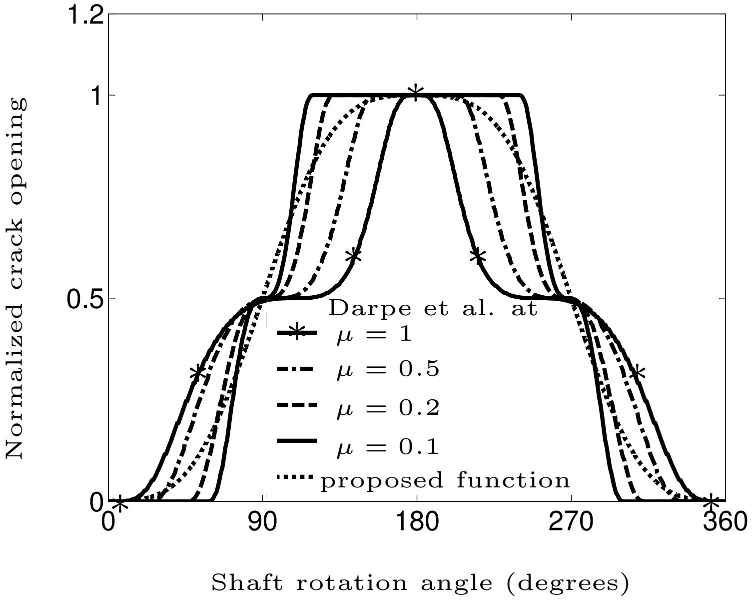

Figure 2.6: Comparison of the proposed breathing function with that reported by Darpe et al. [50] breathing model

Figure 2.6 compares the proposed breathing function, Eq. (2.17), with that of Darpe et al. [50]. It is noted that the pattern of the Darpe et al. [50] breathing model changes as the normalized crack depth ($\mu = \frac{a}{R}$, ratio of the crack depth a to the shaft radius R) changes. The pattern of the proposed breathing function is, however, independent to the normalized crack depth. The comparisons show that the proposed function gives good approximation of Darpe et al. [50] breathing model, particularly for small cracks.

2.3.2 Boundary and continuity conditions

The boundary conditions of shaft-disc systems with rigid-short bearing supports have been described in a number of studies. Assuming negligible resistance to bending moments, the boundary conditions can be expressed as [4]:

$$\frac{\partial^2 u^0}{\partial x^2}(0,t) = \frac{\partial^2 u^4}{\partial x^2}(L_4,t) = 0 \tag{2.20}$$

where L_4 is shaft length. Rigidity of supports also leads to following displacement boundary conditions:

$$u^0(0,t) = u^4(L_4,t) = 0 \tag{2.21}$$

For the flexible-long bearing supports, the slopes of the shaft vanish in the lateral direction in the vicinity of the supports, such that:

$$\frac{\partial u^0}{\partial x}(0,t) = \frac{\partial u^4}{\partial x}(L_4,t) = 0 \tag{2.22}$$

Furthermore, for the flexible-long bearing supports, the shear force developed in the shaft is related to the bearing stiffness and the shaft deflection, such that [4]:

$$\begin{aligned}
&V^0(0,t) = -EI\frac{\partial^3 u^0(0,t)}{\partial x^3} + \rho A r_0^2\left(\frac{\partial^3 u^0(0,t)}{\partial x \partial t^2} - 2i\Omega\left(\frac{\partial^2 u^0(0,t)}{\partial x \partial t}\right)\right) = \\
&(S_1 + iS_4)\,u^0(0,t) + (S_2 + iS_3)\,conj\left(u^0(0,t)\right) \\
&V^4(L_4,t) = -EI\frac{\partial^3 u^4(L_4,t)}{\partial x^3} + \rho A r_0^2\left(\frac{\partial^3 u^4(L_4,t)}{\partial x \partial t^2} - 2i\Omega\left(\frac{\partial^2 u^4(L_4,t)}{\partial x \partial t}\right)\right) = \\
&(S_1 + iS_4)\,u^4(L_4,t) + (S_2 + iS_3)\,conj\left(u^4(L_4,t)\right)
\end{aligned} \tag{2.23}$$

where $conj(u^s(x,t))$ returns the complex conjugate of $u^s(x,t)$, and $S_1 = \frac{1}{2}(k_{yy} + k_{zz})$, $S_2 = \frac{1}{2}(k_{yy} - k_{zz})$, $S_3 = \frac{1}{2}(k_{yz} + k_{zy})$ and $S_4 = \frac{1}{2}(k_{yz} - k_{zy})$ are defined using the stiffness properties of the flexible bearing, $\mathrm{K_b}$, which may be expressed as:

$$\mathrm{K_b} = \begin{bmatrix} k_{yy} & k_{yz} \\ k_{zy} & k_{zz} \end{bmatrix} \tag{2.24}$$

The shear force developed within the shaft segment $V^s(x,t)$, $(s = 0,1,2,3,4)$, is obtained for the Timoshenko shaft with gyroscopic effects, as [39]:

$$V^s(x,t) = -EI\frac{\partial^3 u^s(x,t)}{\partial x^3} + \rho A r_0^2\left(\frac{\partial^3 u^s(x,t)}{\partial x \partial t^2} - 2i\Omega\left(\frac{\partial^2 u^s(x,t)}{\partial x \partial t}\right)\right) \tag{2.25}$$

The continuity conditions for the shaft near the crack location have also been described by Chasalevris and Papadopoulos [4], when the disc and the crack are located at the same position on the shaft. The continuity conditions for the shaft considering multiple cracks and different locations of the discs and cracks may also be formulated in a similar manner. Assuming negligible contributions of disc mass and inertia to the slopes and displacements on the left- and right-sides of the disc, the displacement and slope continuity equations at the discs locations can be expressed as:

$$u^p(L_p, t) = u^{p+1}(L_p, t) \tag{2.26}$$

$$\frac{\partial u^p}{\partial x}(L_p, t) = \frac{\partial u^{p+1}}{\partial x}(L_p, t) \tag{2.27}$$

where L_p $(p = 1, 2)$ denotes the discs locations on the shaft, as shown in Figure 2.3 (a). The disc mass, however, yields abrupt change in shear force developed in adjacent segments of the shaft on both sides of the disc, which is given by:

$$EI\left(\frac{\partial^3 u^p(L_p, t)}{\partial x^3} - \frac{\partial^3 u^{p+1}(L_p, t)}{\partial x^3}\right) + \rho A r_0^2 \left(\frac{\partial^3 u^p(L_p, t)}{\partial x \partial t^2} - \frac{\partial^3 u^p(L_p, t)}{\partial x \partial t^2}\right)$$
$$+2i\rho A r_0^2 \Omega \left(\frac{\partial^2 u^p(L_p, t)}{\partial x \partial t} - \frac{\partial^2 u^{p+1}(L_p, t)}{\partial x \partial t}\right) = M_{D,p} \frac{\partial^2 u^p\,(L_p, t)}{\partial t^2} + (2 - p) m_u r_u \Omega^2 e^{i(\Omega t + \beta)} \tag{2.28}$$

where $M_{D,p}$ (p $= 1, 2$), m_u, r_u and β represent the masses of the discs, unbalance mass, eccentricity and angular position of the unbalance. β is defined as the angle between the normal line of the first crack and the unbalance mass, as shown in Figure 2.3 (b). The above force continuity equation is formulated considering an unbalance mass located on the disc 1. Furthermore, the disc mass moments of inertia affects the shaft bending moment, such that:

$$EI\left(\frac{\partial^2 u^{p+1}(L_p, t)}{\partial x^2} - \frac{\partial^2 u^p(L_p, t)}{\partial x^2}\right) = I_{D,p} \frac{\partial^3 u^p(L_p, t)}{\partial x \partial t^2} - i I_{P,p} \Omega \frac{\partial^2 u^p(L_p, t)}{\partial x \partial t} \tag{2.29}$$

where $I_{D,p}$ and $I_{P,p}$ $(p = 1, 2)$ denote the disc diametral and polar mass moment of inertias. The displacement continuity at the cracks location can be expressed as:

$$u^p(L_p, t) = u^{p+1}(L_p, t) \tag{2.30}$$

where L_p $(p = 0, 3)$ describes location of crack on the shaft. The presence of a crack between two consecutive shaft segments imposes a sudden change in slopes of displacements of shaft segments in the lateral direction. The slope continuity equation of the two adjacent segments at the crack location is thus expressed as:

$$\begin{aligned} &\frac{\partial u^{p+1}}{\partial x}(L_p, t) - \frac{\partial u^p}{\partial x}(L_p, t) = \\ &EI\left(\left(\beta^r - i\nu^r\right) f^r(t) \frac{\partial^2 u^p}{\partial x^2}(L_p, t) + \left(\epsilon^r - i\delta^r\right) f^r(t) conj\left(\frac{\partial^2 u^p}{\partial x^2}(L_p, t)\right)\right) \end{aligned} \tag{2.31}$$

where the parameters $\beta^r, \nu^r, \epsilon^r$ and δ^r represent the effect of a breathing crack and depend on the crack depth. The superscript $r = 1, 2$ denotes the number of the crack, as shown in Figure 2.3. These parameters are defined using the compliance matrix, described in Eq. (2.13), such that:

$$\epsilon^r = \frac{\left(c^r_{zz} - c^r_{yy}\right)}{2}; \beta^r = \frac{\left(c^r_{zz} + c^r_{yy}\right)}{2}; \delta^r = \frac{\left(c^r_{yz} + c^r_{zy}\right)}{2}; \nu^r = \frac{\left(c^r_{yz} - c^r_{zy}\right)}{2} \tag{2.32}$$

The shear force and bending moment continuity between the adjacent shaft segments in the vicinity of the crack are independent of the crack properties, and are formulated, as:

$$\begin{aligned} &EI\left(\frac{\partial^3 u^p(L_p, t)}{\partial x^3} - \frac{\partial^3 u^{p+1}(L_p, t)}{\partial x^3}\right) + \rho A r_0^2\left(\frac{\partial^3 u^{p+1}(L_p, t)}{\partial x \partial t^2} - \frac{\partial^3 u^p(L_p, t)}{\partial x \partial t^2}\right) \\ &+ 2i\rho A r_0^2 \Omega\left(\frac{\partial^2 u^p(L_p, t)}{\partial x \partial t} - \frac{\partial^2 u^{p+1}(L_p, t)}{\partial x \partial t}\right) = 0 \end{aligned} \tag{2.33}$$

$$\frac{\partial^2 u^{p+1}(L_p, t)}{\partial x^2} = \frac{\partial^2 u^p(L_p, t)}{\partial x^2} \tag{2.34}$$

The boundary and continuity conditions, described in Eqs. (2.20) – (2.34), are used in conjunction with the governing equation of motion of the analytical model in Eq.(2.3) to obtain the steady-state lateral vibration response of the shaft-disc system using the modified harmonic balance method.

2.4 FE model of the cracked shaft-disc system

A FE model of a shaft with a single rigid disc is formulated, as reported in [44, 55, 90], to evaluate its lateral dynamic response in the presence of a breathing crack so as to examine validity of the analytical model. In the model, the shaft is discretized using two-node Timoshenko beam elements considering different number of elements in the shaft segments [44, 55]. The governing equations of motion of the shaft supported on flexible foundations, as shown in Figure 2.7, can be described in the finite element form, as [55]:

$$(M_T^e + M_R^e)\,\ddot{U}^e + G^e\dot{U}^e + K^eU^e = F^e \tag{2.35}$$

where U^e is a 8×1 element nodal displacement vector comprising four degree-of-freedom (vertical and horizontal displacements, and rotations about the vertical and horizontal axes) for each node. M_T^e, M_R^e, K^e and G^e are the translational mass, rotary mass, stiffness and gyroscopic effect matrices for each element, respectively. F^e accounts for the unbalance and gravitational forces at each node. The equation of motion for the rigid disk in Figure 2.7 is subsequently formulated, as:

$$\left(M_T^d + M_R^d\right)\ddot{U}^d + G^d\dot{U}^d = F^d \tag{2.36}$$

where U^d is the disc center nodal displacement vector combining lateral displacements and slopes about the y- and z-axes. M_T^d, M_R^d and G^d are the translational mass, rotary mass and gyroscopic effect matrices of the rigid disk, respectively, and vector F^d represents the unbalance and gravitational forces on the disc. Combining the equations of motion of the shaft elements and the rigid disk, the equation of motion of the shaft-disc system with two breathing cracks can be described as:

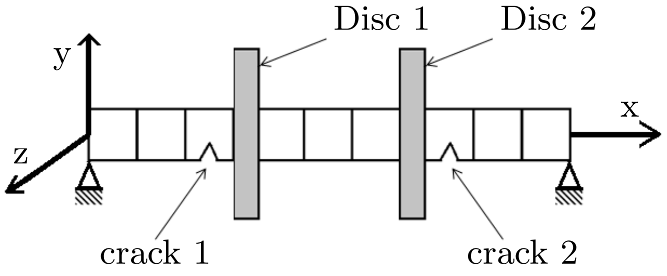

Figure 2.7: FE model of a cracked shaft-disc system

$$M\ddot{U} + C\dot{U} + \left(K - \sum_{r=1}^{2} f^r(t)K_C^r\right)U = F \tag{2.37}$$

where M is the mass matrix integrating the shaft and disc mass matrices, C includes the shaft and the rigid disc gyroscopic effect matrices, K describes the stiffness of the shaft and F represents the unbalance and gravitational forces imposed on the shaft-disc system. K_C^r represents the stiffness matrix of the shaft element containing rth $(r = 1, 2)$ crack and $f^r(t)$ is corresponding crack breathing function, described in section 2.3.1. Furthermore, in order to model the effect of the short and long bearing supports in Eq. (2.37), the influence of the bending moments and slopes are neglected at the supports, respectively.

2.5 Modified harmonic balance method

It has been reported that modeling the crack as a breathing crack leads to excitations of the super-harmonic components of the lateral response of a shaft-disc system [e.g., 6, 55]. The harmonic balance method can provide effective estimations of these super-harmonic components [55]. The method assumes the solution as a linear combination of basic harmonic functions corresponding to multiples of the whirling speed, such that:

$$u\left(x,t\right) = \sum_{n=1}^{m} \Phi_n(x) G_n(t) = \sum_{n=1}^{m} \Phi_n(x) \left(A_n cos\left(n\omega t\right) + B_n sin\left(n\omega t\right)\right) \tag{2.38}$$

where m is number of harmonics considered in the response and n is the order of the super-harmonics. $\Phi_n(x)$ and $G_n(t)$ represent the space- and time-dependent nth super-harmonic components of the lateral response, respectively.

The harmonic balance method has been widely used to obtain the super-harmonic components of the lateral response of FE model of a shaft-disc system [e.g., 44, 55]. The majority of the reported studies, using an analytical model of shaft-disc system, assume the solution in the following form, which yields only the first harmonic of the lateral response [e.g., 4, 38]:

$$u\left(x,t\right) = \Phi(x) e^{i\omega t} \tag{2.39}$$

In this study, an alternate modified assumed solution is proposed in order to capture higher order super-harmonic components of the lateral response of an analytical shaft-disc system, such that:

$$u\left(x,t\right)=\sum_{n=1}^{m}\Phi_n(x)\left(e^{in\omega t}+e^{-in\omega t}\right) \tag{2.40}$$

where $e^{in\omega t}$ describes the forward whirling response, while $e^{-in\omega t}$ relates to the backward whirling response. Unbalance force may excite backward whirling of an asymmetric shaft or a symmetric shaft supported on anisotropic bearing supports [91, 92]. In this study, a symmetric shaft mounted on isotropic bearings is considered. The assumed solution, thus, is limited only to forward whirling term assuming that the unbalance force is synchronized to the frequency of the shaft speed, $\omega = \Omega$, such that:

$$u\left(x,t\right)=\sum_{n=1}^{m}\Phi_n(x)e^{in\omega t} \tag{2.41}$$

The space dependent nth super-harmonic component of the lateral response,$\Phi_n(x)$, is described by:

$$\Phi_n(x)=A_n e^{\alpha_n x} \tag{2.42}$$

where the coefficients A_n and exponents α_n are obtained from simultaneous solutions of the coupled governing equation of lateral motion described in Eq. (2.3), and the assumed solution in Eq. (2.41). The substitution of assumed solution in Eq. (2.3) yields the following characteristic equation in α_{jn}:

$$\begin{aligned}EI\alpha_{jn}^4+\left[\left(\frac{EI\rho}{kG}+\rho A r_0^2\right)n^2\omega^2-2\rho A r_0^2\Omega n\omega\right]\alpha_{jn}^2+\\ \frac{\rho^2 A r_0^2}{kG}n^4\omega^4-\frac{2\rho^2 A r_0^2\Omega}{kG}n^3\omega^3-\rho A n^2\omega^2=0\end{aligned} \tag{2.43}$$

where α_{jn} $(j = 1, 2, 3, 4)$ are the roots of the above characteristic equation. The assumed solution in Eq. (2.41) can thus be rewritten as:

$$u\left(x,t\right)=\sum_{n=1}^{m}\left(\sum_{j=1}^{4}A_n^j e^{\alpha_{jn}x}e^{in\omega t}\right) \tag{2.44}$$

The coefficient vector $\{A_n^j\}$ in the proposed solution is obtained considering the continuity conditions between adjacent segments of the shaft and the boundary conditions. The proposed solution, Eq. (2.44), is in the exponential form. The crack breathing functions in the exponential form, described in Eq. (2.16) and (2.18), can thus be easily employed in the crack slope continuity condition, Eq. (2.31), for determining $\{A_n^j\}$.

2.6 Methods of solutions

In this section, the methods of obtaining the steady-state and transient lateral responses of analytical and FE models of the cracked shaft-disc system are described, receptively. Moreover, the decomposition algorithms required to find the time-frequency representation of the vertical transient response of the Jeffcott rotor model are also explained in the following.

2.6.1 Steady-state response

The analyses are performed considering different types of bearing supports for the shaft-disc system. These include short/ long and rigid/ flexible bearing supports. Substituting the proposed solution in the modified harmonic balance method, described in Eq. (2.44), into the boundary and continuity conditions of the shaft-disc system, yields a system of algebraic equations:

$$[\Delta]\{A\} = \{B\} \tag{2.45}$$

where vector $\{A\}$ represents the coefficients of harmonic and super-harmonic components in the proposed solution for each segment of the shaft. Vector $\{B\}$ describes the harmonic external forces acting on each segment of the shaft. In the above, $[\Delta]$ is the matrix of coefficients, which depends on selected crack breathing function and bearing support type. The solution of the system of linear equations yields the coefficients of harmonic and super-harmonic components, and subsequently the lateral responses of the system. A detailed formulation of Eq. (2.45) is presented in the Appendix.

For each shaft speed, the lateral responses of the shaft-disc system are also evaluated from the FE model considering eigen solutions of Eq. (2.37) together with the assumed solution in Eq. (2.38). The resultant eigenvalues are the coefficients of the harmonic and super-harmonic components of the lateral response, A_n and B_n, as described in Eq. (2.38). The length of the cracked element influences the shaft local stiffness and consequently the lateral response of the FE model. The cracked element length for each crack depth in the FE model is chosen so as to yield the first critical speed identical to that obtained from the analytical model.

2.6.2 Transient response

Considering the stiffness matrix described in Eq. (2.11), the governing equation of motion, Eq. (2.1), is integrated using fourth order Runge-Kutta method to compute the transient start-up responses of the system with different crack depths and acceleration rates. The integration of Eq. (2.1) is carried out using sufficiently small time step ($\Delta t = 0.001$) for accurate solutions. In each time step, the stiffness values and shaft speed are considered to be constant. The shaft speed Ω and angular position θ are constantly updated using [64]:

$$\begin{aligned} \Omega(t) &= \Omega_0 + \alpha_r t, \text{ for } \Omega_0 = 0 \\ \theta(t) &= \theta_0 + \Omega_0 t + \frac{\alpha_r t^2}{2}, \text{ for } \theta_0 = 0 \end{aligned} \tag{2.46}$$

where α_r denotes the acceleration rate of the shaft. The obtained lateral forces at each shaft angle, described in Eq. (2.47), are also used to update the stiffness values for the next time step using the crack breathing behavior models described in section 2.3.1, such that:

$$\begin{Bmatrix} Q_\xi \\ Q_\eta \end{Bmatrix} = \begin{bmatrix} k_{\xi\xi} & k_{\xi\eta} \\ k_{\eta\xi} & k_{\eta\eta} \end{bmatrix} \begin{Bmatrix} \xi \\ \eta \end{Bmatrix} \tag{2.47}$$

The initial displacement of the rotor in the vertical direction is assumed to be equal to the static deflection, while the initial horizontal displacement is set to 0. The rotor starts from the static position with a given constant acceleration rate α_r. Figure 2.8 shows the flowchart of the above described solution method for transient lateral response analysis of the shaft-disc system.

The super-harmonic components of lateral response of the shaft-disc system passing through critical speeds are excited due to the presence of the breathing crack. The emergence of these super-harmonic components is not clearly observable in the time response particularly for the small cracks. However, using time-frequency analysis based on different transforms may reveal the crack-induced changes in transient response. A brief description on time-frequency analysis used in crack detection in rotary systems is presented in the following section.

2.6.3 Time-frequency analysis

The Fourier transform is a well-known method to analyze stationary vibration signals. The Fourier transform method, however, is not well-suited for determination of local changes in frequency contents of the cracked rotor transient responses, which generally exhibit non-stationary behavior. The Short Time Fourier Transform (STFT) has been developed to analyze non-stationary signals. In STFT-based time-frequency representations, an identical window is used for analysis of the entire signal, which leads to a constant resolution for all frequencies. However, generally wide and narrow windows are required to obtain a good frequency resolution for low and high frequency components of a signal, respectively.

Alternatively, the wavelet transform can produce a multi-scale frequency resolution to extract more effective time-frequency representation of non-stationary

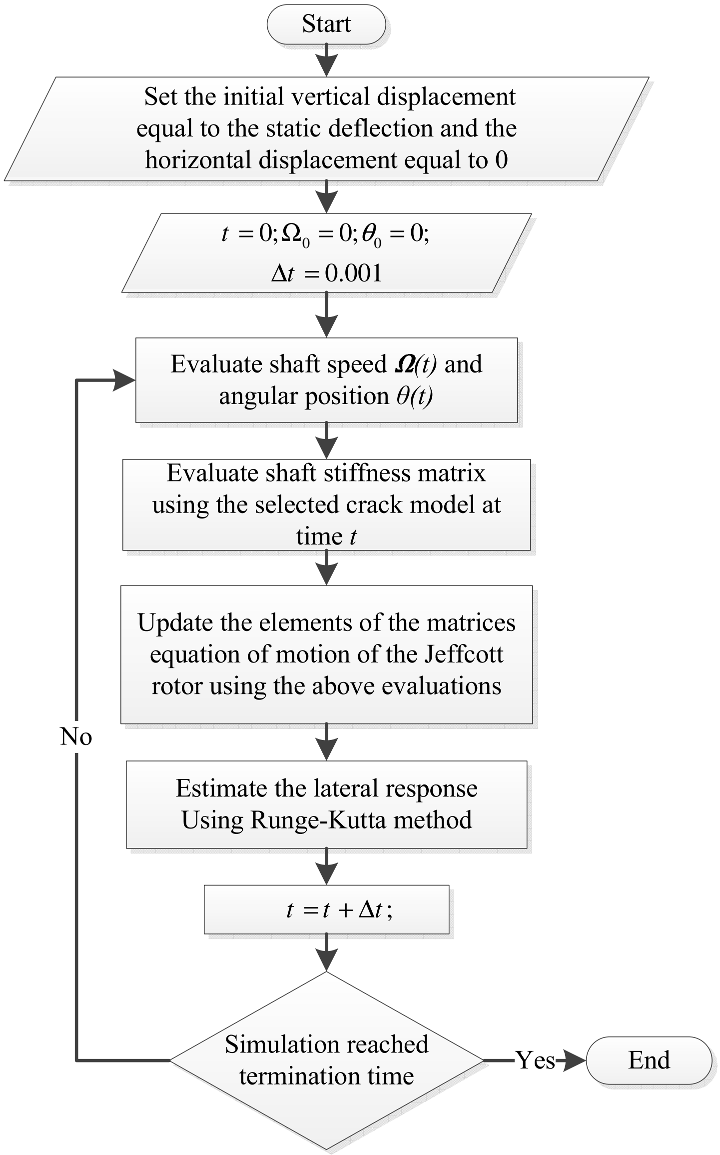

Figure 2.8: The transient lateral response solution flowchart

signals. In wavelet transform, signal features, which are well correlated with the shape of the selected wavelet mother function have a higher chance to be observed in the time-frequency representation, while the features with lower correlations vanish. Therefore, the wavelet transform is a non-adaptive signal processing method. An alternate self-adaptive method, namely, the empirical mode decomposition is capable of determining the time-frequency representation based on the signal itself rather than preselected kernels. This method has shown to overcome the STFT and wavelet transform disadvantages.

2.6.4 Empirical Mode Decomposition (EMD)

Huang et al. [69] presented the empirical mode decomposition algorithm, which is a post-processing method to decompose non-stationary signals into a set of intrinsic mode functions (IMFs). The IMFs represent simple oscillatory signals, which are suitable for computation of instantaneous frequencies, and satisfy the following two conditions: (i) in the entire data set, the number of local extrema and the zero–crossings must either be equal or differ at most by one; and (ii) at any time instant t, the mean values of the upper and lower envelopes of an IMF is zero. Using EMD method, the original signal $u(t)$ can be reconstructed as:

$$u(t) = \sum_{n=1}^{m} c_n(t) + x_m(t) \tag{2.48}$$

where $c_n(t)$ is the IMF and m is the number of total extracted IMFs. $x_m(t)$ represents the residual signal. The IMFs are determined by a simple algorithm, namely, sifting process as follows: (i) the local extrema of the signal $h_{n,l-1}$ ($h_{1,0} = u(t)$) are identified, where the subscripts n and l denote the number of IMF and number of sifting iteration corresponding to the nth IMF, respectively; (ii) the upper $U(t)$ and lower $L(t)$ envelops are constructed by interpolating on the local minima and maxima, respectively, using a cubic spline interpolation algorithm; respectively. (iii) the instantaneous mean $m(t)$ of the upper and lower envelops is computed from

$$m(t) = \frac{U(t) + L(t)}{2}; \text{ and} \tag{2.49}$$

(iv) the instantaneous mean is subtracted from the signal $h_{n,l-1}$, as

$$h_{n,l}(t) = h_{n,l-1}(t) - m(t) \tag{2.50}$$

The steps (i)–(iv) are repeated until the mean of $h_{n,l}(t)$ can be considered zero according to the stop criterion of the sifting process. Once the stop criterion is satisfied, the resulting $h_{n,l}(t)$ is taken as the nth IMF, such that:

$$c_n(t) = h_{n,l}(t) \tag{2.51}$$

The subsequent IMF function can be obtained considering the $(n+1)^{th}$ residual signal $x_{n+1}(t) = u(t) - \sum_{j=1}^{n} c_j(t)$ as the new original signal, and the sifting process is repeated. The sifting process terminates as the desired number of IMFs (m) are obtained or the residual signal $x_n(t)$ is a monotonic signal (a signal with no extrema). The sifting process to calculate the IMFs is illustrated in Figure 2.9. The instantaneous frequency, IF, of each IMF is obtained from:

$$IF_n(t) = \frac{d(arctan(H[c_n(t)]/c_n(t)))}{dt} \tag{2.52}$$

where $H[.]$ denotes the Hilbert transform operation [93]. Huang et al. [69] introduced the Hilbert-Huang transform (HHT), in which the combination of Hilbert transform and EMD is employed to determine time-frequency representation or instantaneous frequency of non-stationary signals. The accuracy of the decomposed IMFs may be verified by examining orthogonality among IMFs.

The sifting process uses cubic spline interpolation algorithm to estimate the upper and lower envelopes of the signal. This algorithm is of second-order smoothness (second-order derivable), which fits the local extrema points with inadequate flexibility. Qin and Zhong [94] reported that fitting the local extrema points using

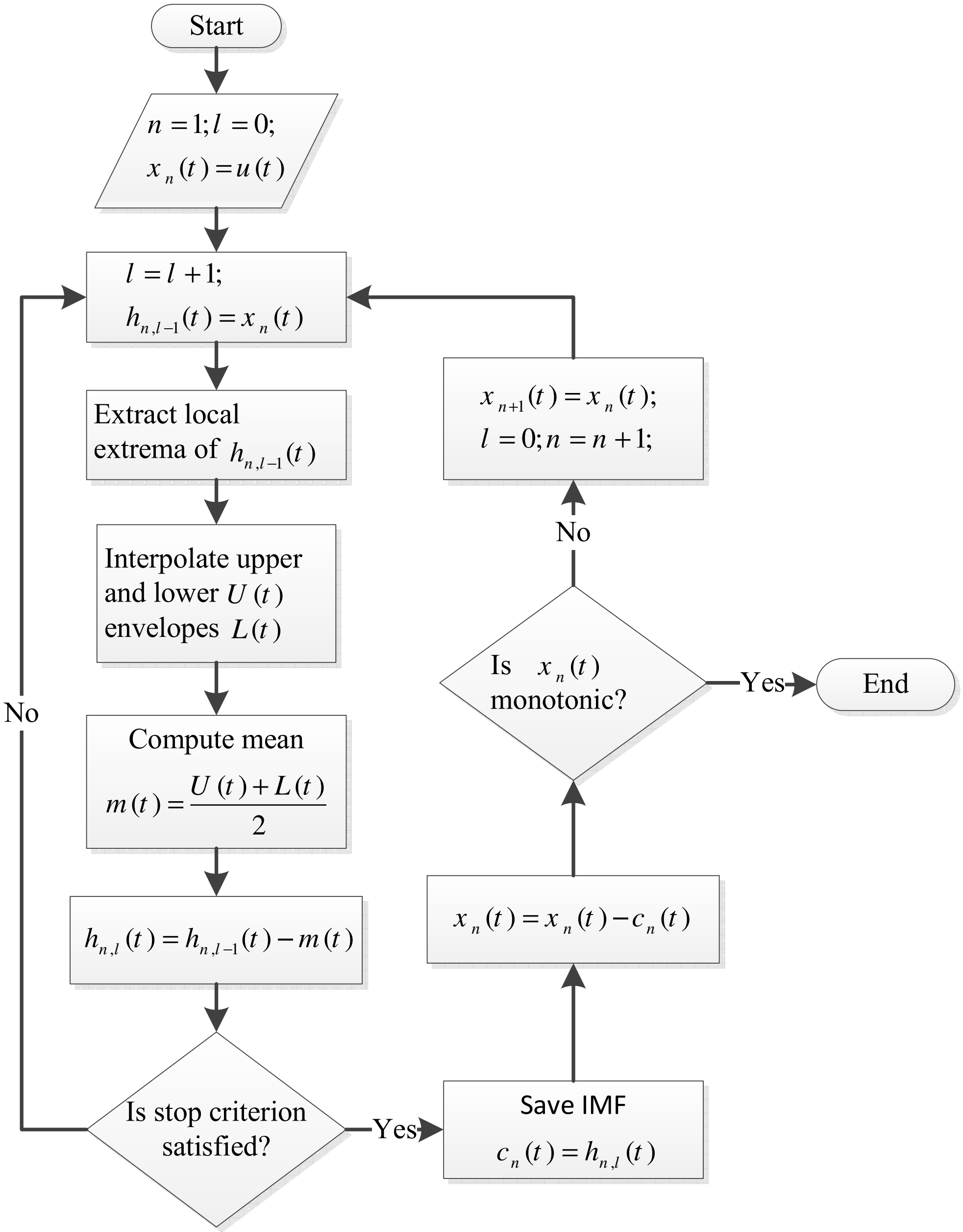

Figure 2.9: The sifting process flowchart

cubic spline interpolation algorithm leads to over- and undershoot problems. These problems shift the instantaneous mean of the upper and lower envelopes $m(t)$ in the sifting process and may not satisfy the conditions required by EMD algorithm.

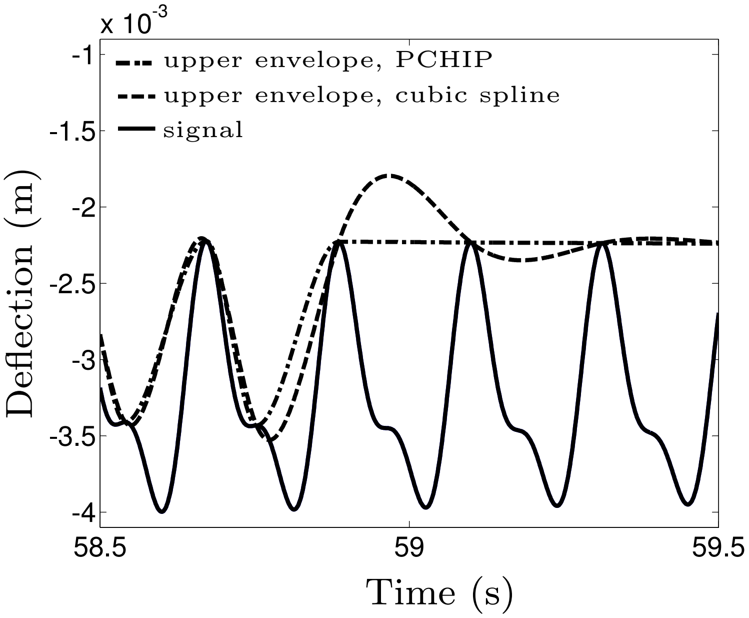

Figure 2.10: Comparison of the upper envelopes in the sifting process based on cubic spline and PCHIP for vertical transient response of a cracked Jeffcott rotor at shaft speeds close to half of its first critical speed

Shulin et al. [95] proposed a Piecewise Cubic Hermite Interpolating Polynamial (PCHIP) to replace the cubic spline interpolation algorithm in the sifting process to eliminate the over- and undershoot problems. The PCHIP is of first-order smoothness with higher flexibility compared with the cubic spline. It has been shown that the results obtained by employing EMD algorithm based on PCHIP provide more features information that the cubic spline in reciprocating pump valves fault diagnosis.

In this dissertation research, in order to evaluate the effectiveness of the proposed interpolation algorithm in [95], the cubic spline and the PCHIP algorithms have been used to obtain upper envelope of the vertical transient response of a shaft-disc system with material properties and dimensions summarized in Table 3.5. The shaft rotates at speeds near to half of the first critical speed of the system, in which the second harmonic component of the vertical transient response has been excited. Comparing the estimated upper envelopes using the both algorithms, illustrated in Figure 2.10, show that the over- and undershoot problems have been eliminated by using PCHIP.

2.7 Summary

Governing equations of lateral motion of analytical and FE shaft-disc system models were formulated in this chapter. An alternate solution function, namely, modified harmonic balance method was proposed to evaluate the harmonic and super-harmonic components of the lateral response of the analytical shaft-disc model. The boundary and continuity conditions of a continuous shaft containing two cracks and discs mounted with different bearing supports were described. The analytical model using Timoshenko beam theory and corresponding crack and disc continuity conditions may be developed in order to add multiple cracks and discs on the shaft. Localized stiffness coefficients of the cracked shaft were obtained using fracture mechanics concepts and different breathing crack models. An alternate explicit breathing function was also proposed to model the saturation phenomenon in crack opening and closing as well as for reducing the computational costs associated with determination of stress intensity factor at each point on the crack edge. The methods of solutions to compute steady-state and transient lateral responses using modified harmonic balance and Runge-Kutta methods, respectively, were described. Moreover, the Hilbert-Huang transform based on an improved empirical mode decomposition was introduced to obtain the time-frequency representation of transient response.

Chapter 3

Verification of the Modified Harmonic Balance Method and the Alternate Breathing Function

3.1 Introduction

The harmonic balance method has been widely used for estimation of the lateral response of numerical models of the shaft-disc systems [e.g., 6, 55]. This method, yields effective estimation of the harmonic as well as super-harmonic components of the response in a highly efficient manner. The approach, however, has not been attempted to determine harmonic as well as super-harmonic components of lateral responses of analytical shaft-disc models. The response estimation of analytical models have been mostly limited to the fundamental harmonic response [e.g., 38, 40]. The modified harmonic balance method introduced in chapter 2 is used to compute the harmonic and super-harmonic components of the steady-state lateral responses of the analytical shaft-disc model. This approach overcomes the limitations of the FE model associated with high computational costs, and eliminates optimization of the cracked element length.

In this chapter, the results obtained from both models are compared to examine validity of the modified harmonic balance method in obtaining the critical speeds of a shaft-disc system with different cracks depths. Moreover, the critical speeds and mode shapes of an intact shaft-disc system obtained from analytical and FE models are compared. In order to verify the shaft-disc model and crack detection results, performing experimental measurements are also required. Experimental measurements give valuable information to improve the proposed crack detection method. In this study, a laboratory experiment is designed to measure lateral vibrations of the shaft near the disc location at different speeds of the shaft.

Although the proposed breathing model by Darpe et al. [50] can accurately describe the breathing behavior of the crack with different depths, it poses high computational cost model. The alternate breathing function in chapter 2, provides an explicit function to reduce the computational costs. The validity of this function in modeling the breathing behavior of the crack with different depths in obtaining the transient responses of a rotor is also examined through comparisons with results obtained from Darpe et al. [50] breathing model.

3.2 Verification of the modified harmonic balance method

3.2.1 Experimental verification

An experiment was designed to measure the critical speeds of the shaft-disc system with and without a crack. The experiment was performed using a Machinery Fault Simulator (Spectra-Quest, Inc.), shown in Figure 3.1. The experimental set-up consists of a flexible shaft with two discs mounted on flexible-long bearing supports. The experiments, however, were limited only to the first critical speed since the maximum motor speed was limited to 3420 rpm. In this experiment, an unbalance mass was attached to disc 1 to excite the lateral vibrations of the shaft. The transverse crack on the rotating shaft breathes as the static deflection of the shaft is much greater than the dynamic deflection response. Further, a relatively heavy disc (disc 2) was mounted on the shaft away from the supports to achieve greater static deflection to simulate crack breathing behavior and to ensure that the first critical speed of the system occurs within the maximum speed of the AC motor. The material properties and dimensions of the shaft-disc system are summarized in Table 3.1.

The experiments were initially performed to identify the bearing stiffness along the vertical and horizontal directions so as to match the first critical speed of the intact shaft-disc system to that obtained from the analytical model. This provided bearings stiffness (k_{yy}, k_{zz}) of 9.24525×10^5 N/m, while the cross-stiffness due to supports were assumed to be $k_{yz} = k_{zy} = 0$. A pair of proximity probes was mounted

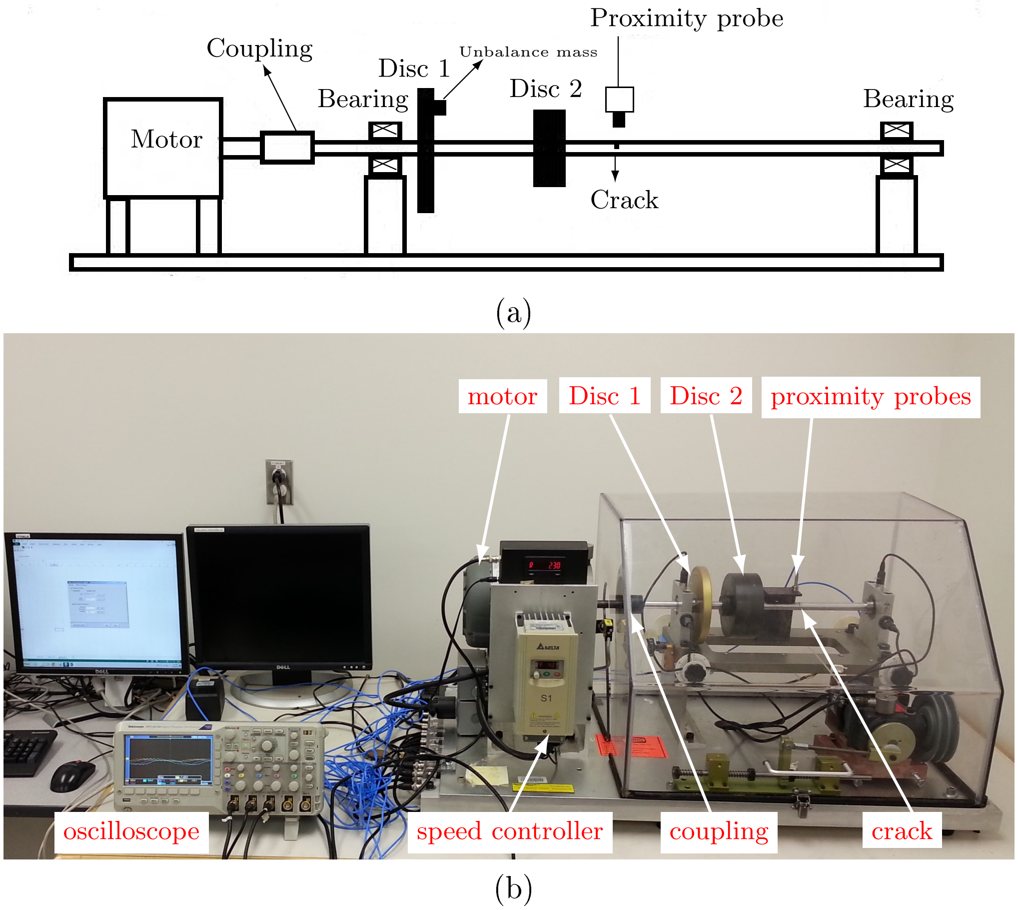

Figure 3.1: (a) The sketch of the experimental set-up and (b) a pictorial view of the Machinery Fault Simulator (Spectra-Quest, Inc.)

on the shaft for measurements of deflection response of the shaft. The first critical speeds of the shaft-disc system were identified as the spin speeds corresponding to the resonant peak in the lateral displacement amplitude response.

A fatigue crack was subsequently introduced on the shaft using cyclic bending loads as per ASTM E399-09 [96]. For this purpose, a 3-point bending fixture was installed on an MTS machine. Considering the actual geometry of a fatigue crack, shown in Figure. 3.2, half of the crack depth could be visualized within the front section, a_v, while the crack was fully-open under the static load, P_y, exerted by the 3-point bending fixture. The crack depth, a, was thus estimated twice the visible depth of the crack on the shaft. Two shafts with normalized crack depth,

Table 3.1: Material properties and dimensions of the experimental set-up

Description	Value
Modulus of elasticity (Pa)	69×10^9
Modulus of rigidity (Pa)	34×10^9
Shaft diameter (m)	0.0159
Shaft length (m)	0.3619
Shaft density (kg/m^3)	2700
Disc 1 density (kg/m^3)	2022
Disc 1 diameter (m)	0.150
Disc 1 thickness (m)	0.015
Normalized Disc 1 location	0.0921
Disc 2 density (kg/m^3)	7600
Disc 2 diameter (m)	0.127
Disc 2 thickness (m)	0.051
Normalized Disc 2 location	0.2894
Unbalance mass (kg)	0.006
Unbalance eccentricity (m)	0.069
Normalized crack location	0.3991

Table 3.2: Comparisons of the measured first critical speed of the system with those obtained from the analytical model

Normalized crack depth	$\Omega_{cr,1}$(Hz)		
	Proposed method	Experiment	Deviation (%)
0	59.52	59.52	0
0.30	59.25	59.40	0.13
0.50	59.13	59.06	0.05

ratio of crack depth to the shaft radius, of 0.3 and 0.5 were realized for subsequent experiments with the cracked shafts.

Table 3.2 compares the measured first critical speeds of the system with intact and cracked shafts with those obtained using the modified harmonic balance method. The model for the cracked shaft employed bearing stiffness identified during the initial experiment involving the intact shaft. The peak deviations between the model and measured results are only 0.05 % and 0.13 % for the crack depths of 0.3 and 0.5, respectively. The comparisons thus suggest that the modified harmonic balance method can yield accurate estimate of the critical speeds of the cracked shaft-disc system.

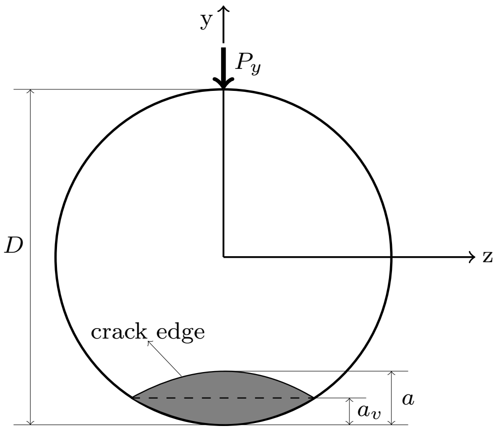

Figure 3.2: Shaft cross-section with a fatigue crack

3.2.2 Verifications using the FE Model

Intact shaft-disc system

In this section, the analytical and numerical models of an intact shaft-disc system are employed to obtain critical speeds and mode shapes of a system applied in [38] (see Table 3.3). The equations of lateral motion of the analytical model using Timoshenko beam theory, described in Eq. (2.3), were solved to obtain steady-state response. Numerical model of the shaft-disc system, formulated using the Finite Element Method (FEM) in section 2.4, is also solved for the same system parameters and bearing supports. The model also considered Timoshenko shaft elements, and the gyroscopic effects.

Table 3.3: Material properties and dimensions of the intact shaft-disc system [38]

Description	Value
Modulus of elasticity (Pa)	200×10^9
Modulus of rigidity (Pa)	77.2×10^9
Shaft diameter (m)	0.01905
Shaft length (m)	1.27
Shaft density (kg/m^3)	7860
Disc density (kg/m^3)	7860
Disc diameter (m)	0.3556
Disc thickness (m)	0.01099
Normalized disc location	0.5

Figures 3.3 and 3.4 show the Campbell diagrams and mode shapes of the system with material properties and dimensions given in Table 3.3, using the analytical and numerical models, respectively. The Campbell diagram illustrates natural frequencies of the rotating shaft-disc system at each shaft speed. The results show that the natural frequencies and mode shapes obtained from the analytical model are almost identical with those obtained from the FE model. Table 3.4 also compares the natural frequencies, and forward and backward critical speeds Ω_{cr} of the analytical and numerical shaft-disc system models developed in this dissertation research. Moreover, selected vibrational properties obtained from an analytical shaft-disc model with the same material properties and dimensions using the Euler-Bernoulli beam theory, reported in [38], are also summarized in this table. The comparisons show that the results obtained from all shaft-disc system models are in good agreements.

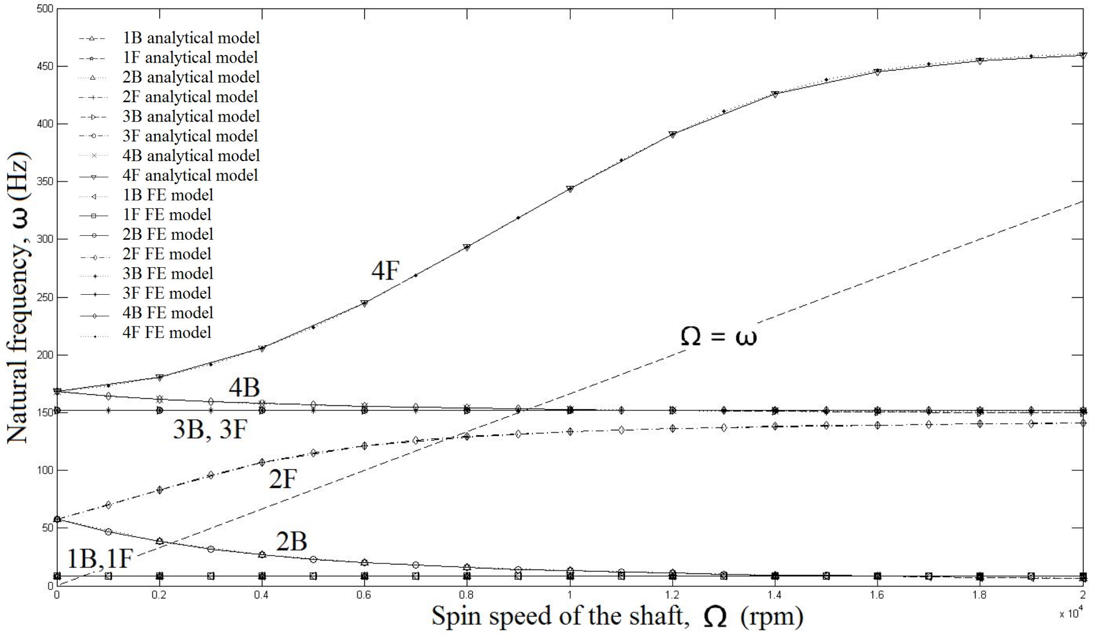

Figure 3.3: Campbell diagrams of the intact shaft-disc system using analytical and FE models, B and F denotes backward and forward whirling speeds of the system, respectively

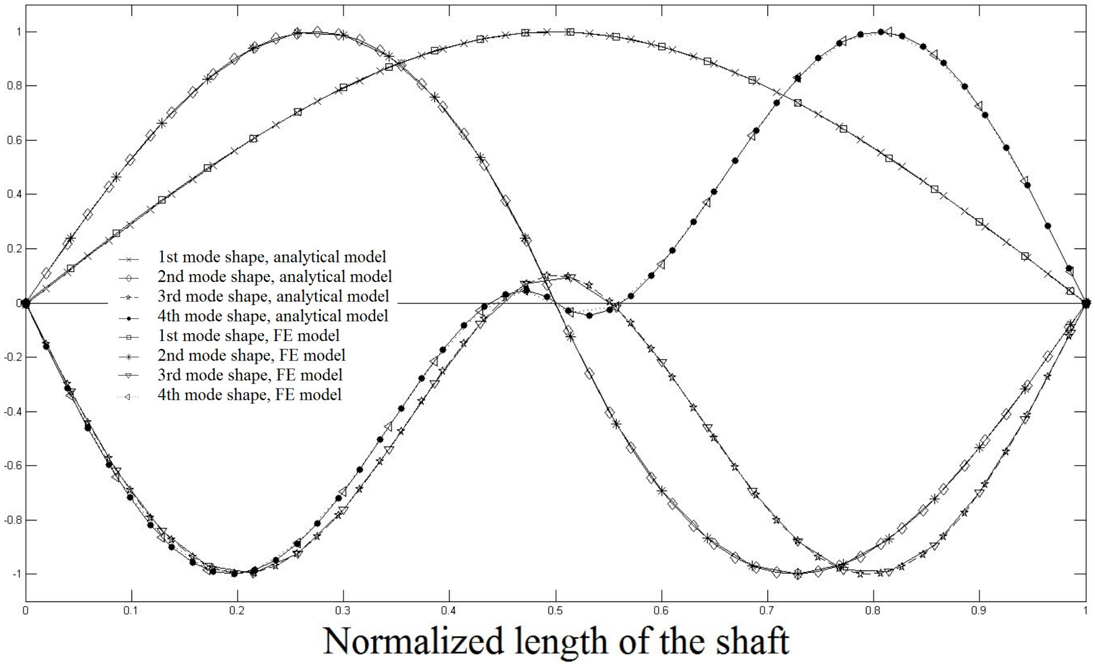

Figure 3.4: Mode shapes of the intact shaft-disc system, $\Omega = 0$

3.2.3 Shaft-disc system with one breathing crack

The modified harmonic balance method is used to determine critical speeds of the analytical model of the shaft-disc system comprising one disc mounted at mid-span of the shaft with a breathing crack and rigid-short bearing supports. Harmonic and super-harmonic components of lateral vibration responses, and the critical speeds of the shaft-disc system are obtained as described in section 2.6. The resulting critical speeds are compared with those obtained from the FE model considering the material properties and dimensions summarized in Table 3.5.

Table 3.6 presents comparisons of the first and third critical speeds, Ω_{cr1} and Ω_{cr3}, of the shaft-disc system obtained from the analytical and the FE models considering different normalized crack depth values. The second mode of the system, however, was not excited since the unbalance mass located on the disc coincided with the node corresponding to second deflection mode. This mode could not be excited and consequently the resonant peak corresponding to the second critical speed does

Table 3.4: The natural frequencies and the critical speeds of the intact shaft-disc system

Present study		Natural frequencies (rpm) with $\Omega = 0$				
		ω_1	ω_2	ω_3	ω_4	ω_5
Analytical		527	3457	9017	10083	28670
FE		527.5	3456.5	9107.4	10082	–
		Critical speeds (rpm)				
		$\Omega_{cr,1}$	$\Omega_{cr,2}$	$\Omega_{cr,3}$	$\Omega_{cr,4}$	$\Omega_{cr,5}$
Analytical	Forward	527	7691	9113	28007	28739
	Backward	527	2221	9102	9185	28377
FE	Forward	527.5	7682.7	9113.6	28007	–
	Backward	527.5	2225	9101.4	9186.5	–
Eshleman and Eubanks [38]		Critical speeds (rpm)				
		$\Omega_{cr,1}$	$\Omega_{cr,2}$	$\Omega_{cr,3}$	$\Omega_{cr,4}$	$\Omega_{cr,5}$
Analytical	Forward	524	7692	9110	–	–
	Backward	–	2203	–	–	

not emerge in the lateral response. The comparisons suggest good agreements in the first and third critical speeds obtained from the two methods. Both the methods yield identical first critical speeds, as expected. The third critical speeds obtained from the two methods are also quite close. The deviation in the third critical speed obtained from the two models is in the order of 0.05 % for the intact shaft and increases gradually with increasing crack depth. The peak deviation corresponds to unity crack depth ratio is only 0.67 %. The results also show that the critical speeds decrease with increasing crack depth. It is evident that the changes in the third critical speed due to a crack depth are greater than those in the first critical speed.

3.2.4 Shaft-disc system with two breathing cracks

The modified harmonic balance method is also used to determine critical speeds of the analytical model of the shaft-disc system with two breathing cracks mounted on rigid-short bearing supports. Table 3.5 summarizes the material properties and dimensions used in the simulations. The cracks breathing behavior is initially modeled using the Mayes and Davies [60] function, while their locations

Table 3.5: Material properties and dimensions of the shaft-disc system

Description	Value
Modulus of elasticity (Pa)	69×10^9
Modulus of rigidity (Pa)	34×10^9
Shaft diameter (m)	0.01905
Shaft length (m)	1.27
Shaft density (kg/m^3)	2700
Disc density (kg/m^3)	2700
Disc diameter (m)	0.1524
Disc thickness (m)	0.0254
Normalized disc location	0.5
Unbalance mass (kg)	0.01
Unbalance eccentricity (m)	0.0508

are taken as $\gamma_1 = \frac{L_0}{L_3} = 0.45$ and $\gamma_2 = \frac{L_2}{L_3} = 0.55$ normalized with respect to the shaft length. The resulting first and third critical speeds of the analytical model are compared with those obtained from the FE model, in Table 3.7 considering different cracks depth values. The cracks depths are normalized with respect to the shaft radius and denoted by μ_1 and μ_2 in the table. It should be noted that the first critical speed obtained from the analytical model with a single crack is used to calibrate crack elements lengths in the FE model, as described in section 2.6.

Since the crack element length also depends on the crack location on the shaft, the identified length could also be used for the second crack, provided they occur on the same location or at mirrored locations of the shaft considering the plane of symmetry of the shaft-disc system. For the purpose of the model verification, mirrored locations of the two cracks are considered, while perpendicular to the shaft at the disc location is taken as the plane of symmetry.

The comparisons in Table 3.7 suggest very good agreements in the first and third critical speeds obtained from the two methods for the ranges of crack depth (μ_1 : 0 to 1; μ_2 : 0 to 0.6) considered. The average deviations in the first and third critical speeds obtained from the two models are in the order of 0.016 % and 0.250 %, respectively, for the entire range of crack depths. It should be noted that the

Table 3.6: Comparison of critical speeds of the shaft-disc system obtained from the modified harmonic balance method and the FE model

Normalized Crack depth	$\Omega_{cr,1}$(rpm)		$\Omega_{cr,3}$(rpm)		
	Proposed method	FE analysis	Proposed method	FE analysis	Deviation (%)
0	747	747	9525.4	9534.3	0.05
0.1	746.9	746.9	9524.1	9533.7	0.05
0.2	746.6	746.6	9518.5	9531.5	0.07
0.3	746	746	9507.6	9527.9	0.11
0.4	745.1	745.1	9490.9	9523.2	0.17
0.5	743.7	743.7	9467.5	9515.2	0.25
0.6	742	742	9436.5	9502.9	0.35
0.7	739.6	739.6	9396.1	9481.8	0.46
0.8	736.6	736.6	9343.6	9448.6	0.56
0.9	732.5	732.5	9275.3	9394	0.64
1	727.1	727.1	9185.4	9308.5	0.67

second deflection mode of the system is not excited since the node coincides with the position of the disc with unbalance. Consequently, the resonant peak corresponding to the second critical speed does not emerge in the lateral response.

3.3 Verification of the alternate breathing function

A shaft supported on rigid-short bearings at both ends with a single disc mounted at the mid-span of the shaft and a breathing crack near the disc is considered for the analysis. The material properties and dimensions of the system model are identical to those given in Table 3.5. It is to be noted that a damping ratio of 0.055 is added to the system in this section. The shaft-disc system is modeled as a Jeffcott rotor and start-up vertical responses for different crack depths are obtained from the governing equations of motion, Eq. (2.1), integrated using fourth order Runge-Kutta method. The shaft starts from rest and reaches the speed of 16.66 Hz (1000 rpm) with a constant acceleration of $\alpha_r = 5\ \frac{\text{rad}}{\text{s}^2}$.

Comparing the vertical transient responses of the system with different crack

Table 3.7: Comparisons of first $\Omega_{cr,1}$ and third $\Omega_{cr,3}$ critical speeds of the shaft-disc system obtained from the modified harmonic balance method and the FE model, ($\gamma_1 = 0.45$ and $\gamma_2 = 0.55$)

Normalized crack depth μ_1	$\mu_2 = 0$		$\mu_2 = 0.2$		$\mu_2 = 0.6$	
	Proposed method	FE analysis	Proposed method	FE analysis	Proposed method	FE analysis
First critical speed, $\Omega_{cr,1}$ (rpm)						
0	747	747	746.7	746.7	742.7	742.7
0.2	746.7	746.7	746.3	746.4	742.4	742.4
0.4	745.3	745.3	745	745	741.1	741.1
0.6	742.7	742.7	742.4	742.4	738.5	738.6
0.8	738.1	738.1	737.8	737.8	734	734.2
1	730	730	729.7	729.7	726.1	726.4
Third critical speed, $\Omega_{cr,3}$ (rpm)						
0	9525.4	9532	9522.6	9530.6	9488.4	9515.6
0.2	9522.6	9530.6	9519.7	9529.5	9485.6	9515.3
0.4	9511	9525.5	9508.2	9524.9	9474.6	9512.5
0.6	9488.4	9515.6	9485.6	9515.3	9452.9	9503.9
0.8	9449.4	9490.4	9446.8	9490.2	9415.5	9479.5
1	9382.7	9466	9380.2	9464.3	9351.3	9428.3

depths passing through first critical speeds using the breathing models proposed by Darpe et al. [50] and the alternate breathing function proposed in this study in Eq. (2.17). The comparisons suggest that the two breathing functions yield comparable responses as the crack depth decreases. The differences in the responses of the two breathing functions are clearly evident for large crack depth. This may be attributed to the fact that the proposed softly-clipped cosine function gives a better estimation of the Darpe et al. [50] breathing model for small crack depths. The similarity of the responses has been computed considering the normalized Euclidean distance between two signals, as [97]:

$$\text{distance } (u_1^t(t), u_2^t(t)) = \frac{1}{1 + ||u_1^t(t) - u_2^t(t)||} \tag{3.1}$$

where $u_i^t(t)$ $(i = 1, 2)$ represents the transient lateral response and $||.||$ returns the norm of the vector. The signals are exactly similar, when the normalized Euclidean distance equals unity, and the similarity between signals decreases as the normalized Euclidean distance between them decreases.

Table 3.8: Transient responses deviations and their computational costs with different normalized crack depths μ using Darpe et al. [50] breathing model and Proposed breathing function

Normalized crack depth μ	Computational cost (s)		Transient responses similarity
	Proposed breathing function	Darpe et al. [50] breathing model	
1	12.866	446.942	0.9296
0.5	12.319	408.907	0.9943
0.2	12.673	369.702	0.9995
0.1	12.364	341.060	0.9999

Table 3.8 summarizes the computational costs and similarities of the obtained transient responses from both breathing models using the average deviation of responses. The computational costs are calculated when the developed program code in MATLAB R2012b platform is run on a pc computer with a 2.8 GHz Intel(R) Core (TM) i5 CPU and 8 GB RAM. The results show that the alternate breathing function reduces the computational cost by nearby 97% compared with Darpe et al. [50] breathing model. It is observed that the computational costs can be substantially reduced using the softly-clipped cosine function without scarifying the accuracy in the presence of small size cracks.

3.4 Summary

The validity of the modified harmonic balance method to obtain the superharmonic components of the steady-state lateral response of the analytical model and consequently the critical speeds was examined using the FE model and the experiments. The critical speeds obtained from harmonic balance method and the experiments were in good agreements. The analytical model is computationally more efficient compared with the FE model, since using the analytical model requires less number of harmonic components in the proposed method to obtain an accurate estimation of the lateral vibrations response. It is noted that the analytical results of the first critical speeds were employed to calculate the proper cracked element length. The transient lateral responses of the rotor with different crack depths were obtained considering the Darpe et al. [50] and alternate breathing functions. The results showed that the alternate breathing function gives good estimate of the crack breathing behavior in the presence of small crack depths, while significantly reducing the computational costs.

Chapter 4

Influence of Cracks' Parameters on the Vibration Responses

4.1 Introduction

Changes in vibrational properties of a shaft-disc system due to the crack have been considered as potential crack indicators. The presence of a crack changes the critical speeds of the system and excites the super-harmonic components of the steady-state as well as transient lateral responses [e.g., 1, 3, 37, 43, 55, 56, 61, 62]. The super-harmonic components exhibit small amplitude sub-critical peaks at fractional critical speeds of the system. The changes in the critical speeds depend on the crack properties such as depth and location, and higher critical speeds are more likely affected by crack depth. Considering changes in higher critical speeds may thus lead to detection of smaller crack depths.

The presence of two cracks in a shaft can effectively change the vibration properties of a shaft-disc system [e.g., 6, 56, 87, 88]. Analyzing the vibration behavior of a shaft with two breathing cracks, however, is much more complex considering cracks properties such as depth, location and relative angular position. Detection of two cracks, however, may be conducted through investigation of changes in the shaft center orbit and super-harmonic components amplitudes of the steady-state lateral response.

Super-harmonic components of the lateral response of a shaft-disc system passing through its critical speed may also be excited due to the presence of a breathing crack. The emergence of these super-harmonic components, however, is not clearly detectable neither in the time response nor the frequency spectrum. The transient lateral response of a rotor is a non-stationary signal, in which the frequency contents change in time. Fourier transform is thus not suitable for analysis of such responses. Using advanced signal processing techniques which are compatible with non-stationary signals may reveal the presence of the breathing crack [e.g., 48, 73, 74, 77].

In the present study, the effects of crack parameters, namely, the depth and location on the selected vibrational properties of a shaft-disc system are obtained. The shaft-disc system is analytically modeled considering a flexible shaft with a rigid disc and boundary conditions due to rigid as well as flexible bearing supports. An unbalance mass is introduced to excite lateral vibration of the system. The steady-state lateral response of the shaft-disc system in the presence of a breathing crack is evaluated using the modified harmonic balance method, described in section 2.5. The changes in the critical speeds and the emergence of sub-critical resonance peaks in the lateral response are evaluated as functions of the crack parameters, and subsequently analyzed as potential crack indicators.

Furthermore, the analytical model of the shaft-disc system is analyzed to obtain its vibrational responses in the presence of two breathing cracks within the flexible shaft. The modified harmonic balance method is utilized to determine responses such as critical speeds, shaft center orbits and the steady-state unbalance lateral response. The alternate softly-clipped cosine function is used to describe breathing behavior of the crack and facilitate implementation of the modified harmonic balance method. The proposed function also resulted in peaks with more accurate amplitudes in frequency spectrum of the lateral response. The effects of crack relative angular positions on the critical speeds and the shaft center orbit are investigated. The frequency spectra of lateral responses of the systems with single and two cracks are compared to those of an intact rotor in order to highlight the changes in responses caused by the cracks.

Finally, start-up responses of a shaft-disc system with different crack depths are considered. The shaft-disc system is analytically modeled as a Jeffcott rotor with a breathing crack to obtain the transient lateral response of the system as it passes through critical speeds. The excitations of super-harmonic components of the transient response and the emergence of sub-critical peaks are considered as crack indicators. The equations of motion are integrated using fourth order Runge-Kutta method. The crack is modeled as a breathing crack using the model proposed by Darpe et al. [50], and the proposed breathing function is also employed to reduce the computational costs. The performances of the proposed crack detection methods for detecting small cracks based on EMD and an improved EMD method are compared.

4.2 Effect of a breathing crack on steady-state lateral vibration responses

The validated analytical model of the shaft-disc system with a single disc mounted on the mid-span is analyzed to study the effects of a breathing crack and bearing supports on the lateral deflection responses. The lateral deflection responses are obtained using the proposed modified harmonic balance method together with the material properties and dimensions of the shaft-disc system presented in Table 3.5. The analyses are performed for the breathing crack located at the mid-span of the shaft, while the normalized depth of the crack is taken as unity. The effect of the breathing crack is evaluated through comparisons of the lateral responses of the shaft-disc system with and without a crack.

Figure 4.1 (a) compares the vertical deflection amplitudes of the intact and cracked systems mounted on rigid-short bearing supports with shaft spin speed increasing from 100 rpm to 10000 rpm with an increment of 0.1 rpm. The results show the emergence of relatively small magnitude sub-critical resonant peaks in the presence of a breathing crack, which are not evident for the intact shaft. These sub-critical resonant peaks are clearly evident at half of the first and third critical speeds suggesting that the second super-harmonic component is well excited. The third super-harmonic component is also excited with relatively small amplitude. The sub-critical resonant peaks are very sharp, and thus increasing the shaft spin speed with a finer increment may result in emergence of sub-critical resonant peaks with relatively smaller amplitudes.

Figures 4.1 (b) and (c) further illustrate the comparisons of responses zoomed in 100 to 1000 and 2800 to 4800 rpm ranges, respectively, in which the shaft spin speed increases with an increment of 0.01 rpm. These clearly illustrate the emergence of sub-critical resonance peaks associated with the first and third critical speeds. It can be realized that the resonant peaks corresponding to half of the critical speeds emerge with a substantially higher amplitudes compared with the peaks at other sub-critical speeds, namely $\frac{1}{3}$ or $\frac{1}{4}$ of the critical speeds. The emergence of sub-critical resonant peaks may thus serve as reliable indicators for detecting the existence of a crack. The emergence of sub-critical resonant peaks in lateral deflection responses of the FE model and the simple Jeffcott model of shaft-disc systems has been reported as a valuable indicator of the existence of the crack [e.g., 3, 37, 61, 62]. The correlations among crack properties and amplitudes of the sub-critical resonant peaks may also be considered for crack parameters identification. For a specified crack depth, the changes in the third critical speed were observed to be considerably greater than those in the first critical speed. The third critical speed is thus more suitable for detection of cracks with small depth. The use of higher critical speeds, for detection of a crack, however, would be limited to situations where the nominal spin speed range of the shaft-disc system is sufficiently high.

The crack properties such as depth and location are known to affect the vibrational properties of the shaft-disc system. While the effect of crack depth on the critical speeds of a shaft-disc system are evident in Table 3.6, solutions were also obtained to study the effect of crack location on changes in the critical speeds. Figure 4.2 shows the changes in the first and third critical speeds of the shaft-disc system as a function of the crack location. The results are presented in terms of the crack location normalized to the shaft length, ($\gamma = \frac{L_0}{L_4}$), while the normalized crack depth is taken as unity ($\mu = \frac{a}{R} = 1$). The results in Figure 4.2 (a) show increase in

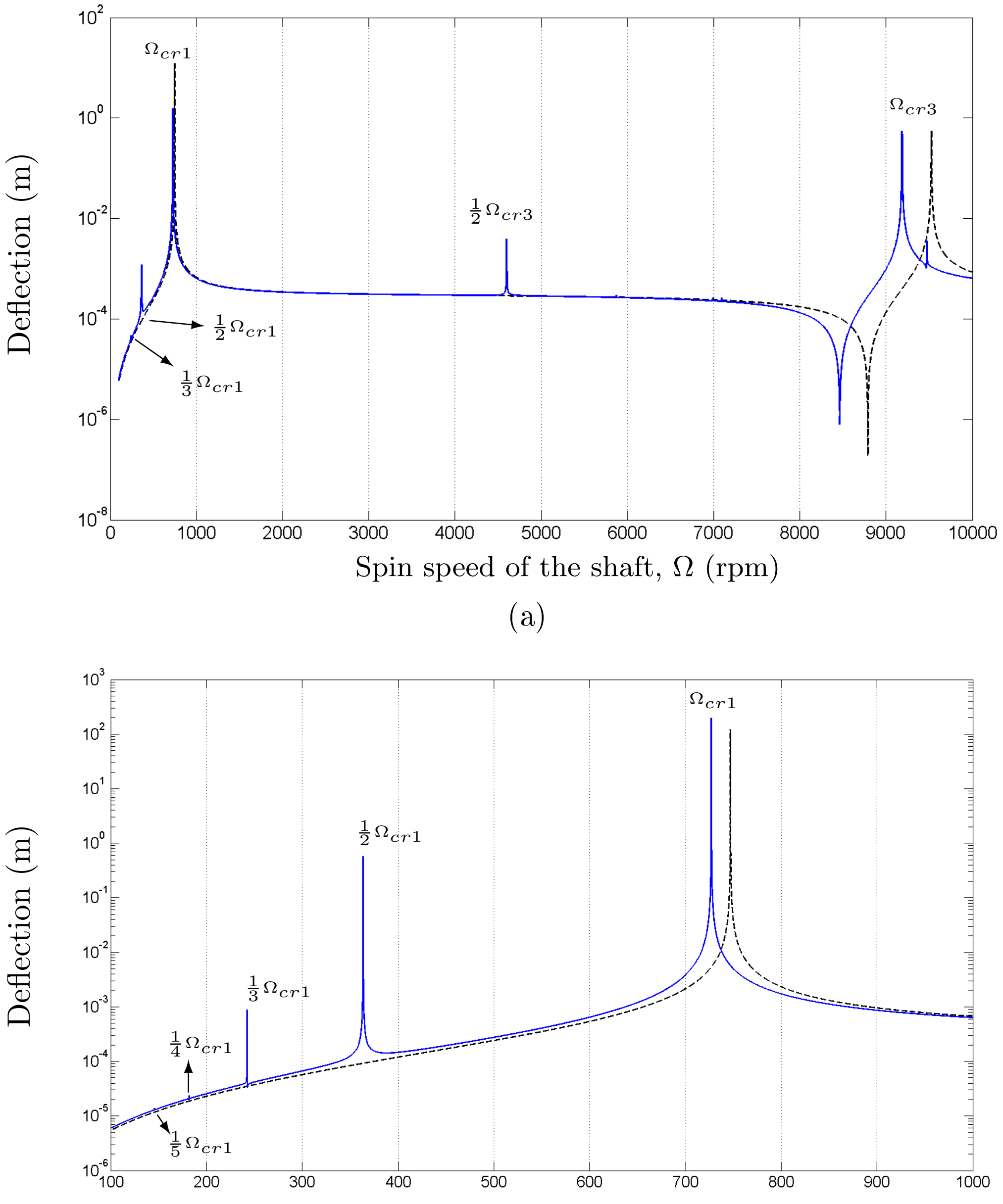

(a)

(b)

Figure 4.1: Vertical deflection amplitude of the shaft-disc system (solid line: normalized crack depth=1, dashed line: no crack)

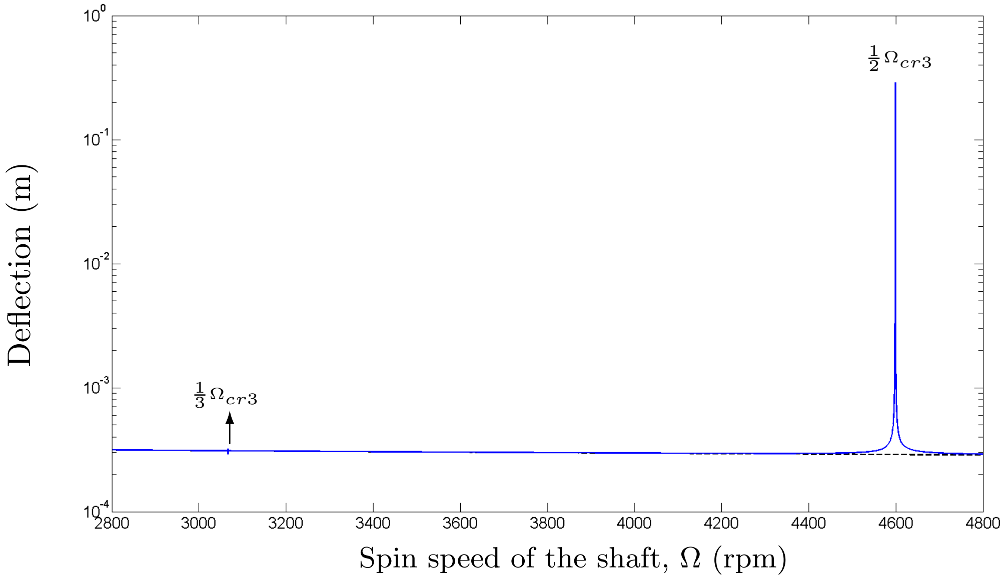

(c)

Figure 4.1 (Continued.): Vertical deflection amplitude of the shaft-disc system

change in the first critical speed from the supports to the middle of the shaft. This is attributed to the shaft deformation corresponding to the first mode. The changes in the third critical speed of the shaft-disc system are also strongly related to the crack location and follow the third mode deflection pattern, as shown in Figure 4.2 (b). The results show that the third critical speed remains unchanged when the crack coincides with the nodes corresponding to third mode shape. Furthermore, the maximum reduction in the third critical speed also occurs when the crack is located at the mid-span of the shaft near the disc. Furthermore, it should be noted that the patterns of the change in the rational fractions ($\frac{1}{2}$ and $\frac{1}{3}$) of the first critical speed are similar to the patterns of change in the third critical speed, respectively.

4.2.1 Effect of bearing support type on crack detection

The changes in the critical speeds due to a crack are also dependent upon the properties of the bearing supports. The proposed modified harmonic balance method is used to investigate the critical speeds of a shaft-disc systems with a single crack for

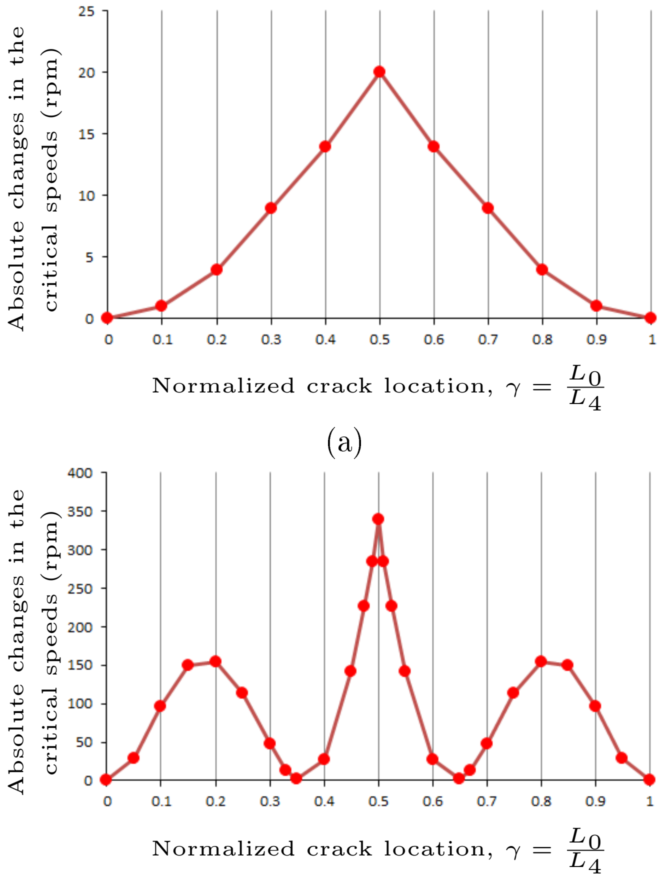

(a)

(b)

Figure 4.2: Changes in the critical speeds of the shaft-disc system (a) first critical speed; (b) third critical speed

four different types of bearing supports, including: rigid-short, rigid-long, flexible-short and flexible-long. The results are obtained for varying depths of crack located at the mid-span of the shaft. The stiffness of flexible-long and flexible-short bearings in vertical and horizontal directions were assumed to be ($k_{yy} = k_{zz} = 9.24525 \times 10^5$ N/m, $k_{yz} = k_{zy} = 0$).

Table 4.1 summarizes the first and third critical speeds of the cracked shaft-disc system for different crack depths and bearing supports. The results show that, as the crack depth increases, the changes in the first and third critical speeds of the shaft-disc system mounted on long bearings are relatively greater than those obtained from the shaft-disc system mounted on short bearings. Assuming that

Table 4.1: Critical speeds of the shaft-disc system with a single crack mounted on different bearing supports

Normalized Crack depth	$\Omega_{cr,1}$ (rpm)				$\Omega_{cr,3}$ (rpm)			
	rigid-short	rigid-long	flexible-short	flexible-long	rigid-short	rigid-long	flexible-short	flexible-long
0	747	1545	743.9	1520.1	9525.4	13489.7	9173.7	12023.8
0.1	746.9	1544.9	743.9	1519.9	9524.1	13487.8	9172.5	12022.4
0.2	746.6	1544.3	743.6	1519.3	9518.5	13479.7	9167.4	12016.5
0.3	746	1543	743	1518.2	9507.6	13464.1	9157.6	12005
0.4	745.1	1541.1	742	1516.4	9490.9	13439.9	9142.4	11987.2
0.5	743.7	1538.5	740.7	1513.3	9467.5	13406.2	9121.2	11962.2
0.6	742	1535	739	1510.5	9436.5	13361.4	9093	11928.6
0.7	739.6	1530.4	736.6	1506.1	9396.1	13302.4	9056.2	11884.1
0.8	736.6	1524.4	733.6	1500.4	9343.6	13226.3	9008.3	11825.8
0.9	732.5	1516.5	729.6	1492.9	9275.3	13126.6	8945.9	11748.6
1	727.1	1506	724.3	1482.9	9185.4	12995.1	8863.6	11645.5

the minimum measurable change in the critical speed is 5 rpm, then the smallest detectable normalized crack depths for the shaft-disc system with rigid-long and flexible-long bearings are 0.5 and 0.2 using the changes in the first and third critical speeds, respectively. Considering the changes in the first critical speeds of the shaft-disc system with rigid-short and flexible-short bearing supports, the smallest detectable normalized crack depths are 0.6 and 0.7, respectively, while the results show that using the changes in the third critical speeds yields the smallest detectable normalized crack depth of 0.2 for the shaft-disc system with different supports.

4.3 Vibration response characteristics of a shaft-disc system with two breathing cracks

The vibration response characteristics of the shaft-disc system are evaluated using the modified harmonic balance method considering two cracks within the shaft. The effects of crack parameters such as depth, location and relative angular position, $\beta = |\Phi_2 - \Phi_1|$, are investigated in view of different responses, namely the critical speeds, shaft center orbit and lateral vibration of the shaft-disc system.

Table 4.2 illustrates the effect of relative axial positions of the two cracks (γ_1 and γ_2) with unity normalized depths ($\mu_1 = \mu_2 = 1$) on the first and third critical speeds. The table also compares the critical speeds of the analytical model incorporating the proposed softly-clipped cosine breathing function and cosine function of Mayes and Davies [60], described in section 2.3.1. The results are obtained considering fixed location of the first crack ($\gamma_1 = \mathrm{L}_0/\mathrm{L}_4 = 0.5$), while varying position of the second crack from the right bearing support ($\gamma_2 = \mathrm{L}_3/\mathrm{L}_4 = 1$) to a location close to mid-span of the shaft ($\gamma_2 = \mathrm{L}_3/\mathrm{L}_4 = 0.6$). The relative position, $|\gamma_2 - \gamma_1| = 0.5$ in Table 4.2 implies that the second crack is located on right bearing and has no effect on the critical speeds.

The results show that both the breathing functions yield comparable critical speeds of the system with cracks. Using the proposed breathing function, however, leads to only slightly higher critical speeds compared to those obtained with Mayes and Davies breathing function. The average deviations between first and third critical speeds obtained from both breathing functions are about 0.009% and 0.016%, respectively. This is likely due to saturation in closing and opening of the crack in the proposed breathing function. The first critical speed of the system with two cracks tends to be lower compared with that with one crack, as the spacing between the two cracks, $|\gamma_2 - \gamma_1|$, decreases. This trend, however, is not consistently observed for changes in the third critical speed. The third critical speed tends to be lower when

Table 4.2: First and third critical speeds of the shaft-disc system with two cracks ($\mu_1 = \mu_2 = 1$ and $\gamma_1 = 0.5$)

γ_2	$\|\gamma_2 - \gamma_1\|$	$\Omega_{cr,1}$(rpm)			$\Omega_{cr,3}$(rpm)		
		Breathing function		Deviation (%)	Breathing function		Deviation (%)
		cosine [60]	clipped cosine		cosine [60]	clipped cosine	
1	0.5	727.1	727.2	0.007	9185.4	9187.8	0.013
0.9	0.4	726.1	726.2	0.007	9102.4	9105.9	0.019
0.8	0.3	723.4	723.5	0.007	9043.2	9047.2	0.022
0.7	0.2	719.3	719.5	0.014	9131.4	9133.7	0.012
0.6	0.1	714.4	714.6	0.014	9171.5	9174.4	0.016

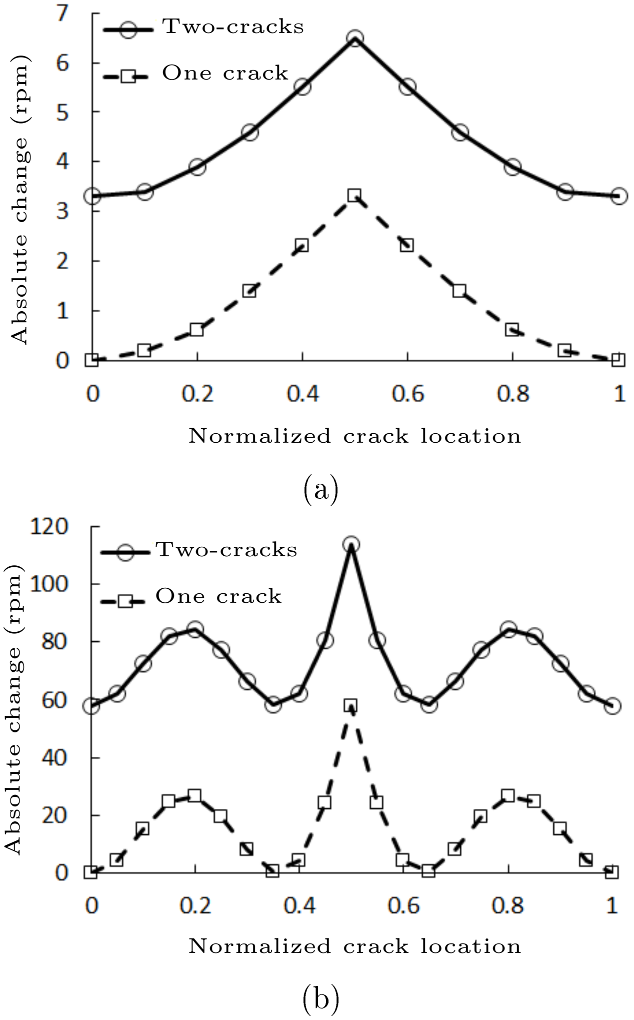

Figure 4.3: Changes in critical speeds of the shaft-disc system with one crack ($\mu_1 = 0.5;\ 0 \leqslant \gamma_1 \leqslant 1$) and two cracks ($\mu_1 = \mu_2 = 0.5;\ \gamma_1 = 0.5;\ 0 \leqslant \gamma_2 \leqslant 1$) versus crack normalized location (a) first critical speed ($\Omega_{cr,1}$); (b) third critical speed ($\Omega_{cr,3}$)

second crack is located close to the extrema points of the corresponding mode at normalized locations of 0.16, 0.5 and 0.83 on the shaft. The change in third critical speed is greatest when the cracks relative position is close to 0.3 ($\gamma_2 = 0.8$).

This is also evident from Figure 4.3, which shows the changes in critical speeds with reference to those of the intact shaft (shaft without crack) as a function of normalized crack locations. The results in the figure are obtained using cosine breathing function [60] with normalized crack depth ($\mu_1 = \mu_2 = 0.5$) and the 0 relative angular position β ($\beta = |\Phi_2 - \Phi_1| = 0$). The Figures 4.3 (a) and (b) also illustrate changes in first and third critical speeds of the system with one crack, respectively, due to the changes in normalized crack location. Results show greatest change in critical speeds when the single crack is located at the mid-span of the shaft.

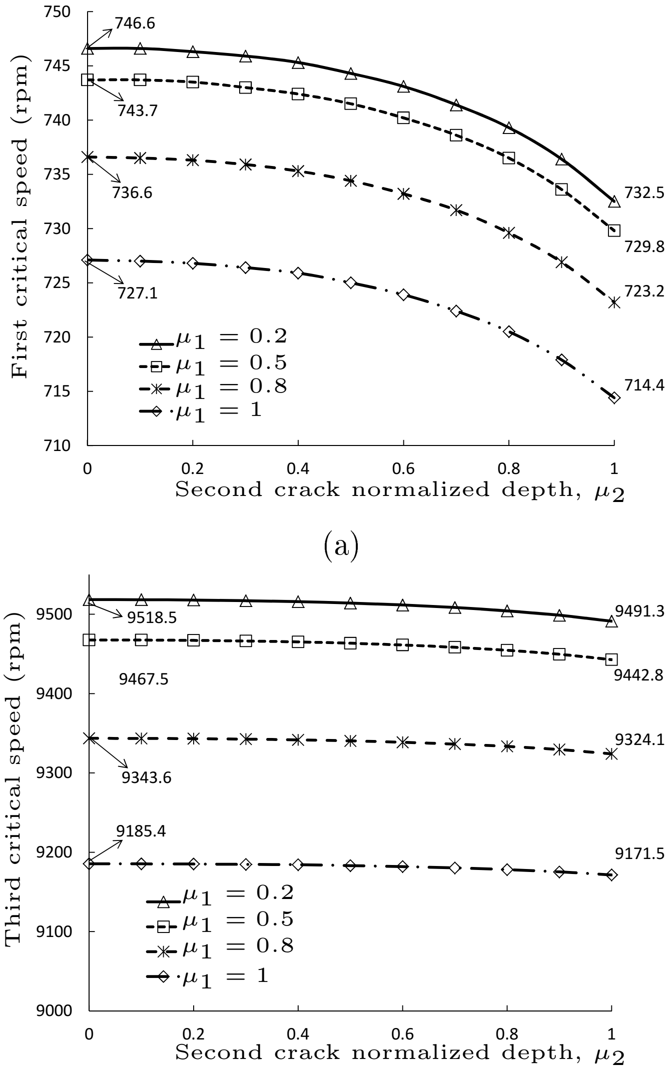

(a)

(b)

Figure 4.4: Effects of cracks depths on critical speeds of the shaft-disc system ($\gamma_1 = 0.4$ and $\gamma_2 = 0.5$); (a) first critical speed ($\Omega_{cr,1}$); (b) third critical speed ($\Omega_{cr,3}$)

Figure 4.4 shows the effect of the cracks depths on the first and third critical speeds for crack normalized locations of ($\gamma_1 = 0.4$ and $\gamma_2 = 0.5$) and 0 relative angular position β. The critical speeds tend to decrease with increasing depth of the first crack μ_1, which is especially evident for the first critical speed. The results further show notable reduction in shaft critical speeds with increasing depth of second crack, irrespective of the first crack depth. The maximum changes in critical speeds occur when normalized depths of both cracks are taken as unity.

Furthermore, higher changes are observed in the critical speeds of the system with one small crack compared with one deep crack, as the second crack depth increases. For example, as shown in Figure 4.4 (b), third critical speeds for the system with two cracks in the presence of first crack normalized depth of 0.2 and 1 change from 9518.5 to 9491.3 rpm and from 9185.4 to 9171.5 rpm, respectively, as the second crack normalized depth increases from 0 to unity. The total reductions in the third critical speeds in these two cases are 27.2 and 13.9 rpm, respectively. In other words, the effect of the first crack on critical speeds is less sensitive to the presence of the second crack, as its depth increases.

Breathing crack excites the super-harmonic components of the lateral vibration, which lead to shaft center orbits with inner loops at fractional critical speeds. Figures 4.5 and 4.6 show the effect of relative angular positions ($\beta = |\Phi_2 - \Phi_1|$) of the breathing cracks, modeled with cosine function [60]. The crack normalized depth are taken as ($\mu_1 = \mu_2 = 1$) at normalized locations of ($\gamma_1 = 0.4$ and $\gamma_2 = 0.5$). As illustrated in these figures, shaft center orbits consist of 2 and 3 inner loops at shaft spin speeds close to $\frac{1}{2}$ and $\frac{1}{3}$ of the first critical speed corresponding to β, respectively. Positions of crossing points of the inner loops, point O in Figure 4.5 and points O_1 and O_2 in Figure 4.6, show that shaft center orbits rotate clockwise, as the relative angular position increases in the clockwise direction.

Furthermore, Figure 4.7 shows the effect of the relative angular position β on the critical speeds of shaft with two cracks using the cosine breathing function. As β changes from 0 to π, the first and third critical speeds decrease, which can be attributed to the fact that the shaft stiffness reduction due to the cracks is

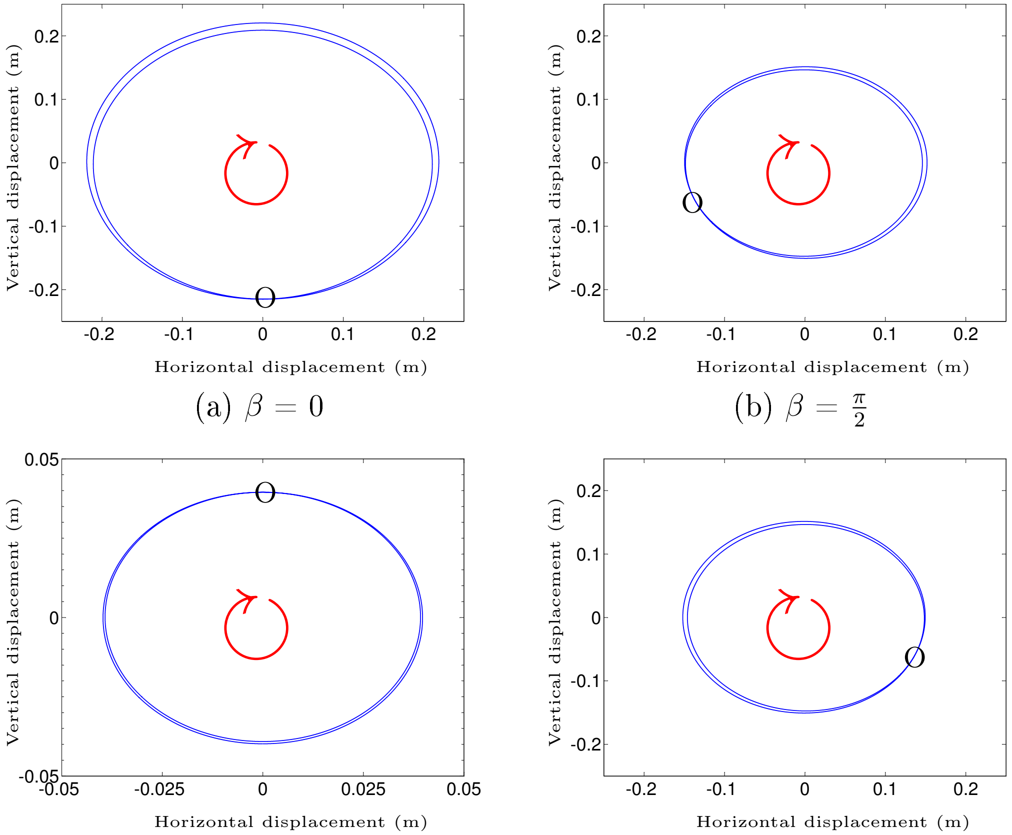

(a) $\beta = 0$ (b) $\beta = \frac{\pi}{2}$

(c) $\beta = \pi$ (d) $\beta = \frac{3\pi}{2}$

Figure 4.5: Shaft orbit centers of the two-crack shaft-disc system close to half of the first critical speed $(\frac{1}{2}\Omega_{cr,1})$ corresponding to β , $(\mu_1 = \mu_2 = 1;\ \gamma_1 = 0.4,\ \gamma_2 = 0.5)$

maximized. Unbalance force F_u, which depends on the shaft speed Ω $(F_u = m_u r_u \Omega^2)$, also decreases. Unbalance force declines at a higher rate than the shaft stiffness, which leads to decrease in the lateral displacement response amplitudes. It is clearly observed in Figures 4.5 and 4.6 that the lateral displacement amplitude decreases, as the relative angular position β increases from 0 to π.

It is to be noted that modeling the cracks breathing behavior using the proposed softly-clipped cosine function leads to similar shaft center orbits close to subcritical speeds of the system corresponding to β with smaller lateral displacement amplitude. This is likely attributed to the fact that the crack is considered to be saturated to either fully-open or fully-closed state in each shaft rotation.

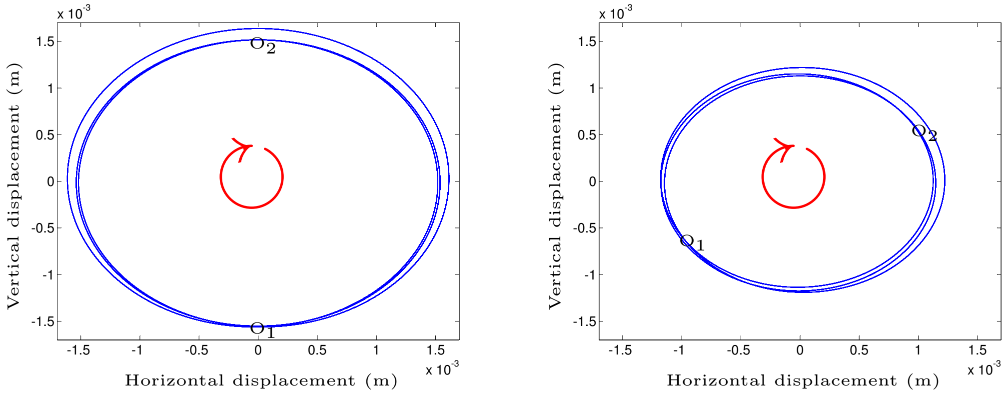

(a) $\beta = 0$ (b) $\beta = \frac{\pi}{2}$

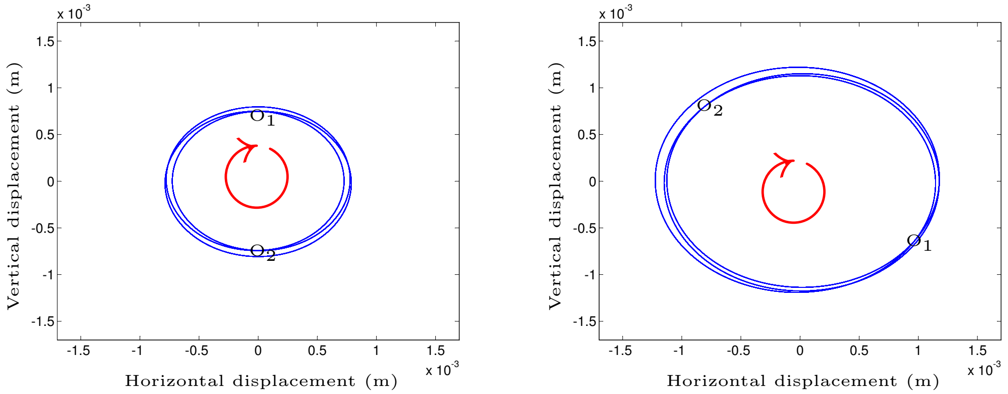

(c) $\beta = \pi$ (d) $\beta = \frac{3\pi}{2}$

Figure 4.6: Shaft orbit center close to half of the third critical speed ($\frac{1}{3}\Omega_{cr,1}$) of a two-crack shaft-disc system corresponding to β, ($\mu_1 = \mu_2 = 1;\ \gamma_1 = 0.4,\ \gamma_2 = 0.5$)

Figures 4.8 and 4.9 compare frequency spectra of vertical responses of the single crack with two-crack shaft-disc systems utilizing cosine [60] and the proposed softly-clipped cosine breathing functions, respectively. It is noted that vertical responses of the two-crack system are obtained at shaft spin speeds close to $\frac{1}{3}$ of first critical speed corresponding to β. As evident from the Figures 4.8 (a and b) and 4.9 (a and b), the presence of the two aligned cracks can effectively increase the third super-harmonic amplitude compared to that of the single crack system. The amplitudes of the second and fourth super-harmonics are also increased but not to the extent of the third super-harmonic component. This is likely due to the shaft spin speed value, which is close to $\frac{1}{3}$ of first critical speed, in which the third super-harmonic

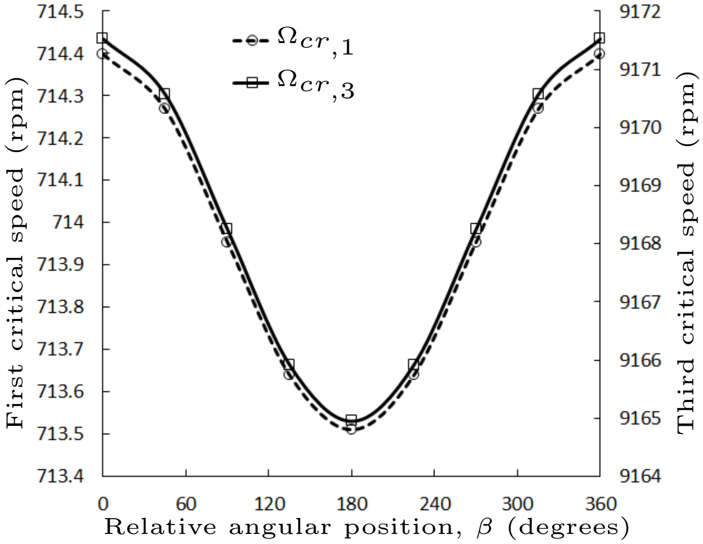

Figure 4.7: Changes in first and third critical speeds ($\Omega_{cr,1}$ and $\Omega_{cr,3}$) of the two-crack shaft due to changes in relative angular position ($\mu_1 = \mu_2 = 1$, $\gamma_1 = 0.5$ and $\gamma_2 = 0.4$)

component of vertical response is highly excited and much more sensitive to changes in shaft stiffness in comparison with other super-harmonic components.

However, as the relative angular position β increases to $\beta = \pi$, the amplitudes of the harmonic and super-harmonic components decrease. As illustrated in Figures 4.8 (e and f) and 4.9 (e and f), for $\beta = \frac{3\pi}{4}$ and $\beta = \pi$ the amplitudes of the second and fourth super-harmonic components are considerably lower compared to those of the first harmonic and third super-harmonic components amplitudes. These changes in the frequency spectrum are also observed in Figure 4.9 (d) for $\beta = \frac{\pi}{2}$, when the cracks are modeled using the proposed softly-clipped cosine function. The frequency spectrum of the vertical response of the two-crack system using the cosine breathing function is shown in Figure 4.8 (d). The results suggest that the amplitudes of the second and fourth super-harmonic components are nearly identical to the first harmonic component amplitude.

Furthermore, as described in section 2.3.1, consideration of the breathing crack saturation phenomenon in the proposed breathing function may lead to reductions

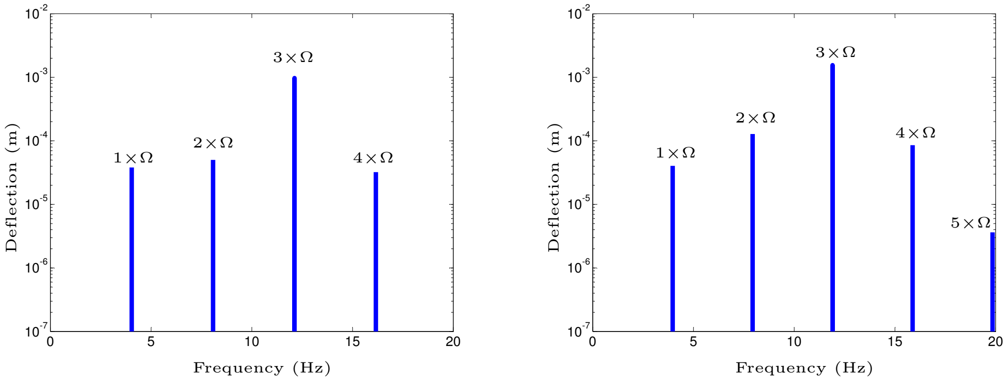

(a) Single crack

(b) β=0

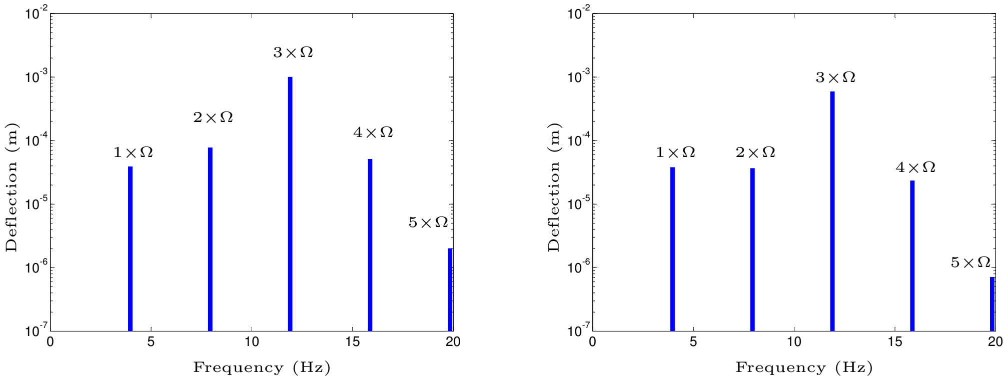

(c) $\beta=\frac{\pi}{4}$

(d) $\beta=\frac{\pi}{2}$

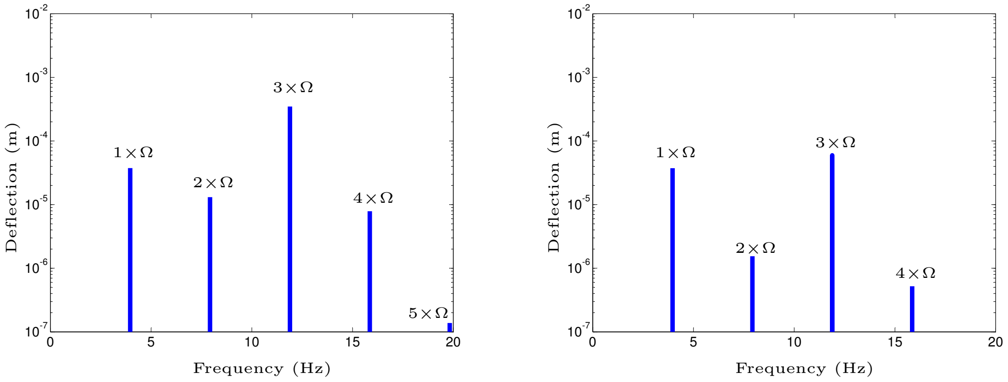

(e) $\beta=\frac{3\pi}{4}$

(f) $\beta=\pi$

Figure 4.8: Frequency spectra of the cracked system vertical responses at the shaft speed close to $\frac{1}{3}\Omega_{cr,1}$ using the Mayes and Davies breathing function, (a) single crack shaft, $\gamma_1 = 0.5$, $\mu_1 = 1$; (b to f) two-crack shaft ($\gamma_1 = 0.5$ and $\gamma_2 = 0.4$, $\mu_1 = \mu_2 = 1$)

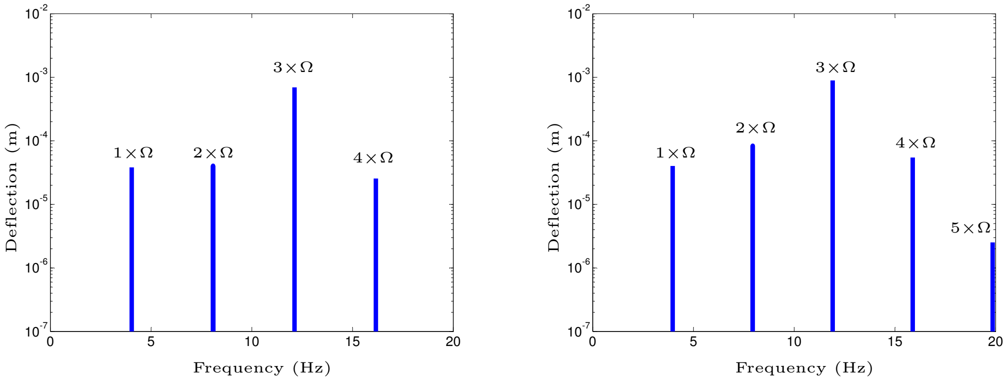

(a) Single crack

(b) β=0

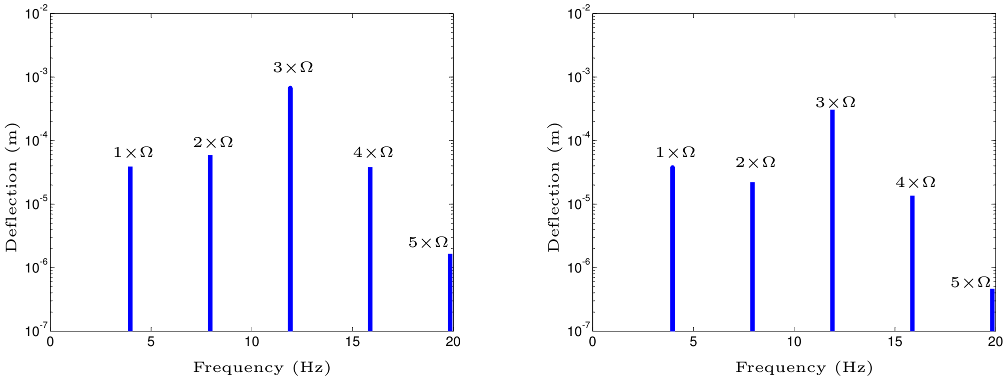

(c) $\beta=\frac{\pi}{4}$

(d) $\beta=\frac{\pi}{2}$

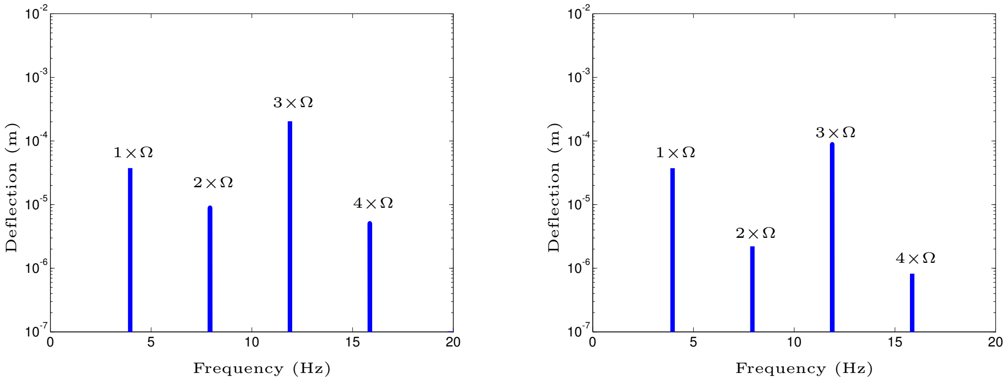

(e) $\beta=\frac{3\pi}{4}$

(f) $\beta=\pi$

Figure 4.9: Frequency spectra of the cracked system vertical responses at the shaft speed close to $\frac{1}{3}\Omega_{cr,1}$ using the proposed breathing function, (a) single crack shaft, $\gamma_1 = 0.5$, $\mu_1 = 1$; (b to f) two-crack shaft ($\gamma_1 = 0.5$ and $\gamma_2 = 0.4$, $\mu_1 = \mu_2 = 1$)

in amplitudes of harmonic and super-harmonic components compared to those obtained from the cosine breathing function. Figure 4.10 compares the harmonic and super-harmonic amplitudes of the vertical responses of the two-crack system versus relative angular position β using cosine and softly-clipped cosine functions. In Figure 4.10 (a), the results show that the first harmonic component amplitudes are almost unaffected by the relative angular position β. Moreover, the two breathing crack models yield nearly identical responses. The maximum deviations in the first harmonic components amplitudes are 6.87% and 6.91% for the cosine and softly-clipped cosine breathing functions as β changes from 0 to π. These deviations are much less than the average deviation (95%) in higher super-harmonic component amplitudes obtained from both the breathing functions, as shown in Figures 4.10 (b,c and d). It can also be concluded that the amplitude of the first harmonic component is independent of the crack parameters and may only depend on the unbalance force. The results in Figures 4.10 (b,c and d) also confirm the expected effect of saturation phenomenon on the decreasing amplitudes of super-harmonic components.

The presence of second and fourth super-harmonic components with lower amplitudes compared with the first harmonic and third super-harmonic components in frequency spectrum can be considered as an indicator of presence of two cracks. Based on this indicator, the two cracks are detectable if the relative angular position is in the ranges of ($\frac{3\pi}{4} \leqslant \beta \leqslant \pi$) and ($\frac{\pi}{2} \leqslant \beta \leqslant \pi$) using the cosine and softly-clipped cosine breathing functions, respectively.

4.4 Breathing crack detection using transient response of a rotor

A shaft supported on rigid-short bearings with a single disc mounted at the mid-span and a breathing crack near the disc is considered for the start-up transient

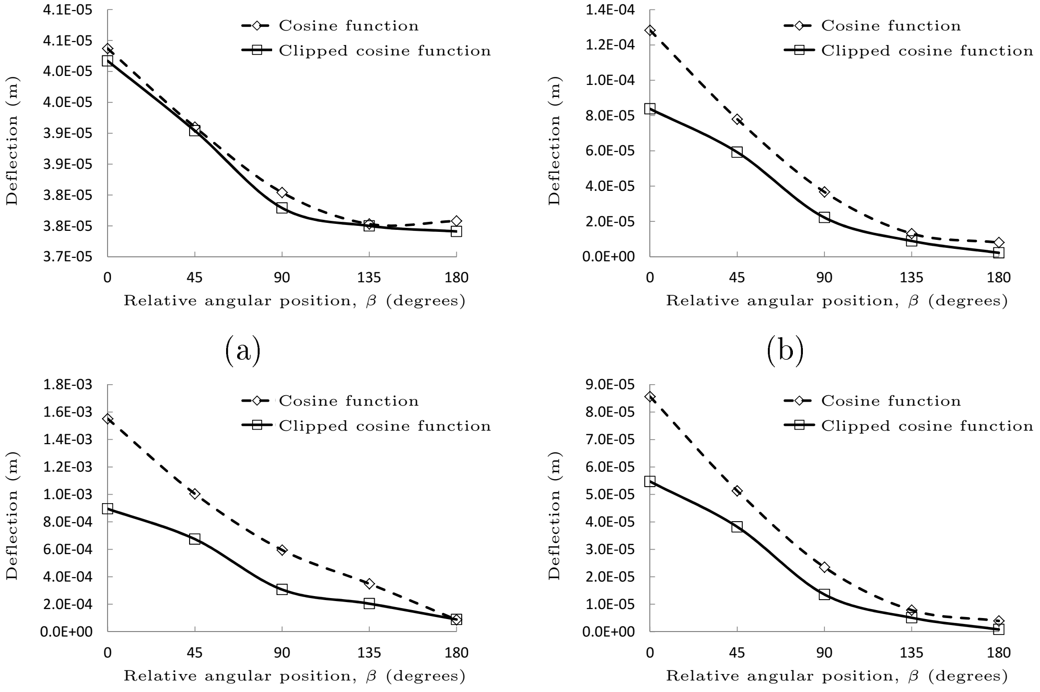

(a) (b)

(c) (d)

Figure 4.10: Amplitudes of harmonic and super-harmonic components of obtained vertical response of the two-crack shaft-disc system at a shaft speed close to $\frac{1}{3}\Omega_{cr,1}$ using the cosine breathing function [60] and softly-clipped cosine function, ($\gamma_1 = 0.5$ and $\gamma_2 = 0.4$, $\mu_1 = \mu_2 = 1$); (a) first harmonic components; (b) second super-harmonic components; (c) third super-harmonic components; and(d) fourth super-harmonic components

response analysis. The material properties and dimensions presented in Table 3.5 are used in the simulations. The shaft-disc system is modeled as a Jeffcott rotor and start-up responses in the vertical direction for different crack depths are obtained from the governing equations of motion, Eq. (2.1). The shaft starts from rest and reaches speed of 16.66 Hz (1000 rpm) with a constant acceleration of $\alpha_r = 5\ \frac{\text{rad}}{\text{s}^2}$.

Figure 4.11 shows the transient response of the intact system in vertical direction and its frequency spectrum and time-frequency representations using HHT based on EMD and improved EMD. These time-frequency representations are considered as the references for finding changes in transient responses of the system due to the crack. The transient response amplitude in Figure 4.11 (a) shows a peak at

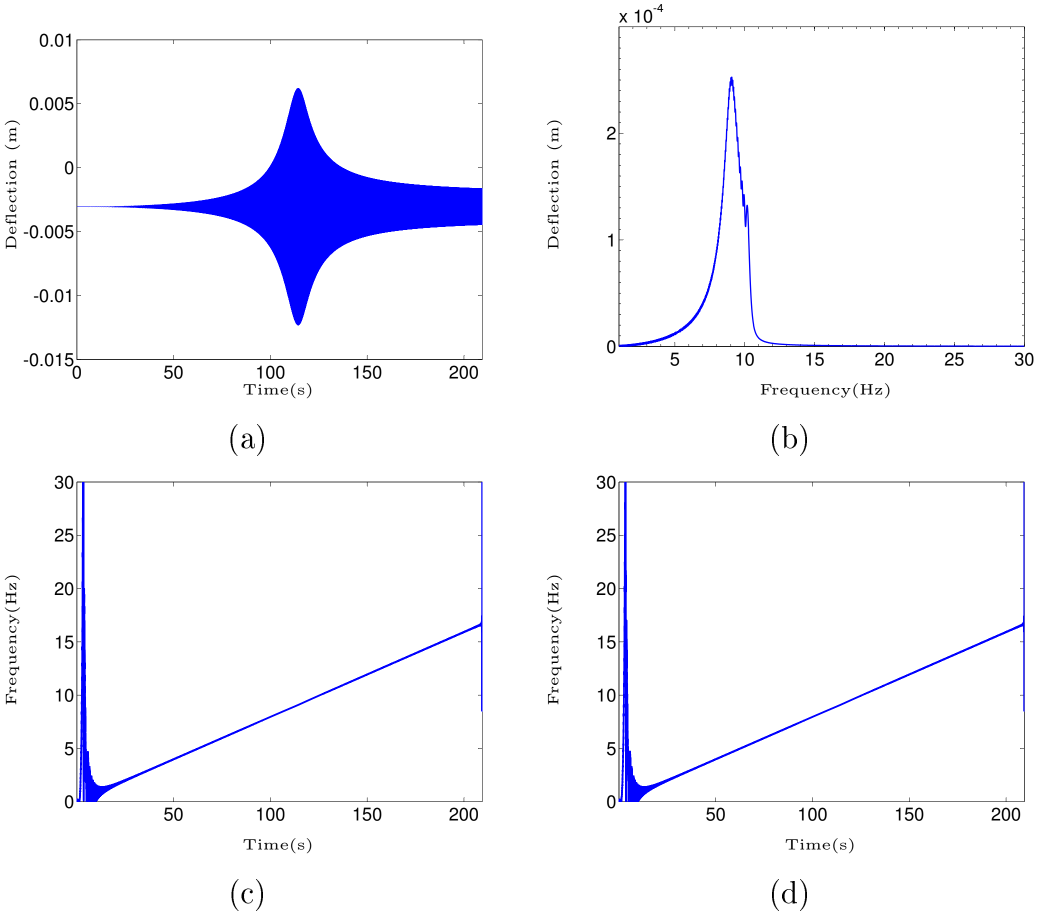

(a) (b)

(c) (d)

Figure 4.11: Transient response of the intact Jeffcott rotor: (a) time response; (b) Fourier spectrum; and time-frequency representations based on (c) EMD; and (d) improved EMD

$t = 114.4$ s, corresponding to shaft speed $\Omega = 9.1$ Hz. This shaft speed is considered as the first critical speed $\Omega_{cr,1}$ of the intact system. The corresponding frequency spectrum in Figure 4.11 (b), also shows the critical speed of the intact system as $\Omega_{cr,1} = 9.07$ Hz, while the corresponding peak amplitude is lower than that shown in the time response. This may be attributed to the fact that Fourier transform is suitable only for stationary signals rather than transient (non-stationary) signals.

Figures 4.11 (c) and (d) illustrate the instantaneous frequency of the vertical transient response obtained from HHT based on EMD and improved EMD methods, respectively. The results show that the instantaneous frequencies, computed based on both the methods, change linearly from 0 to 16.66 Hz (1000 rpm) as expected

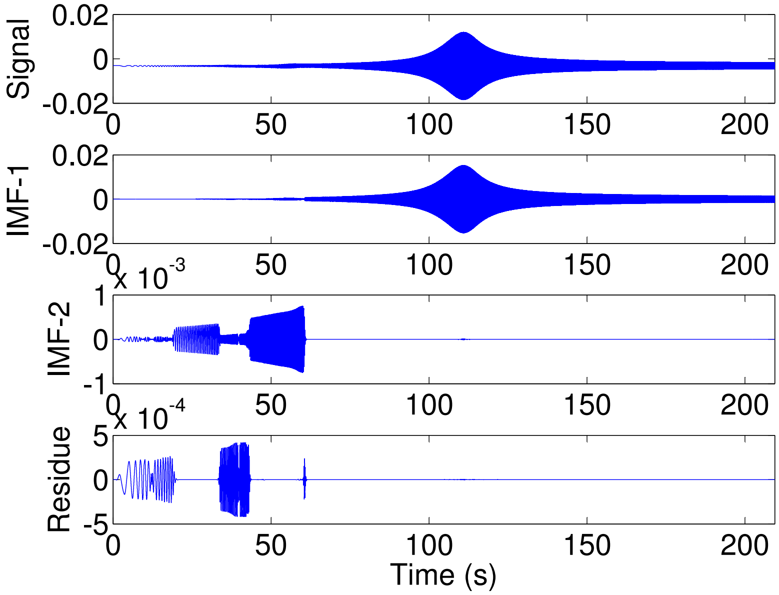

(a)

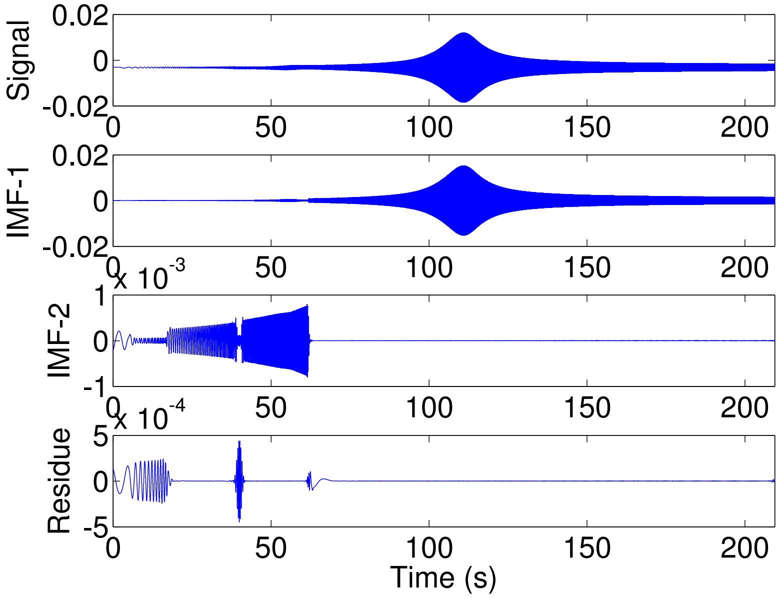

(b)

Figure 4.12: Decomposition of the vertical transient response of the system with a deep crack, ($\mu = 1$), based on (a) improved EMD and; (b) EMD algorithms, the shaft speed changes from 0 to 16.66 Hz (1000 rpm) with a constant acceleration rate of $a_r = 0.5\ \frac{\text{rad}}{\text{s}^2}$

considering the linear relation for shaft speed, Eq. (2.46), in the transient response solution, described in section 2.6. These instantaneous frequencies are computed using Eq. (2.52) and correspond to the first IMF based on EMD and improved EMD methods. It is noted that the unbalance force can only excite the first harmonic component of the transient response of the intact Jeffcott rotor. It must be mentioned that the undesirable high frequencies in the time-frequency representations near the beginning of time $t = 0\ s$, are resulted from numerical errors associated with the algorithms used.

The decompositions of the vertical transient response of the system with a deep crack, ($\mu = 1$), based on EMD and improved EMD algorithms, are shown in Figure 4.12. The vertical transient response has been obtained using Darpe et al. [50] breathing model. The results show that the two algorithms could successfully decompose the transient signal into two IMFs. However, calculating the orthogonality between the obtained IMFs from each algorithm confirms that those obtained from the improved EMD show less dependency compared to those obtained from the EMD. The orthogonality of the IMFs is examined using the dot product between IMFs.

In both EMD and improved EMD algorithms, frequencies in each segment of the non-stationary signal are extracted from higher to lower values. Thus, the first IMF presents the highest frequencies in each signal segment, while other IMFs consists of lower frequencies. For instance, the transient lateral response of the shaft-disc system, shown in Figures 4.12 (a) and (b), the first IMF presents the first harmonic, and second and third super-harmonic components in the vicinities of the first critical speed, $\frac{1}{2}$ and $\frac{1}{3}$ of the first critical speed, respectively. These suggest that the super-harmonic components are also excited in the vicinities of rational fraction of the critical speeds. While the second IMF presents the second and third super-harmonic components in the vicinities of the $\frac{1}{2}$ and $\frac{1}{3}$ of the first critical speed, respectively.

Furthermore, Figures 4.13 (a) and (b) show the time-frequency representations of the vertical transient response of the system with a deep crack ($\mu = 1$). The results clearly show that the presence of the deep crack excites the second, third and forth super-harmonic components ($2\times, 3\times$ and $4\times\Omega$) of the transient response in IMFs obtained from both the algorithms. The first IMFs consist of the highest instantaneous frequencies as seen from the solid curves in these figures. The subsequent IMFs continuously present the relatively lower frequency contents of the time signal, as evident from the figures, and also reported in [76]. For instance, the second IMFs obtained from the transient response represent the first harmonic component ($1\times\Omega$), while the first IMFs represent the second super-harmonic component ($2\times\Omega$) at shaft speeds near $\frac{1}{2}$ of the first critical speed around $t = 50s$, as shown in Figures 4.13 (a) and (b). Figure 4.13 (c) shows the frequency spectrum of the vertical transient response of the system with a deep crack ($\mu = 1$). The comparison between the frequency spectra of the system with a deep crack and the intact system, shown in Figure 4.11 (b), confirms that presence of the crack is not detectable from the frequency spectrum of the transient response.

Deep cracks excite the super-harmonic components of the transient response, which are detectable in time-frequency representations obtained from HHT based on EMD and improved EMD methods. Smaller crack depths, however, cannot effectively excite the super-harmonic components, and yield only low amplitude sub-critical resonant peaks at $\frac{1}{2}$ and $\frac{1}{3}$ of the critical speed in the time-frequency representation of the transient response. Detection of these small amplitude peaks strongly depends on the applied method to obtain the time-frequency representation of the transient response. The improved EMD algorithm used in this study could enhance the performance of the crack detection based on changes in time-frequency representation compared to the EMD algorithm.

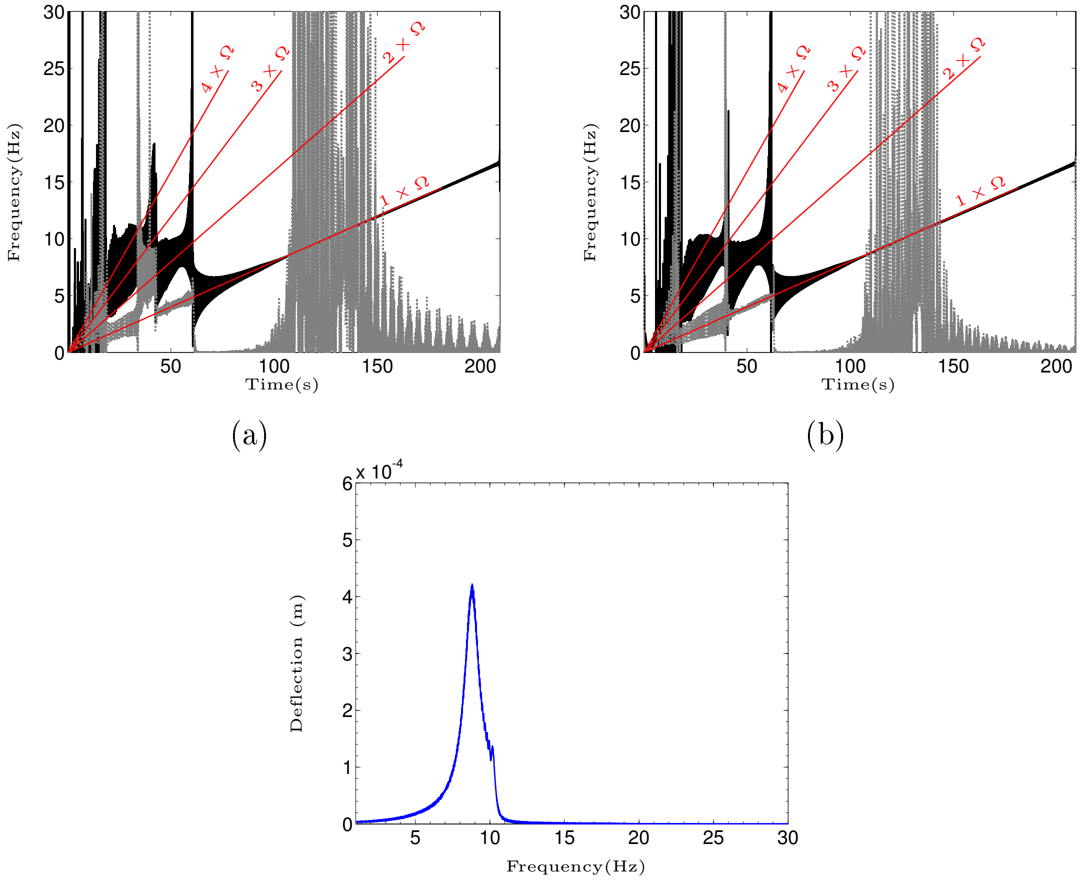

(a) (b)

(c)

Figure 4.13: Time-frequency representations of the vertical transient response of the system with a deep crack, ($\mu = 1$), using HHT based on (a) improved EMD and; (b) EMD algorithms (solid line represents the instantaneous frequency of the first IMF and dotted line represents the instantaneous frequency of the second IMF); and (c) Fourier spectrum

Figure 4.14 shows the time-frequency representations of the vertical transient response of the Jeffcott rotor with a small crack with normalized depth of $\mu = 0.2$, while the crack breathing behavior is modeled using Darpe et al. [50] breathing model. The results show that the effect of sub-critical resonant peaks due to the small crack on the instantaneous frequency of the first IMF are only observable in the time-frequency representation based on improved EMD. The smallest detectable normalized crack depths considering changes in time-frequency representation obtained from HHT based on EMD and improved EMD algorithms are 0.25 and 0.2, respectively. The use of the proposed breathing function, described in Eq. (2.17), also revealed the smallest detectable crack of $\mu = 0.2$, as seen in Figure 4.15. The figure shows changes in the time-frequency representation of transient response of the system near $\frac{1}{2}$ and $\frac{1}{3}$ of the first critical speed, which are obtained from the HHT based on the improved EMD algorithm.

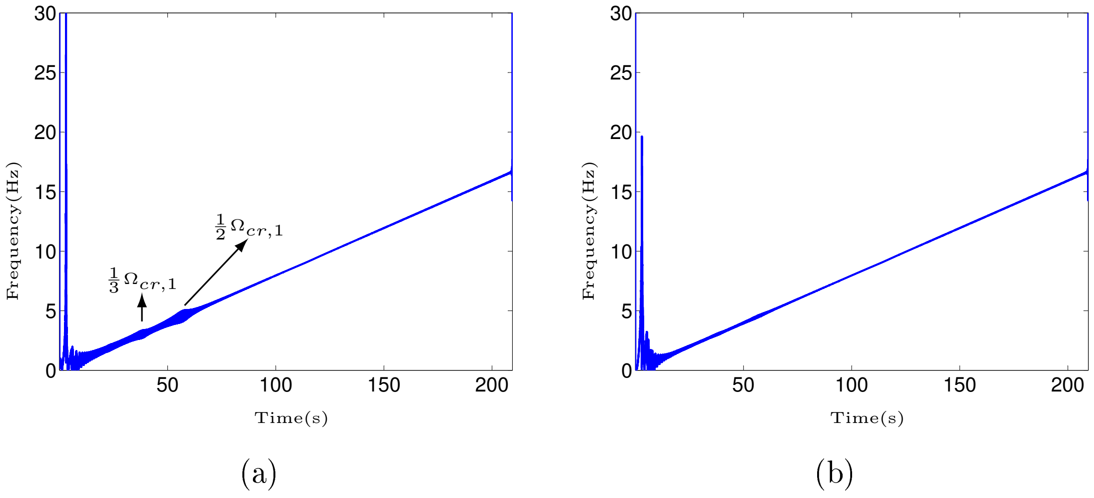

Figure 4.14: Time-frequency representations of the vertical transient response of the system with a small crack, ($\mu = 0.2$), using HHT based on (a) improved EMD; and (b) EMD algorithms

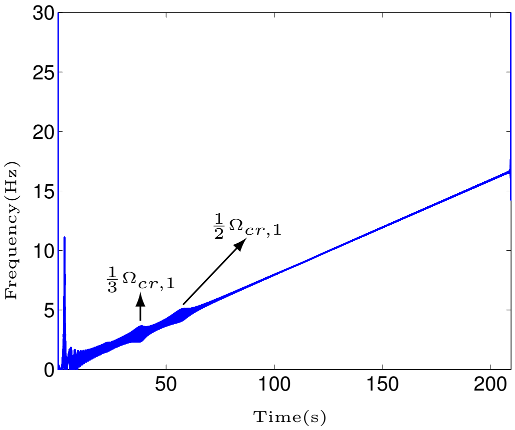

Figure 4.15: Time-frequency representations of the vertical transient response of the system with a small crack, ($\mu = 0.2$), using HHT based on improved EMD, and the crack is modeled using the proposed breathing function in this study

4.5 Summary

In this chapter, a modified harmonic balance method is employed to obtain steady-state lateral responses of a continuous shaft-disc system with a single breathing crack. The smallest detectable normalized crack depth using changes in the third critical speeds is about 0.2 for the shaft-disc system regardless of the type of bearing supports, while the smallest detectable normalized crack depths using the changes in the first critical speeds is 0.5 for the shaft-disc system with long bearing supports. The results show that the emergence of small sub-critical resonant peaks in harmonic and super-harmonic components of the lateral response is an effective indicator of the existence of the crack. The crack location on the shaft also showed an effective impact on changes in the critical speeds. If the crack locates near the supports or a node, the crack is considered to remain closed during entire cycle of rotation and the corresponding critical speed thus remains unchanged. A crack located near points of a mode shape with maximum deflection can effectively reduce the corresponding critical speed.

Furthermore, the results show that the second crack intensifies the effect of the first crack on the critical speeds of the system considering its depth and location on the shaft. The results show that the small depth cracks are more sensitive to the propagation of the second crack compared with relatively deep cracks. The results further showed that modeling the cracks using the softly-clipped cosine breathing function can provide effective detection of two cracks over the relative angular position range of $\frac{\pi}{2} \leqslant \beta \leqslant \pi$, while the cosine breathing function could provide similar detection over a relatively smaller range of angular position ($\frac{3\pi}{4} \leqslant \beta \leqslant \pi$). Both the breathing functions are resulting in similar critical speeds and shaft center orbits of the cracked rotor disc-bearing system.

The Hibert-Huang transform based on an improved empirical mode decomposition is employed to obtain the time-frequency representation of start-up transient response of a shaft-disc system with transverse fatigue crack. The shaft-disc system is modeled as a Jeffcott rotor and the breathing behavior of the crack is modeled using Darpe et al. [50] breathing model. The results show that smallest detectable normalized crack depth using changes in time-frequency representation of vertical transient response based on improved empirical mode decomposition is enhanced by 5% compared with those based on empirical mode decomposition. Furthermore, the proposed explicit breathing function could reduce the computational cost of the applied breathing model without sacrificing the accuracy of the crack breathing model in the case of small crack depths. It is observed that the smallest detectable normalized crack depth using both the breathing functions is 0.2.

Chapter 5

Conclusions and Recommendations

5.1 Major contributions and highlights of the dissertation research

The general aim of this dissertation research is to develop an analytical model and efficient solution strategy to investigate the vibrational response of a rotating shaft-disc system in the presence of multiple breathing cracks. A comprehensive literature review on various vibration-based crack detection methods has been conducted. The results revealed that crack indicators such as changes in the shaft-disc system critical speeds, shaft center orbit evolution and the emergence of sub-critical resonant peaks in super-harmonic components of steady-state and transient lateral responses can be effectively utilized to detect small size cracks. While there are many studies on shaft-disc system with single crack, a few studies have reported the crack detection and vibration analysis of two-crack shaft-disc systems, and also application of advanced signal processing methods in analysis of the transient lateral response of a shaft-disc system. In this dissertation research, analytical model together with an efficient method of solution to obtain vibration characteristics of a rotating shaft-disc system have been developed. A new crack breathing function and advanced signal processing methods have also been proposed to effectively identify the presence of single and two cracks and their characteristics through analysis of the system vibration response. The major contributions of the dissertation research are summarized as follows:

1. Formulating boundary and continuity conditions of an analytical rotating shaft-disc model with two discs and two cracks on arbitrary locations on the shaft mounted on different bearing supports including rigid-short, flexible-short, rigid-long and flexible-long;
2. Developing the modified harmonic balance method to accurately solve the governing equations of motion in order to investigate changes in the selected

vibrational properties such as shaft critical speeds and super-harmonic components in the steady-state response due to single and double cracks;

3. Design an experiment and formulate a FE model to validate the developed analytical model and solution strategy;
4. Investigating the effects of cracks parameters such as depths, locations and relative angular positions on the critical speeds, shaft center orbit and amplitudes of sub-critical resonant peaks;
5. Proposing a softly-clipped cosine function to accurately describe saturation in breathing behavior of the fatigue crack and reducing the computational costs of transient lateral response of a cracked shaft-disc model;
6. Proposing a Hilbert-Huang transform based on the improved empirical mode decomposition to enhance the resolution of the time-frequency representation of the transient lateral for detection of small size cracks;

5.2 Major conclusions

The major conclusions drawn from the dissertation research are itemized as follows:

1. The modified harmonic balance method is utilized to obtain the harmonic and super-harmonic components of the steady-state lateral response. The results from developed analytical model have been verified with those obtained from FE model and experiments. It is observed that the analytical model is computationally more efficient compared with the FE model, as the analytical model requires less number of harmonic components in the proposed solution to obtain an accurate estimation of the lateral vibrations.
2. The crack-induced changes in higher critical speeds are much greater than

those in the first critical speed for a specified crack depth. As the crack depth increases the changes in critical speeds increase, however, the crack location exhibits more pronounced effect on these changes. The effect of the crack location on changes of a critical speed depends on the shaft deflection at crack location of the corresponding mode shape.

3. The smallest detectable normalized crack depth using changes in the third critical speeds, considering a lower threshold of 5 rpm for measurable changes in the critical speeds, is 0.2 for the shaft-disc system regardless of the type of bearing supports, while the smallest detectable normalized crack depths using the changes in the first critical speeds is 0.5 for the shaft-disc system with long bearing supports.
4. Inner loops are emerged in the shaft center orbits at fractional critical speeds due to the presence of the breathing crack, which effectively excites the super-harmonic components of steady-state lateral response. In a two-crack shaft, as the cracks relative angular position β increases clockwise, these shaft center orbits are also rotate clockwise. Moreover, as the relative angular position increases from 0 to π, the critical speed and the shaft center orbit average radius decrease. This may be attributed to the fact that the shaft stiffness decreases with a lower rate than the unbalance force.
5. The results showed that the second crack intensifies the effect of the first crack on the critical speeds of the system considering its depth and location on the shaft. Furthermore, the results show that the small depth cracks are more sensitive to the propagation of the second crack compared with relatively deep cracks as a result of crack saturation.
6. The amplitude of the first harmonic component of the steady-state lateral response only changes with unbalance force and the crack breathing behavior has no effect. In the contrary, amplitudes of the super-harmonic components

are considerably affected by the crack breathing behavior and thus its associated breathing function. The differences between critical speeds and shaft center orbits of the cracked rotor disc-bearing system obtained from the modified harmonic balance method using cosine and softly-clipped cosine breathing functions is found to be negligible.

7. The results showed that modeling the cracks using the alternate (softly-clipped cosine) breathing function providing detection of two cracks for the range of the relative angular position $\frac{\pi}{2} \leqslant \beta \leqslant \pi$ in comparison with the obtained range $\frac{3\pi}{4} \leqslant \beta \leqslant \pi$ using the cosine breathing function.
8. The results showed that smallest detectable normalized crack depth using changes in time-frequency representation of vertical transient response based on improved empirical mode decomposition is 0.2, which has been enhanced by 5% compared with those based on empirical mode decomposition.
9. It is observed that the proposed explicit breathing function could considerably reduce the computational costs of the Darpe et al. [50] breathing model without sacrificing the accuracy of the crack detection method in the case of small crack depths.
10. Changes in selected vibration characteristics obtained from steady-state and transient lateral responses showed almost identical capabilities in detecting small crack depths, however, consideration of each of these responses for crack detection mostly depends on the shaft-disc system working conditions.

5.3 Recommendations for future works

The detection of the crack in the presence of other faults has not been addressed in this dissertation research. This study should thus be continued to investigate the effect of other faults on the efficiency of the proposed crack detection method. Strategies should also be developed to realize if changes in the preselected vibration properties is due to the crack or other faults. This study is also limited to the lateral vibration of the shaft-disc system, while axial and torsional vibrations may show an important role in crack detection and identification. Furthermore, in detection of small cracks using changes in alternate crack indicators, the application of other signal processing techniques may be required. Some recommendations for future studies are thus itemized as follows:

1. The analytical model can be extended to include other faults such as bow shaft and misalignment. The effect of these faults on changes in critical speeds and harmonic and super-harmonic components of steady-state lateral response in the presence of the crack may be studied using the modified harmonic balance method.
2. Jeffcott rotor model as a simplified analytical model with 2 degrees-of-freedom was employed to obtain the transient lateral response. The crack location effect on the efficiency of the crack detection method cannot be investigated using this model. The described analytical model in this study, may also be used to find transient lateral response of the system. This model comprises a continuous shaft, in which the crack can be located in any position on the shaft. It should be noted that the FE model of the shaft-disc system may also be used to eliminate the deficiency of the Jeffcott rotor, although it demands excessive computational cost with low rate of convergence in computing vibration responses.
3. The coupled torsional-lateral vibration is considered to be a crack indicator, which is sensitive only to the crack effects rather than the other faults. This crack indicator was not employed in this study, since an external torque is required to excite crack-induced torsional-lateral coupling. The application of an external torsional torque may not be practical in most rotating systems.

However, the use of this crack indicator for detection of crack in the presence of other faults may be considered in shaft-disc systems, in which the torsional vibrations are already excited.

4. The resolution of the time-frequency representation of the transient vertical response was enhanced using an improved empirical mode decomposition. The application of other decomposition algorithms such as local mean decomposition which are more effective in obtaining instantaneous frequencies may lead to detection of smaller crack depths. Furthermore, the local mean decomposition algorithm is sensitive to the presence of impacts in the signal. The application of this algorithm may effectively reveal crack-induced changes in the lateral response of a shaft-disc system in the presence of a transient torsional excitation.
5. The stability analysis of a shaft-disc system with a breathing crack has been reported in some studies, however, the effects of other faults on the characteristics of the identified instability regions have not been well investigated. The study of the rotating shaft-disc system stability in the presence of multiple faults would be an interesting topic for the future research.
6. In evaluation of the localized shaft stiffness at the location of the crack, various models have considered different crack properties such as depth and location, however, other crack geometries have been neglected. The width of the crack may exhibit a significant effect on estimating the cracked shaft stiffness at each shaft angle. It seems that a wide crack may stay open at each shaft angle, thus, determination of a threshold value for describing the breathing behavior of the crack is necessary.

Bibliography

[1] M.I. Friswell and J.E.T. Penny. Crack modeling for structural health monitoring. *Structural Health Monitoring*, 1(2):139–148, 2002.

[2] A.K. Darpe, K. Gupta, and A. Chawla. Coupled bending, longitudinal and torsional vibrations of a cracked rotor. *Journal of Sound and Vibration*, 269:33–60, 2004.

[3] O.S. Jun, H.J. Eun, Y.Y. Earmme, and C.W. Lee. Modeling and vibration analysis of a simple rotor with a breathing crack. *Journal of Sound and Vibration*, 155(2):273–290, 1992.

[4] A.C. Chasalevris and C.A. Papadopoulos. A continuous model approach for cross-coupled bending vibrations of a rotor-bearing system with a transverse breathing crack. *Mechanism and Machine Theory*, 44:1176–1191, 2009.

[5] C.A. Papadopoulos and A.D. Dimarogonas. Coupled longitudinal and bending vibrations of a rotating shaft with an open crack. *Journal of Sound and Vibration*, 117(1):81–93, 1987.

[6] A.S. Darpe, K. Gupta, and A. Chawala. Dynamics of a two-crack rotor. *Journal of Sound and Vibration*, 259(3):649–675, 2003.

[7] J. Zou, J. Chen, J.C. Niu, and Z.M Cheng. Application of the Wigner–Ville distribution to identification of a cracked rotor. *Proceedings of the Institution of Mechanical Engineers, Part C: Journal of Mechanical Engineering Science*, 217(5):551–556, 2003.

[8] J.T. Sawicki, A.K. Sen, and G. Litak. Multiresolution wavelet analysis of the dynamics of a cracked rotor. *International Journal of Rotating Machinery*, Article ID 65198(DOI: 10.1155/2009/265198), 2009.

[9] N. Bachschmid, P. Pennacchi, E. Tanzi, and A. Vania. Identification of transverse crack position and depth in rotor systems. *Meccanica*, 35(6):563–582, 2000.

[10] P. Ciorau. Contribution to detection and sizing linear defects by phased array ultrasonic techniques. *The e-Journal of Nondestructive*, 10(9):http://www.ndt.net/ article/v10n09/ciorau1 /ciorau1.htm, 2005.

[11] S. Menon, J. N. Schoess, R. Hamza, and D. Busch. Wavelet based acoustic emission detection method with adaptive thresholding. *Proceedings of SPIE*, 3986:71–77, 2000.

[12] F. Pariente and M. Guagliano. X-ray fractography of a diesel engine crankshaft. *Fatigue and Fracture of Engineering Materials and Structures*, 31:111–124, 2007.

[13] R. L. Colwell. *Cracking in a steam turbine rotor disc, Handbook of case histories in failure analysis, Vol 2, K.A. Esakul.* ASM International, 1993.

[14] Y. He, D. Guo, and F. Chu. Using genetic algorithms and finite element methods to detect shaft crack for rotor-bearing system. *Mathematics and Computers in Simulation*, 57:95–108, 2001.

[15] A.S. Sekhar. Multiple cracks effects and identification. *Mechanical Systems and Signal Processing*, 22:845–878, 2008.

[16] B. Li, X.F. Chen, J.X. Ma, and Z.J. He. Detection of crack location and size in structures using wavelet finite element methods. *Journal of Sound and Vibration*, 285:767–782, 2005.

[17] Y. Ishida and Inou T. Detection of a rotor crack using a harmonic excitation and nonlinear vibration analysis. *Journal of Vibration and Acoustics*, 128:741–749, 2006.

[18] C.A. Papadopoulos. The strain energy release approach for modeling cracks in rotors: A state of the art review. *Mechanical Systems and Signal Processing*, 22(4):763–789, 2008.

[19] A.K. Darpe, K. Gupta, and A. Chawla. Experimental investigations of the response of a cracked rotor to periodic axial excitation. *Journal of Sound and Vibration*, 260(2):265–286, 2003.

[20] S. Prabhabkar, A.S. Sekhar, and A.R. Mohanty. Detection and monitoring of cracks in a rotor-bearing system using wavelet transforms. *Mechanical Systems and Signal Processing*, 15(2):447–450, 2001.

[21] A.S. Sekhar. Crack detection and monitoring in a rotor supported on fluid film bearings: start–up vs. run–down. *Mechanical Systems and Signal Processing*, 17(4):897–901, 2003.

[22] N. Bachschmid, P. Pennacchi, and E. Tanzi. Some remarks on breathing mechanism, on non-linear effects and on slant and helicoidal cracks. *Mechanical Systems and Signal Processing*, 22:879–904, 2008.

[23] R. Markert, R. Platz, and M. Seidler. Model based fault identification in rotor systems by least squares fitting. *International Journal of Rotating Machinery*, 7(5):311–321, 2001.

[24] A.S. Sekhar. Model-based identification of two cracks in a rotor system. *Mechanical Systems and Signal Processing*, 18:977–983, 2004.

[25] P. Pennacchi, N. Bachschmid, and A. Vania. A model-based identification method of transverse cracks in rotating shafts suitable for industrial machines. *Mechanical Systems and Signal Processing*, 20:2112–2147, 2006.

[26] Y. Zou, L. Tong, and G.P. Steven. Vibration–based model–dependent damage (delamination) identification and health monitoring for composite structures–a review. *Journal of Sound and Vibration*, 230(2):357–378, 2000.

[27] A.S. Sekhar. Crack identification in a rotor system: a model-based approach. *Journal of Sound and Vibration*, 270(4–5):887–902, 2004.

[28] A.S. Sekhar. Identification of a crack in a rotor system using a model–based wavelet approach. *Structural Health Monitoring*, 2(4):293–308, 2003.

[29] A.S. Sekhar. On-line rotor fault identification by combined model and signal based approach. *Noise and Vibration Worldwide*, 35(7):16–30, 2004.

[30] M. Feldman and S. Seibold. Damage diagnosis of rotors: application of hilbert transform and multihypothesis testing. *Journal of Vibration and Control*, 5(3):421–442, 1999.

[31] I. Bucher and D. J. Ewins. Modal analysis and testing of rotating structures. *Philosophical Transactions of the Royal Society*, 359:61–96, 2001.

[32] I. Imam, S.H. Azzaro, R.J. Bankert, and J. Scheibel. Development of an on–line rotor crack detection and monitoring system. *Journal of Vibration, Acoustics, Stress, and Reliability in Design*, 111:241–250, 1989.

[33] J. Xiang, X. Chen, Q. Mo, and Z. He. Identification of crack in a rotor system based on wavelet finite element method. *Finite Elements in Analysis and Design*, 43:1068–1081, 2007.

[34] H.B. Dong, X.F. Chen, B. Li, K.Y. Qi, and Z.J. He. Rotor crack detection based on high-precision modal parameter identification method and wavelet finite element model. *Mechanical Systems and Signal Processing*, 23:869–883, 2009.

[35] J.J. Sinou. Experimental study on the nonlinear vibrations and n*times* amplitudes of a rotor with a transverse crack. *Journal of Vibration and Acoustics*, 131(4):041008–6, 2009.

[36] G.D. Gounaris and C.A. Papadopoulos. Crack identification in rotating shafts by coupled response measurements. *Engineering Fracture Mechanics*, 69(3):339–352, 2002.

[37] J. Sinou. Detection of cracks in rotor based on the 2× and 3× super-harmonic frequency components and the crack–unbalance interactions. *Communications in Nonlinear Science and Numerical Simulation*, 13:2024–2040, 2008.

[38] R.L. Eshlemen and R.A. Eubanks. On the critical speeds of a continuous shaft-disk system. *Journal of Engineering for Industry*, pages 645–652, 1967.

[39] O.S. Jun and J.O. Kim. Free bending vibration of a multi-step rotor. *Journal of Sound and Vibration*, 224(4):625–642, 1999.

[40] Y. Yamamoto, T.and Ishida. *Linear and Nonlinear Rotordynamics: A Modern Treatment with Applications.* Wiley and Sons, 1st edition, 2001.

[41] A.S. Sekhar and B.S. Prabhu. Transient analysis of a cracked rotor passing through the critical speed. *Journal of Sound and Vibration*, 173(3):415–421, 1994.

[42] J. Sinou and A.W. Lees. A non-linear study of a cracked rotor. *European Journal of Mechanics- A: solids*, 26(1):152–170, 2007.

[43] M.A. AL-Shudeifat and E.A. Butcher. New breathing functions for the transverse breathing crack of the cracked rotor system: Approach for critical and subcritical harmonic analysis. *Journal of Sound and Vibration*, 330:526–544, 2011.

[44] M.A. AL-Shudeifat, E.A. Butcher, and C.R. Stern. General harmonic balance solution of a cracked rotor-bearing-disk system for harmonic and sub-harmonic analysis: Analytical and experimental approach. *International Journal of Engineering Science*, 48:921–935, 2010.

[45] A.S. Sekhar and B.S. Prabhu. Crack detection and vibration characteristics of cracked shafts. *Journal of Sound and Vibration*, 157(2):375–381, 1992.

[46] A.W. Lees and M.I. Friswell. The vibration signature of chordal cracks in asymmetric rotors. *Proceedings of the 19th International Modal Analysis Conference (IMAC), Kissimmee, Florida*, pages 1–6, 2001.

[47] R.H. Plaut, R.H. Andruet, and S. Suherman. Behavior of a cracked rotating shaft during passage through a critical speed. *Journal of Sound and Vibration*, 173:577–589, 1994.

[48] T. Ramesh Babu, S. Srikanth, and A.S. Sekhar. Hilbert–Huang transform for detection and monitoring of crack in a transient rotor. *Mechanical Systems and Signal Processing*, 22(4):905–914, 2008.

[49] O.S. Jun, H.J. Eun, Y.Y. Earmme, and C.W. Lee. Modeling and vibration analysis of a simple rotor with a breathing crack. *Journal of Sound and Vibration*, 155:273–290, 1992.

[50] A.K. Darpe, K. Gupta, and A. Chawla. Transient response and breathing behaviour of a cracked Jeffcott rotor. *Journal of Sound and Vibration*, 272:207–243, 2004.

[51] M.D. Rajab and A. AL-Sabeeh. Vibration characteristics of a cracked shaft. *Journal of Sound and Vibration*, 147(3):465–473, 1991.

[52] L. Cheng, N. Li, X.F. Chen, and Z.J. He. The influence of crack breathing and imbalance orientation angle on the characteristics of the critical speed of a cracked rotor. *Journal of Sound and Vibration*, 330:2031–2048, 2011.

[53] A.S. Sekhar and B.S. Prabhu. Condition monitoring of cracked rotors through transient response. *Mechanism and Machine Theory*, 33(8):1167–1175, 1988.

[54] A.K. Darpe. Coupled vibrations of a rotor with slant crack. *Journal of Sound and Vibration*, 305:172–193, 2007.

[55] J.J. Sinou and A.W. Lees. The influence of cracks in rotating shafts. *Journal of Sound and Vibration*, 285:1015–1073, 2005.

[56] A.S. Sekhar. Vibration characteristics of a cracked rotor with two open cracks. *Journal of Sound and Vibration*, 223(4):497–512, 1999.

[57] A.D. Dimarogonas and C.A. Papadopoulos. Vibration of cracked shafts in bending. *Journal of Sound and Vibration*, 91(4):583–593, 1983.

[58] I.W. Mayes and W.G.R. Davies. Analysis of the response of a multi-rotor-bearing system containing a transverse crack in a rotor. *Journal of vibration, Acoustics, Stress, and Reliability in Design*, 106:139–145, 1984.

[59] N. Bachschmid, P. Pennacchi, and A. Vania. Identification of multiple faults in rotor systems. *Journal of Sound and Vibration*, 254(2):327–366, 2002.

[60] I.W. Mayes and W.G.R. Davies. The vibrational behavior of a rotating shaft system containing a transverse crack. *I. Mech. E. Conference on Vibrations in Rotating Machinery*, C168/76:53–64, 1976.

[61] C.A. Papadopoulos and A.D. Dimarogonas. Stability of cracked rotors in the coupled vibration mode. *Journal of Vibration, Acoustics, Stress, and Reliability in Design*, 110:356–360, 1988.

[62] R. Gasch. A survey of the dynamic behavior of a simple rotating shaft with a transverse crack. *Journal of Sound and Vibration*, 106(2):313–332, 1993.

[63] A.K. Darpe. A novel way to detect transverse surface crack in a rotating shaft. *Journal of Sound and Vibration*, 305(1–2):151–171, 2007.

[64] J.T. Sawicki, X. Wu, G.Y. Baaklini, and A.L. Gyekenyesi. Vibration-based crack diagnosis in rotating shafts during acceleration through resonance. *Nondestructive Evaluation and Health Monitoring of Aerospace Materials and Composites II*, 5046 of Proceedings of SPIE:1–10, 2003.

[65] R. N. Bracewell. *The Fourier Transform and Its Applications.* Boston: McGraw–Hill, 3rd edition, 2000.

[66] O. Rioul and M. Vetterli. Wavelets and signal processing. *IEEE Signal Processing Magazine*, 8(4):14–38, 1991.

[67] E. Wigner. On the quantum correction for thermodynamic equilibrium. *Physical Review Letters*, 40:749–759, 1932.

[68] A. Grossmann and J. Morlte. Decomposition of hardy functions into square integrable wavelets of constant shape. *SIAM Journal on Mathematical Analysis*, 15(4):723–736, 1984.

[69] N.E. Huang, Z. Shen, S.R. Long, M.C. Wu, E.H. Shih, Q. Zheng, N.C. Yen, C.C. Tung, and H.H. Liu. The empirical mode decomposition method and the Hilbert spectrum for non-stationary time series analysis. *Proceedings of The Royal Society of London, A*, 454:903–995, 1998.

[70] R. B. Pachori and P. Sircar. A new technique to reduce cross terms in the Wigner distribution. *Digigtal Signal Processing*, 17:466–474, 2007.

[71] C.K. Chui. *An Intruduction to Wavelets*. Academic Press, Boston, MA, 1992.

[72] A.S. Sekhar. Detection and monitoring of crack in a coast-down rotor supported on fluid film bearings. *Tribology International*, 37(3):279–287, 2004.

[73] A.S. Sekhar. Crack detection through wavelet transform for a run-up rotor. *Journal of Sound and Vibration*, 259(2):461–472, 2003.

[74] S.A. Adewusi and B.O. Al-Bedoor. Wavelet analysis of vibration signals of an overhang rotor with a propagating transverse crack. *Journal of Sound and Vibration*, 246(5):777–793, 2001.

[75] J. Zou, J. Chen, J.C. Niu, and Z.M Cheng. Study on the transient response and wavelet time–frequency feature of a cracked rotor passage through a subcritical speed. *Journal of Strain Analysis for Engineering Design*, 38(3):269–276, 2003.

[76] Y. Lei, J. Lin, Z. He, and M.J. Zuo. A review on empirical mode decomposition in fault diagnosis of rotating machinery. *Mechanical Systems and Signal Processing*, 35:108–126, 2013.

[77] D. Guo and Z.K. Peng. Vibration analysis of a cracked rotor using Hilbert–Huang transform. *Mechanical Systems and Signal Processing*, 21(8):3030–3041, 2007.

[78] N. Harish Chandra and A.S. Sekhar. Fault detection in rotor bearing systems using time frequency techniques. *Mechanical Systems and Signal Processing*, 72–73:105–133, 2016.

[79] G.D. Chen and Z.C. Wang. A signal decomposition theorem with Hilbert transform and its application to narrowband time series with closely spaced frequency components. *Mechanical Systems and Signal Processing*, 28:258–279, 2012.

[80] R.T. Rato, M.D. Ortigueira, and A.G. Batista. On the HHT, its problems, and some solutions. *Mechanical Systems and Signal Processing*, 22:1374–1394, 2008.

[81] Z. He, Y. Shen, and Q. Wang. Boundary extension for Hilbert–Huang transform inspired by gray prediction model. *Signal Process*, 92:685–697, 2012.

[82] J. Xun and S.Z. Yan. A revised Hilbert–Huang transformation based on the neural networks and its application in vibration signal analysis of a deployable structure. *Mechanical Systems and Signal Processing*, 22:1705–1723, 2008.

[83] X. Zhu, J. Hu, and S. Lv. Comprehensive evaluation study on the methods for restraining the end effect in EMD. *Information Technology Journal*, 12(16):3870–3874, 2013.

[84] S.D. Hawley, L.E. Atlas, and H.J. Chizeck. Some properties of an empirical mode type signal decomposition algorithm. *IEEE Signal Processing Letters*, 17:24–27, 2010.

[85] A. Roy and J.F. Doherty. Raised cosine filter–based empirical mode decomposition. *IET Signal Processing*, 5:121–129, 2011.

[86] Z.H. Wu and N.E. Huang. Ensemble empirical mode decomposition: a noise-assisted data analysis method. *Advances in Adaptive Data Analysis*, 1(1):1–41, 2009.

[87] K.M. Saridakis, A.C. Chasalevris, and A.J. Dentsoras. Applying neural networks, genetic algorithms and fuzzy logic for the identification of cracks in shafts by using coupled response measurements. *Computers and Structures*, 86:1318–1338, 2008.

[88] T. Ramesh and A.S. Sekhar. Detection of two cracks in a rotor-bearing system using amplitude deviation curve. *Journal of Sound and Vibration*, 314:547–646, 2008.

[89] A.C. Chasalevris and C.A. Papadopoulos. Identification of multiple cracks in beams under bending. *Mechanical Systems and Signal Processing*, 20:1631–1673, 2006.

[90] V. Jaumouille, J.J. Sinou, and B. Petitjean. An adaptive harmonic balance method for predicting the non linear dynamic responses of mechanical systems–application to bolted structures. *Journal of Sound and Vibration*, 329(19):4048–4067, 2010.

[91] M.A. AL-Shudeifat. On the finite element modeling of the asymmetric cracked rotor. *Journal of Sound and Vibration*, 332(11):2795–2807, 2013.

[92] M.A. AL-Shudeifat. Stability analysis and backward whirl investigation of cracked rotors with time-varying stiffness. *Journal of Sound and Vibration*, 348:365–380, 2015.

[93] Y.X. Wang, Z.J. He, and Y.Y. Zi. A comparative study on the local mean decomposition and empirical mode decomposition and their applications to rotating machinery health diagnosis. *Journal of Vibration and Acoustics*, 132(2):021010, 2010.

[94] S.R. Qin and Y.M. Zhong. A new envelope algorithm of Hilbert–Huang transform. *Mechanical Systems and Signal Processing*, 20:1941–1952, 2006.

[95] L. Shulin, Z. Haifeng, W. Hui, and M. Rui. Application of improved EMD algorithm for the fault diagnosis of reciprocating pump valves with spring failure. *In Proceedings of the 9th International Symposium on ISSPA 2007*, pages 1–4, 2007.

[96] ASTM E399-09. Standard test method for linear-elastic plane strain fracture toughness k_{Ic} of metallic materials. West Coshohocken, PA: American Society for Testing and Materials, 2009.

[97] S. Arlot and A. Celisse. A survey of cross–validation procedures for model selection. *Statistics Surveys*, 4:40–79, 2010.

Appendix. System of Linear Equations Description and Solution Using Modified Harmonic Balance Method

The vectors $\{A\}$ and $\{B\}$ and the matrix $[\Delta]$ in the system of linear equations, described in Eq. (2.45), considering the shaft-disc system with rigid-short and flexible-long bearing supports, are given in details as follow. The obtained system of linear equations is repeated as:

$$[\Delta]\{A\} = \{B\}$$

where

$$\begin{aligned}
&\{A\}_{(4\times m\times(l+1))\times 1} = \left(\{A'\}_{1\times(4\times m\times(l+1))}[C]_{(4\times m\times(l+1))\times(4\times m\times(l+1))}\right)^T = \\
&\left(\left\{{}^{0}\mathrm{A}_1^1, {}^{0}\mathrm{A}_1^2, {}^{0}\mathrm{A}_1^3, {}^{0}\mathrm{A}_1^4, \ldots, {}^{s}\mathrm{A}_n^1, {}^{s}\mathrm{A}_n^2, {}^{s}\mathrm{A}_n^3, {}^{s}\mathrm{A}_n^4, \ldots, {}^{l}\mathrm{A}_m^1, {}^{l}\mathrm{A}_m^2, {}^{l}\mathrm{A}_m^3, {}^{l}\mathrm{A}_m^4\right\}[C]\right)^T \\
&[C] = \\
&diag\left[e^{i\Omega t}, e^{i\Omega t}, e^{i\Omega t}, e^{i\Omega t}, \ldots, e^{in\Omega t}, e^{in\Omega t}, e^{in\Omega t}, e^{in\Omega t}, \ldots, e^{im\Omega t}, e^{im\Omega t}, e^{im\Omega t}, e^{im\Omega t}\right]
\end{aligned} \tag{A.1}$$

The vector $\{A\}$ is considered as a multiplication of vector $\{A'\}$ and matrix $[C]$. The vector $\{A'\}$ represents the coefficients of proposed solution in modified harmonic method, Eq. (2.44), and matrix $[C]$ is a diagonal matrix with elements in exponential form $e^{in\Omega t}$. The parameter n $(n = 1, 2, \ldots, m)$ represents the order of the super-harmonic component. The elements of vector $\{A\}$ are considered as ${}^{s}A_n^j e^{in\Omega t}$, in which the superscripts s $(s = 0, 1, 2, \ldots, l)$ and j $(j = 1, 2, 3, 4)$ denote the number of the shaft segment and the jth root, α_{jn}, of the characteristic equation, Eq. (2.43), respectively. Considering that the unbalance mass is located on disc 1, shown in Figure 2.3, vector $\{B\}$ describes the external harmonic forces on shaft segments, is given by:

$$\{B\}_{(4\times m\times(l+1))\times 1} = \left\{0, 0, 0, 0, m_u r_u \Omega^2 e^{i\Omega t}, 0, \ldots, 0\right\}^T \tag{A.2}$$

Matrix $[\Delta]$ is the coefficient matrix, which the value of its elements depend on type of the bearing support, employed crack breathing function and location of the cracks and the disc on the shaft. For the cracked rotor disc-bearing system, as shown in Figure 2.3, with rigid-short bearing supports and considering the exponential form of the Mayes and Davis breathing function, the matrix $[\Delta]$ is expressed as:

$$[\Delta]_{(4\times m\times(l+1))\times(4\times m\times(l+1))} = \begin{bmatrix}
{}^{1}\Delta & {}^{0}_{s2}\Delta_0 & 0 & \cdots & & 0 \\
{}^{0}_{s1}\Delta_1 & {}^{2}\Delta & & & & \\
0 & & \ddots & {}^{0}_{sn}\Delta_0 & & \vdots \\
\vdots & & {}^{0}_{s(n-1)}\Delta_1 & {}^{n}\Delta & & 0 \\
 & & & & \ddots & {}^{0}_{sm}\Delta_0 \\
0 & & \cdots & 0 & {}^{0}_{s(m-1)}\Delta_1 & {}^{m}\Delta
\end{bmatrix} \tag{A.3}$$

where

$$\begin{gathered}
\left[{}^{0}_{sn}\Delta_{g}\right]_{((l+1)\times 4)\times((l+1)\times 4)} = \frac{-1}{2}\left[{}^{0}_{sn}\Delta^{0}_{g}\middle|{}^{0}_{sn}\Delta^{1}_{g}\middle|{}^{0}_{sn}\Delta^{2}_{g}\middle|{}^{0}_{sn}\Delta^{3}_{g}\middle|{}^{0}_{sn}\Delta^{4}_{g}\right], \\
\left[{}^{0}_{sn}\Delta^{1}_{g}\right] = \left[{}^{0}_{sn}\Delta^{2}_{g}\right] = \left[{}^{0}_{sn}\Delta^{4}_{g}\right] = [0]\,, g = 0, 1. \\
\left[{}^{0}_{sn}\Delta^{0}_{g}\right] = \left[\begin{array}{cccc}
\multicolumn{4}{c}{[0]_{3\times 4}} \\ \hline
{}_{g}\Delta^{c}_{11n1} & {}_{g}\Delta^{c}_{12n1} & {}_{g}\Delta^{c}_{13n1} & {}_{g}\Delta^{c}_{14n1} \\ \hline
\multicolumn{4}{c}{[0]_{12\times 4}}
\end{array}\right] \\
\left[{}^{0}_{sn}\Delta^{2}_{g}\right] = \left[\begin{array}{cccc}
\multicolumn{4}{c}{[0]_{11\times 4}} \\ \hline
{}_{g}\Delta^{c}_{31n2} & {}_{g}\Delta^{c}_{32n2} & {}_{g}\Delta^{c}_{33n2} & {}_{g}\Delta^{c}_{34n2} \\ \hline
\multicolumn{4}{c}{[0]_{4\times 4}}
\end{array}\right]
\end{gathered} \tag{A.4}$$

$$\left[{}^{n}\Delta\right]_{(4\times(l+1))\times(4\times(l+1))} = \left[{}^{n}\Delta_{0}\middle|{}^{n}\Delta_{1}\middle|{}^{n}\Delta_{2}\middle|{}^{n}\Delta_{3}\middle|{}^{n}\Delta_{4}\right]$$

$$\left[{}^{n}\Delta_{0}\right] = \left[\begin{array}{cccc}
1 & 1 & 1 & 1 \\
\Delta^{1}_{1n} & \Delta^{1}_{2n} & \Delta^{1}_{3n} & \Delta^{1}_{4n} \\
\Delta^{2}_{11n} & \Delta^{2}_{12n} & \Delta^{2}_{13n} & \Delta^{2}_{14n} \\
\Delta^{3}_{11n} + \Delta^{c}_{11n1} & \Delta^{3}_{12n} + \Delta^{c}_{12n1} & \Delta^{3}_{13n} + \Delta^{c}_{13n1} & \Delta^{3}_{14n} + \Delta^{c}_{14n1} \\
\Delta^{4}_{11n} & \Delta^{4}_{12n} & \Delta^{4}_{13n} & \Delta^{4}_{14n} \\
\Delta^{5}_{11n} & \Delta^{5}_{12n} & \Delta^{5}_{13n} & \Delta^{5}_{14n} \\ \hline
\multicolumn{4}{c}{[0]_{14\times 4}}
\end{array}\right]$$

$$\left[{}^{n}\Delta_{1}\right] = \left[\begin{array}{cccc}
0 & 0 & 0 & 0 \\
0 & 0 & 0 & 0 \\
-\Delta^{2}_{11n} & -\Delta^{2}_{12n} & -\Delta^{2}_{13n} & -\Delta^{2}_{14n} \\
-\Delta^{3}_{11n} & -\Delta^{3}_{12n} & -\Delta^{3}_{13n} & -\Delta^{3}_{14n} \\
-\Delta^{4}_{11n} & -\Delta^{4}_{12n} & -\Delta^{4}_{13n} & -\Delta^{4}_{14n} \\
-\Delta^{5}_{11n} & -\Delta^{5}_{12n} & -\Delta^{5}_{13n} & -\Delta^{5}_{14n} \\
\Delta^{2}_{21n} & \Delta^{2}_{22n} & \Delta^{2}_{23n} & \Delta^{2}_{24n} \\
\Delta^{3}_{21n} & \Delta^{3}_{22n} & \Delta^{3}_{23n} & \Delta^{3}_{24n} \\
\Delta^{4}_{21n} + \Delta^{d}_{21n} & \Delta^{4}_{22n} + \Delta^{d}_{22n} & \Delta^{4}_{23n} + \Delta^{d}_{23n} & \Delta^{4}_{24n} + \Delta^{d}_{24n} \\
\Delta^{5}_{21n} + \Delta^{i}_{21n} & \Delta^{5}_{22n} + \Delta^{i}_{22n} & \Delta^{5}_{23n} + \Delta^{i}_{23n} & \Delta^{5}_{24n} + \Delta^{i}_{24n} \\ \hline
\multicolumn{4}{c}{[0]_{10\times 4}}
\end{array}\right]$$

$$[{}^n\Delta_2] = \left[\begin{array}{cccc}
\multicolumn{4}{c}{[0]_{6\times 4}} \\
\hline
-\Delta^2_{11n} & -\Delta^2_{12n} & -\Delta^2_{13n} & -\Delta^2_{14n} \\
-\Delta^3_{11n} & -\Delta^3_{12n} & -\Delta^3_{13n} & -\Delta^3_{14n} \\
-\Delta^4_{11n} & -\Delta^4_{12n} & -\Delta^4_{13n} & -\Delta^4_{14n} \\
-\Delta^5_{11n} & -\Delta^5_{12n} & -\Delta^5_{13n} & -\Delta^5_{14n} \\
\Delta^2_{21n} & \Delta^2_{22n} & \Delta^2_{23n} & \Delta^2_{24n} \\
\Delta^3_{21n} & \Delta^3_{22n} & \Delta^3_{23n} & \Delta^3_{24n} \\
\Delta^4_{21n} + \Delta^d_{21n} & \Delta^4_{22n} + \Delta^d_{22n} & \Delta^4_{23n} + \Delta^d_{23n} & \Delta^4_{24n} + \Delta^d_{24n} \\
\Delta^5_{21n} + \Delta^i_{21n} & \Delta^5_{22n} + \Delta^i_{22n} & \Delta^5_{23n} + \Delta^i_{23n} & \Delta^5_{24n} + \Delta^i_{24n} \\
\hline
\multicolumn{4}{c}{[0]_{6\times 4}}
\end{array}\right]$$

$$[{}^n\Delta_3] = \left[\begin{array}{cccc}
\multicolumn{4}{c}{[0]_{10\times 4}} \\
\hline
-\Delta^2_{21n} & -\Delta^2_{22n} & -\Delta^2_{23n} & -\Delta^2_{24n} \\
-\Delta^3_{21n} & -\Delta^3_{22n} & -\Delta^3_{23n} & -\Delta^3_{24n} \\
-\Delta^4_{21n} & -\Delta^4_{22n} & -\Delta^4_{23n} & -\Delta^4_{24n} \\
-\Delta^5_{21n} & -\Delta^5_{22n} & -\Delta^5_{23n} & -\Delta^5_{24n} \\
\Delta^2_{31n} & \Delta^2_{32n} & \Delta^2_{33n} & \Delta^2_{34n} \\
\Delta^3_{31n} + \Delta^c_{31n2} & \Delta^3_{32n} + \Delta^c_{32n2} & \Delta^3_{33n} + \Delta^c_{33n2} & \Delta^3_{34n} + \Delta^c_{33n2} \\
\Delta^4_{31n} & \Delta^4_{32n} & \Delta^4_{33n} & \Delta^4_{34n} \\
\Delta^5_{31n} & \Delta^5_{32n} & \Delta^5_{33n} & \Delta^5_{34n} \\
\hline
\multicolumn{4}{c}{[0]_{2\times 4}}
\end{array}\right]$$

$$[{}^n\Delta_4] = \left[\begin{array}{cccc}
\multicolumn{4}{c}{[0]_{14\times 4}} \\
\hline
-\Delta^2_{31n} & -\Delta^2_{32n} & -\Delta^2_{33n} & -\Delta^2_{34n} \\
-\Delta^3_{31n} & -\Delta^3_{32n} & -\Delta^3_{33n} & -\Delta^3_{34n} \\
-\Delta^4_{31n} & -\Delta^4_{32n} & -\Delta^4_{33n} & -\Delta^4_{34n} \\
-\Delta^5_{31n} & -\Delta^5_{32n} & -\Delta^5_{33n} & -\Delta^4_{34n} \\
\Delta^2_{41n} & \Delta^2_{42n} & \Delta^2_{43n} & \Delta^2_{44n} \\
\Delta^6_{41n} & \Delta^6_{42n} & \Delta^6_{43n} & \Delta^6_{44n}
\end{array}\right]$$

$$
\begin{aligned}
\Delta^1_{jn} &= EI\lambda^2_{jn} \\
\Delta^2_{sjn} &= e^{L_s\lambda_{jn}} \\
\Delta^3_{sjn} &= \lambda_{jn}\Delta^2_{sjn} \\
\Delta^4_{sjn} &= \Delta^2_{sjn}\left(EI\lambda^3_{jn} + \left(n^2 - 2n\right)\rho A r_0^2\omega^2\lambda_{jn}\right) \\
\Delta^5_{sjn} &= \Delta^1_{jn}\Delta^2_{sjn} \\
\Delta^6_{sjn} &= \lambda^2_{jn}\Delta^2_{sjn} \\
\Delta^d_{sjn} &= m_d n^2\omega^2\Delta^2_{sjn} \\
\Delta^i_{sjn} &= \Delta^3_{sjn}\left(I_p n\omega^2 - I_t n^2\omega^2\right) \\
{}_g\Delta^c_{sjnr} &= \frac{1}{2}\left(\beta_r - i\gamma_r\right)\Delta^5_{sjn}e^{i(-1)^g\Phi_r} + \frac{1}{2}\left(\epsilon_r - i\delta_r\right) conj\left(\Delta^5_{sjn}e^{i(-1)^g\Phi_r}\right), r = 1, 2.
\end{aligned}
$$

where r denotes the number of the crack. The matrices $[{}^0_{sn}\Delta_g]$ and $[{}^n\Delta]$ in Eq. (2.45) have been determined considering that the cracks and the discs' locations are arranged as shown in Figure 2.3, ($L_0 \leqslant L_1 \leqslant L_2 \leqslant L_3 \leqslant L_4$). These matrices have to be updated for other arrangements of the cracks and disc on the shaft. For flexible-long bearing supports, in Eq. (2.45) the matrices $[{}^n\Delta_1]$ and $[{}^n\Delta_5]$ are modified as:

$$
[{}^n\Delta_0] = \left[\begin{array}{cccc}
\Delta^7_{1n} & \Delta^7_{2n} & \Delta^7_{3n} & \Delta^7_{4n} \\
\Delta^1_{1n}/\alpha_{1n} & \Delta^1_{2n}/\alpha_{2n} & \Delta^1_{3n}/\alpha_{3n} & \Delta^1_{4n}/\alpha_{4n} \\
\Delta^2_{01n} & \Delta^2_{02n} & \Delta^2_{023n} & \Delta^2_{04n} \\
\Delta^3_{01n} & \Delta^3_{02n} & \Delta^3_{03n} & \Delta^3_{04n} \\
\Delta^4_{01n} + \Delta^d_{01n} & \Delta^4_{02n} + \Delta^d_{02n} & \Delta^4_{03n} + \Delta^d_{03n} & \Delta^4_{04n} + \Delta^d_{04n} \\
\Delta^5_{01n} + \Delta^i_{01n} & \Delta^5_{02n} + \Delta^i_{02n} & \Delta^5_{03n} + \Delta^i_{03n} & \Delta^5_{04n} + \Delta^i_{04n} \\
\hline
\multicolumn{4}{c}{[0]_{14\times 4}}
\end{array}\right]
$$

$$
[{}^n\Delta_4] = \left[\begin{array}{cccc}
\multicolumn{4}{c}{[0]_{14\times 4}} \\
\hline
-\Delta^2_{21n} & -\Delta^2_{22n} & -\Delta^2_{23n} & -\Delta^2_{24n} \\
-\Delta^3_{21n} & -\Delta^3_{22n} & -\Delta^3_{23n} & -\Delta^3_{24n} \\
-\Delta^4_{21n} & -\Delta^4_{22n} & -\Delta^4_{23n} & -\Delta^4_{24n} \\
-\Delta^5_{21n} & -\Delta^5_{22n} & -\Delta^5_{23n} & -\Delta^4_{24n} \\
\Delta^8_{31n} & \Delta^8_{32n} & \Delta^8_{33n} & \Delta^8_{34n} \\
\Delta^3_{31n} & \Delta^3_{32n} & \Delta^3_{33n} & \Delta^3_{34n}
\end{array}\right]
$$

$$
\begin{aligned}
\Delta^7_{jn} &= -EI\alpha^3_{jn} + \rho A r_0^2\omega^2\alpha_{jn}\left(2n - n^2\right) - \left(S_1 + iS_4\right) - \left(S_2 + iS_3\right) \\
\Delta^8_{sjn} &= \Delta^2_{sjn}\left(-EI\alpha^3_{jn} + \rho A r_0^2\omega^2\alpha_{jn}\left(2n - n^2\right) - \left(S_1 + iS_4\right)\right) - conj\left(\Delta^2_{sjn}\right)\left(S_2 + iS_3\right)
\end{aligned}
\tag{A.5}
$$

Modeling the breathing cracks using the alternate breathing function described in Eq. (2.18), the matrix $[\Delta]$ is updated as:

$$[\Delta]_{(4\times m\times(l+1))\times(4\times m\times(l+1))} =$$

$$\begin{bmatrix}
{}^{1}\Delta & \left(\frac{10}{9}\right){}^{0}_{s2}\Delta_{0} & 0 & \left(\frac{e^{-i\pi}}{9}\right){}^{0}_{s4}\Delta_{0} & 0 & \cdots & & 0 \\
\left(\frac{10}{9}\right){}^{0}_{s1}\Delta_{1} & {}^{2}\Delta & \left(\frac{10}{9}\right){}^{0}_{s3}\Delta_{0} & 0 & \ddots & & & \\
0 & \left(\frac{10}{9}\right){}^{0}_{s2}\Delta_{1} & {}^{3}\Delta & \left(\frac{10}{9}\right){}^{0}_{s4}\Delta_{0} & \ddots & & & \vdots \\
\left(\frac{e^{i\pi}}{9}\right){}^{0}_{s1}\Delta_{1} & 0 & \left(\frac{10}{9}\right){}^{0}_{s3}\Delta_{1} & {}^{4}\Delta & \ddots & \left(\frac{e^{-i\pi}}{9}\right){}^{0}_{sn}\Delta_{0} & & \\
0 & \ddots & \ddots & \ddots & \ddots & 0 & & \\
 & & & & & \left(\frac{10}{9}\right){}^{0}_{sn}\Delta_{0} & & \\
\vdots & & \left(\frac{e^{i\pi}}{9}\right){}^{0}_{s(n-3)}\Delta_{1} & 0 & \left(\frac{10}{9}\right){}^{0}_{s(n-1)}\Delta_{1} & {}^{n}\Delta & \ddots & \\
 & & \ddots & & & & & 0 \\
 & & & & \ddots & \ddots & \ddots & \left(\frac{10}{9}\right){}^{0}_{sm}\Delta_{0} \\
0 & & & \cdots & & 0 & \left(\frac{10}{9}\right){}^{0}_{s(m-1)}\Delta_{1} & {}^{m}\Delta
\end{bmatrix} \qquad \text{(A.6)}$$